THE UNIVERSITY OF HULL

Observing the Effect of Galaxy Environment on the Evolution of Active Galactic Nuclei in the Era of Multiplexed Wide-Field Fibre-Optic Spectroscopy

being a Thesis submitted for the Degree of Doctor of Philosophy

in the University of Hull

by

Yjan Arthur Gordon, B.Sc. (Hons.) Physical Science (Open)

February 2018

"Long is the way and hard, that out of Hull leads up to the light"

– John Milton, *Paradise Lost (1667, adapted 2018)*

Acknowledgements

I take this opportunity to thank the many people whose support has made my time as a graduate student easier than it might otherwise have been. First and foremost, I thank my supervisors Kevin Pimbblet and Matt Owers. Their longstanding and constructive feedback has undoubtedly improved me as a researcher and subsequently the quality of this work. Moreover, I would like to thank Kevin for hiring me to undertake this project, I am forever grateful for the opportunities that have been opened up to me.

I was fortunate enough at the start of my PhD to share an office with three students, Jacob Crossett, Amelia Fraser-McKelvie, and Dane 'Gerzone' Kleiner, visiting from Monash University. These three provided not only academic support to a fledgling postgraduate student, but entertainment and friendship stretching well beyond their visit to Hull. Thanks here especially goes to Amelia for completely owning the role of academic big sister, providing sound advice on both scientific matters and career opportunities over the last three years.

Additionally several of my colleagues, both at Hull and afar, have my thanks for their support and insights at various points throughout my PhD. On this note, I'd particularly like to thank Brad Gibson for his steadfast backing and encouragement since his arrival at Hull. Further thanks go to Elke Roediger, Gareth Few, Siri Chongchitnan, Scott Croom, Andrew Hopkins, Sugata Kaviraj, and Sheona Urquhart.

I'd like also to record my gratitude to the many friends, office-mates, and colleagues who've made the last three years conducting this work easier and more enjoyable. Whilst there are too many of you to name you all, special mentions go to Connor, Lawrence, Matt, Nick, Chris, James, Marco, Walter, Jonny and Zoë. Notably, I thank Dr Simon Prentice of Liverpool John Moores University for our many discussions, often related to our transition from our undergraduate studies at the Open University to postgraduate research in astrophysics.

Lastly, but by no means least, I thank my mother for her unwavering support in every task I undertake, and continuing to believe in me even, and especially, when I no longer do.

Declaration of Originality

This thesis is submitted in partial fulfilment of the degree of Doctor of Philosophy from the University of Hull. I declare that the work undertaken in this thesis is original and my own and was carried out under the supervision of Dr Kevin Pimbblet and Dr Matt Owers. Where work, results, or ideas have been taken from other sources, those sources are explicitly referenced.

A substantial amount of the work here has been used for peer-reviewed journal articles either led by, or co-authored by myself. The nature of modern astronomy is such that a number of co-authors is commonplace on research publications, and indeed is necessitated by the large number of observations and data reduction required. Nonetheless, the work that has been published from this thesis was the principle responsibility of myself in terms of driving the science case, analysis, and writing up. The observations used were conducted by others as part of large scale surveys, and the data products from these observations are explicitly referenced.

Chapter 2 has been published as Gordon et al. (2017) MNRAS 465, 2671, Chapter 3 has been published as Gordon et al. (2018) MNRAS 475, 4223, while Chapter 4 presents work that is the basis for a paper I am leading that is in preparation. The analysis of the completeness at small angular scales of the SDSS and GAMA spectroscopic samples in Chapter 5 was performed as part of my contribution for the journal article "*The Taipan Galaxy Survey: Scientific Goals and Observing Strategy*" (da Cunha et al., 2017 PASA 34, e047) on which I am a co-author. The details of the contributions of myself and my co-authors to those works are described in the prologues of the relevant Chapters.

Candidates signature:

Date:

Abstract

In this thesis, we use the environment of active galactic nuclei (AGN) to test AGN unification. Furthermore, we analyse how interaction between the environment and host galaxy can influence AGN evolution. This is done for a range of galaxy densities, from the field to the cores of galaxy clusters.

We utilise the high spectroscopic completeness of the Galaxy And Mass Assembly survey (GAMA) to perform a comparative analysis of the pair-wise environments of broad- and narrow-line AGN. Our observations show no difference in the frequency of broad- and narrow line AGN in all but the tightest galaxy pairs. Furthermore, our observations show no difference in the colour or star-forming properties of the neighbouring galaxies of AGN, contrary to previous works. These observations are consistent with AGN unification and indicate that close galaxy interactions may increase nuclear obscuration.

Optically selected AGN preferentially inhabit infall regions of massive clusters, and are rarely found in the cluster core. Using the depth and completeness of GAMA, we optically select 451 AGN from 695 groups in the halo mass range $11.5 \lesssim \log_{10}(M_{200}/\mathrm{M}_{\odot}) \lesssim 14.5$ at $z < 0.15$. At $\log_{10}(M_{200}/\mathrm{M}_{\odot}) > 13.5$ our results are similar to previous works on clusters with a deficit of AGN observed in the group core at 3.6σ confidence. At lower halo masses no preferred location for AGN is seen.

Weakly accreting radio AGN are found in dense galactic environments, and minor-mergers have been invoked as a plausible mechanism to 'drip-feed' these low-excitation radio galaxies (LERGs). We use deep optical imaging from the Dark Energy Camera Legacy Survey (DECaLS) to search for low-surface brightness tidal remnants in a sample of 189 LERGs. We observe such tidal features in $27^{+3.5}_{-3.0}$ per cent of LERGs compared to $31.5^{+2.5}_{-2.3}$ per cent of a control sample. Our results are thus inconsistent with the hypothesis that minor-mergers play a significant role in LERG fuelling.

Contents

List of Figures

List of Tables

1. Introduction

"To see the world in a grain of sand, and to see infinity in a wild flower, hold infinity in the palm of your hands, and eternity in an hour"

– William Blake, *Auguries of Innocence (1863)*

1.1 The Great Debate and the Emergence of Extragalactic Astronomy

Although observers have been aware of the existence of the celestial objects we now refer to as galaxies throughout the telescopic era (e.g. Messier, 1781; Herschel, 1802), it is only in the last century that we have begun to understand the physical nature of these phenomena. Originally thought to reside within the Milky Way, evidence began to mount in the early 1900s that some nebulae were, perhaps, 'island universes' like our own Milky Way in nature but residing beyond its confines (Kant, 1755; Curtis, 1917). This formed the basis of the so-called 'great debate' in astronomy during the first few decades of twentieth century.

In the early twentieth century it was believed that the Milky way had a diameter of $< 30\,000$ light years (Shapley & Curtis, 1921). In combination with the apparent observations of van Maanen (1916), this was argued by Harlow Shapley to suggest that if spiral nebulae were extragalactic in nature, then their rotational speed must be greater than the speed of light (Shapley & Curtis, 1921). Furthermore, the brightness of some novae observed in spiral nebulae implied absolute magnitudes not seen in other stars in the sky (Shapley, 1919). On the basis of such physical difficulties, accepting a Universe that extended beyond the confines of the Milky Way seemed illogical.

Counter to this position, Heber Curtis argued that the frequency of novae was higher in spiral nebulae than in the rest of the Milk-Way (Curtis, 1917). This could be explained by the spiral nebulae being extremely distant such that the rate of novae per volume of space was roughly consistent with the Milky Way (Curtis, 1920). Moreover, the absolute magnitudes of

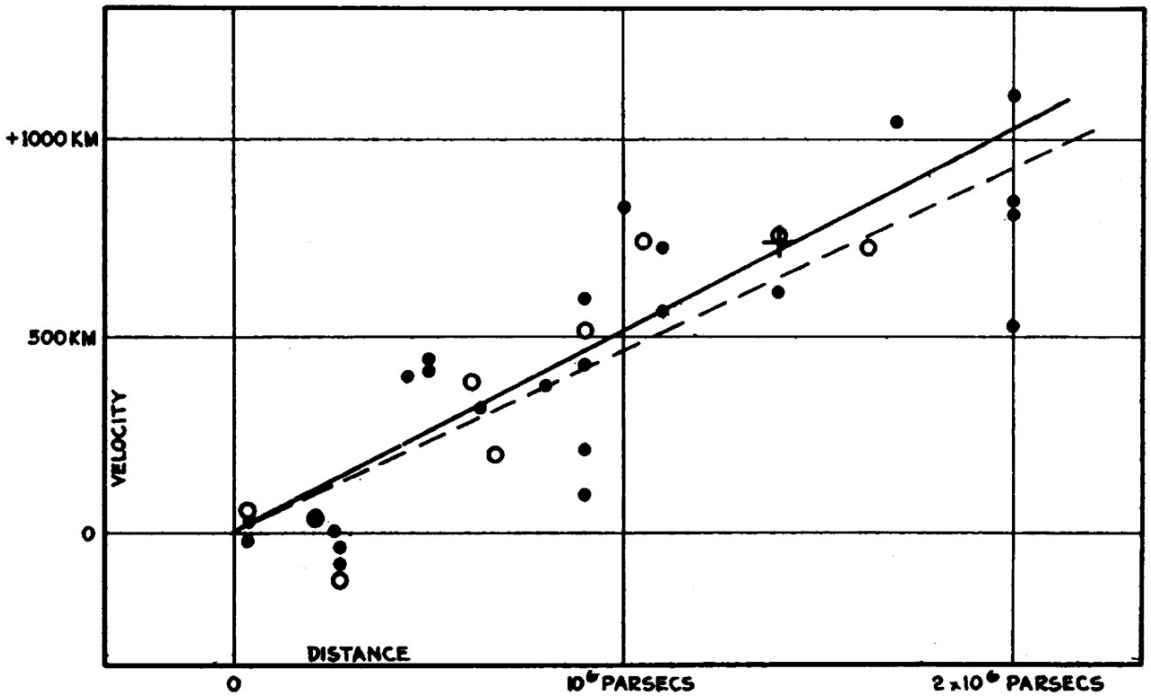

Figure 1.1: The observations of Hubble (1929) showing the increase in galaxy recessional velocity with distance.

novae in spiral nebulae were, for the most part, consistent with novae within the Milky Way should they reside at extragalactic distances (Shapley & Curtis, 1921).

Studying the light curves of Cepheid variable stars in the Andromeda nebula, Hubble (1927a) showed that 'spiral nebulae' were located at exceedingly large distances relative to objects within the Milky Way. This proved to be a death knell for arguments of Shapley, showing that the observations of van Maanen (1916) could not be correct.

Building on this model of the Universe where many different galaxies existed, another observation in the early 20th century was that the light from these extragalactic sources was stretched relative to nearby objects (Slipher, 1915). This redshifting of the light, an optical doppler effect, allowed the velocities of these galaxies to be calculated relative to the observer. Hubble (1929), again using Cepheid variables as a standard candle, showed a positive relationship between galaxy distance and recessional velocity (see Figure 1.1). This was the first observational confirmation of the expanding Universe theory (Lemaître, 1927, 1931), and consequently early extragalactic astronomy shed light not only on the nature of galaxies, but on the fundamental physics of the Universe as a whole.

In the modern era we have a model of the Universe based in no small part on the

observations and work conducted nearly a century previously. This introductory chapter has aimed to give the reader a broad background of our current understanding of galaxy evolution as a whole. Various observational properties of galaxies, and their significance, are discussed, beginning with the more obvious, e.g., shape and colour, before moving on to more subtle properties that can be observed such as how rapidly a galaxy is forming stars. More specifically, the active galactic nucleus (AGN) phenomenon and the large scale surveys used in modern extragalactic astronomy are described in order to prepare the reader for the rest of this thesis. This work aims to directly address how the galactic environment, on both large and small scales, affects the evolution of AGN, and to what extent can we answer this with the current range of wide-field multi-object spectroscopic galaxy surveys?

1.2 Observable Properties of Galaxies

1.2.1 Morphology

It became clear early in the era of extragalactic astronomy that not all galaxies were the same, with stark observational differences at the most conspicuous level. In particular, observations showed that galaxies did not all share the same morphology (Hubble, 1926). Noticing that the spiral population could be bisected into those with and without central bars, and that both the eccentricity of ellipticals and the tightness of spiral arms varied between galaxies, Hubble (1926) classified galaxies based on these morphological features. It is worth noting that it is often thought that Hubble intended for this classification scheme to demonstrate an evolutionary path for galaxies (e.g., Coles & Lucchin, 2002; Carroll & Ostlie, 2006; Baldry, 2008), perhaps as a result of the common name of 'the Hubble sequence' by which it is referred. However, he was explicit in his statement that *"the entire classification is purely empirical without prejudice to theories of evolution"* (Hubble, 1927b).

The Hubble sequence splits galaxies broadly into those with 'spiral', 'elliptical', and 'lenticular'. The so-called 'tuning fork' shape of the Hubble sequence is achieved by splitting the spiral, or late-type, population into the barred and unbarred populations, as shown in Figure 1.2. These are ordered according to the tightness of the spiral structure, thus forming the two tines of the fork. The handle of the fork, joined to the the tines by the lenticular

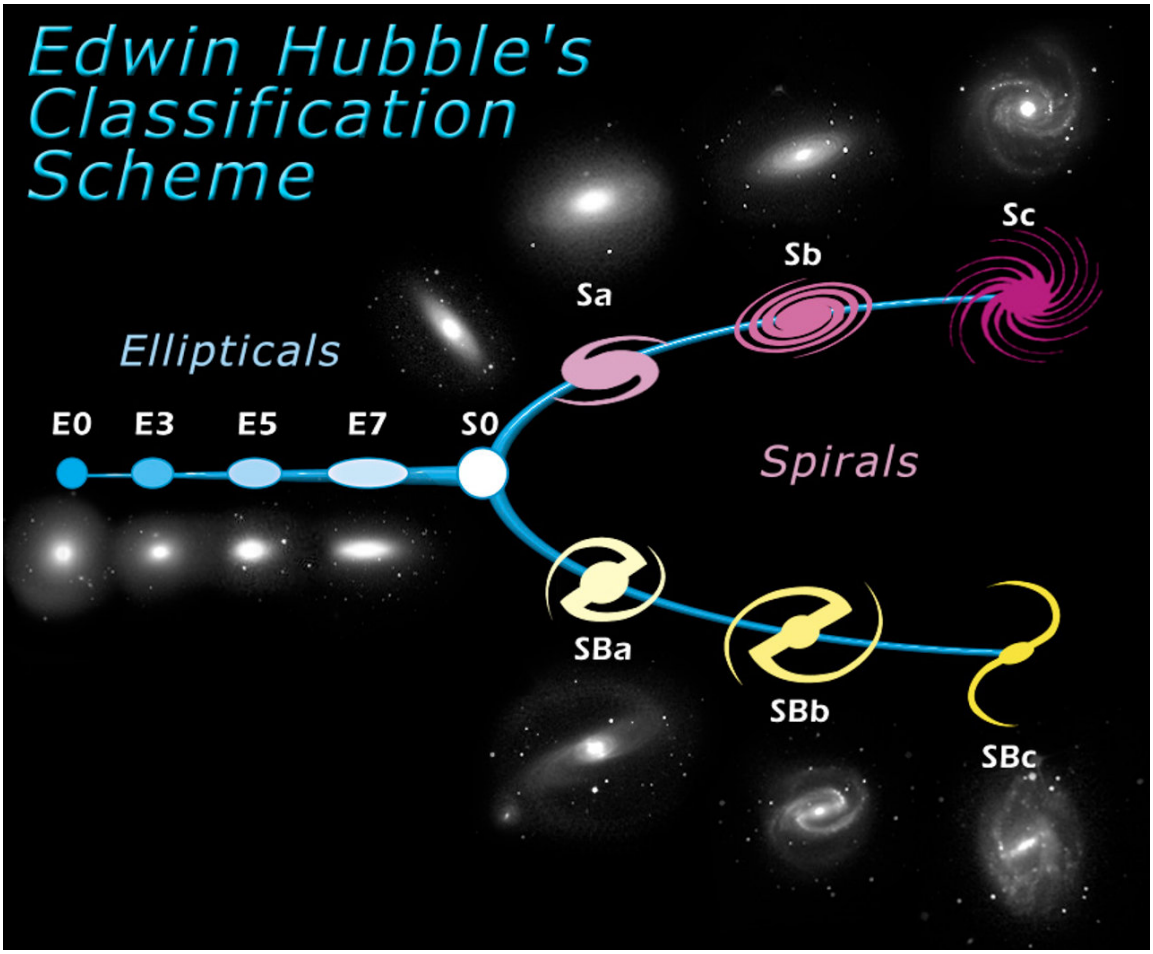

Figure 1.2: The Hubble sequence or 'tuning fork' of galaxy classification by morphology. The left hand side shows early type or elliptical galaxies making up the handle of the tuning fork. The two tines of the fork are the barred and unbarred spirals with spiral tightness decreasing with distance from the handle of the fork (image credit: NASA, obtained from http://www.spacetelescope.org).

population, is formed by ordering the elliptical population by eccentricity, i.e., from spherical to highly elliptical.

1.2.2 Luminosity and mass

The brightness of a galaxy is dependent on both the distance the light has had to travel by the inverse square law, and the intrinsic brightness, or luminosity, of the galaxy. The luminosity can be considered to be the sum of the luminosities of the individual luminous objects (e.g. the stellar population) that make up a galaxy. Given that the luminosity of a star is related to its mass by the mass-luminosity relation (Eddington, 1924), then the luminosity of a galaxy is

related to the total mass of all the stars within that galaxy. That is to say if a galaxy contains more stars it will have a higher stellar mass and thus higher integrated luminosity. Thus if one assumes a stellar population for a galaxy, and then estimates a mass to light ratio, then the stellar mass, M_*, of that galaxy may be calculated.

Beyond just being used to estimate the mass of individual galaxies, the galaxy luminosity function can be used to learn about the galaxy population as a whole. Schechter (1976) parameterised such a luminosity function to be of the form

$$n(L)\,\mathrm{d}L = \phi^* \frac{L}{L^*}^{\alpha} \mathrm{e}^{-L/L^*}\,\mathrm{d}L, \tag{1.1}$$

where ϕ^* is a normalisation constant, L^* is a characteristic luminosity, and α is a free parameter. The observations of Loveday et al. (2015) define $\phi^* = 10^{-2.12\pm0.07}\,h^3\,\mathrm{Mpc}^{-3}$, and $\alpha = -1.23 \pm 0.01$.

The shape of the luminosity function, and therefore the stellar mass function, is, however, inconsistent with the halo mass function (Moster et al., 2010; Mutch et al., 2013), as shown in Figure 1.3. As the halo mass function is dominated by non-baryonic dark matter, this indicates that the efficiency of star-formation is not constant at all halo masses. That is to say, that the difference in stellar and halo mass functions is evidence that something inhibiting stellar mass growth at either end of the luminosity function. At the low mass end of the luminosity function, this is attributed to stellar feedback (e.g., Scannapieco et al., 2008; Krause et al., 2014). This is a process where supernovae shocks and winds from massive stars act to heat and expel gas from the galaxy, thus removing the fuel required for star-formation to occur. At the other end of the scale, feedback from AGN (e.g., Croton et al., 2006; Newton & Kay, 2013), may either heat the surrounding gas (quasar mode feedback) or remove it from the galaxy by mechanical mechanisms such as winds or radio jets (radio mode feedback).

1.2.3 Colour

Other than the morphology and luminosity of a galaxy, its next most obvious property is its colour. Given that, when observing a galaxy, the majority of the optical luminosity is the integrated output of the individual stellar luminosities of that galaxy, then a galaxy's colour tells us about its stellar population. By using photometric filters to quantify the

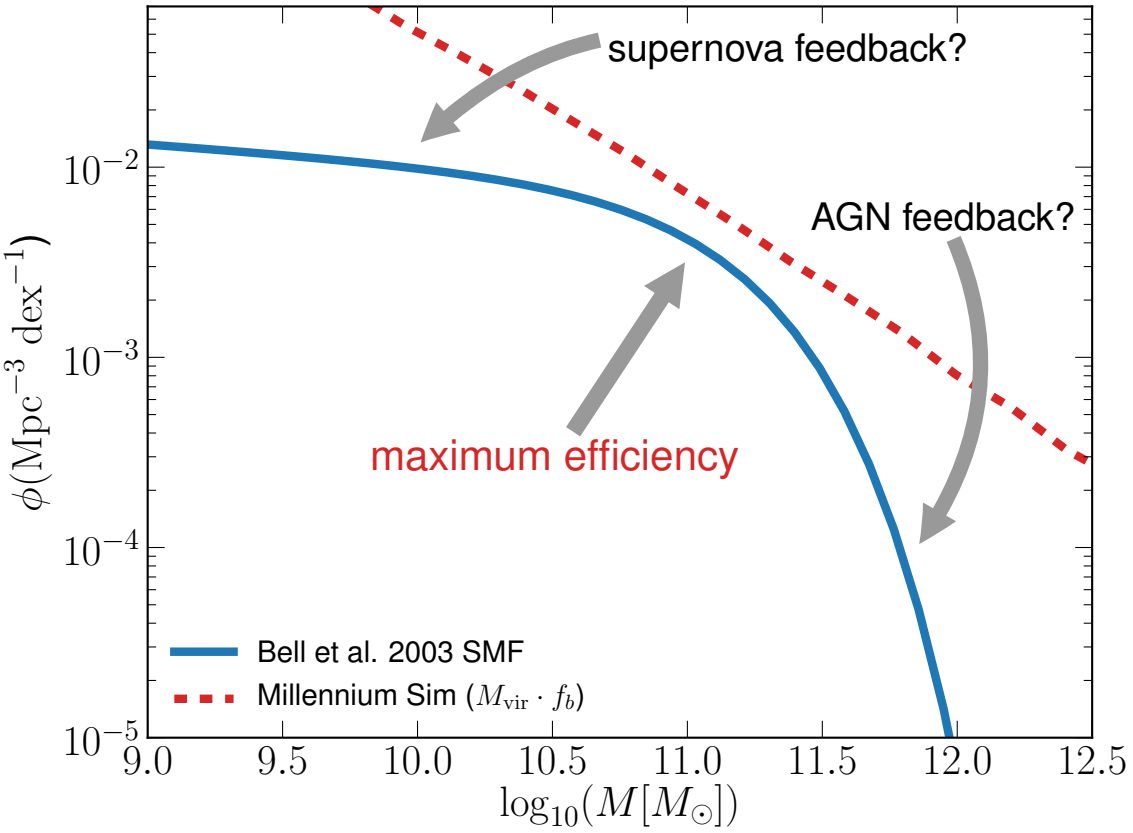

Figure 1.3: A comparison of the stellar mass function based on the observations of Bell et al. (2003, blue curve) to the dark matter halo mass function from the Millennium Simulation (red dashed line, Springel et al., 2005). The different shapes of the functions demonstrated that the efficiency of stellar mass growth is inhibited at both the low and high ends of the stellar mass function, with supernovae and AGN feedback respectively invoked as the causal mechanisms. Originally Fig. 2 in Mutch et al. (2013).

colour, and comparing to the absolute magnitude, and thus by proxy the stellar mass, the galaxy population naturally splits in to two groups. Figure 1.4 shows the 'red-sequence' and 'blue-cloud' populations on such a colour-mass diagram.

As a basic example of why galaxy colour is an important parameter, one can consider what stellar information can be gained from stellar colour. Luminous blue stars, i.e. spectral type O, B, and A on the Hertzsprung-Russell (HR, Russell, 1914) diagram, are massive and relatively short lived. Thus if the colour of a galaxy is relatively blue, one can infer that the galaxy experienced a period of star-formation in its recent past. On the other hand, should a galaxy be red then it may be the case that the stellar population is dominated by red stars with longer life-cycles. In this case the dearth of luminous blue stars suggests a long time (> 1 Gyr, e.g. Ferreras & Silk, 2000; Yi et al., 2005; Crossett et al., 2017) has passed since that galaxy was actively forming stars.

It should be noted that caution must taken when using photometry to infer the make-up of galactic stellar populations in this way. Interstellar dust preferentially absorbs and scatters blue light over red. This relative extinction of blue light can cause a galaxy to appear redder than it should based entirely on on it's stellar constituents (Mathis, 1990).

1.2.4 Redshift

Atomic transitions occur at precise energies, and hence wavelengths, and contribute to the shape of spectra through absorption and emission of photons (see Figure 1.5). Knowing the rest-frame, or laboratory, wavelength of such spectroscopic features allows for the accurate measurement of the redshift of a galaxy. From Hubble's law the redshift of a galaxy is related to its distance from the observer by,

$$d \approx \frac{cz}{H_0}, \tag{1.2}$$

where $H_0 \approx 70\,\mathrm{km\,s^{-1}\,Mpc^{-1}}$ is the Hubble constant. Thus, obtaining spectra for galaxies provides a reliable estimate of their distance from Earth, particularly when the galaxy is so distant as to make using other distance measures (e.g. Cepheid variables or stars at the tip of the red giant branch) impractical.

This of course assumes that the redshift is attributable entirely to the Hubble flow. In reality,

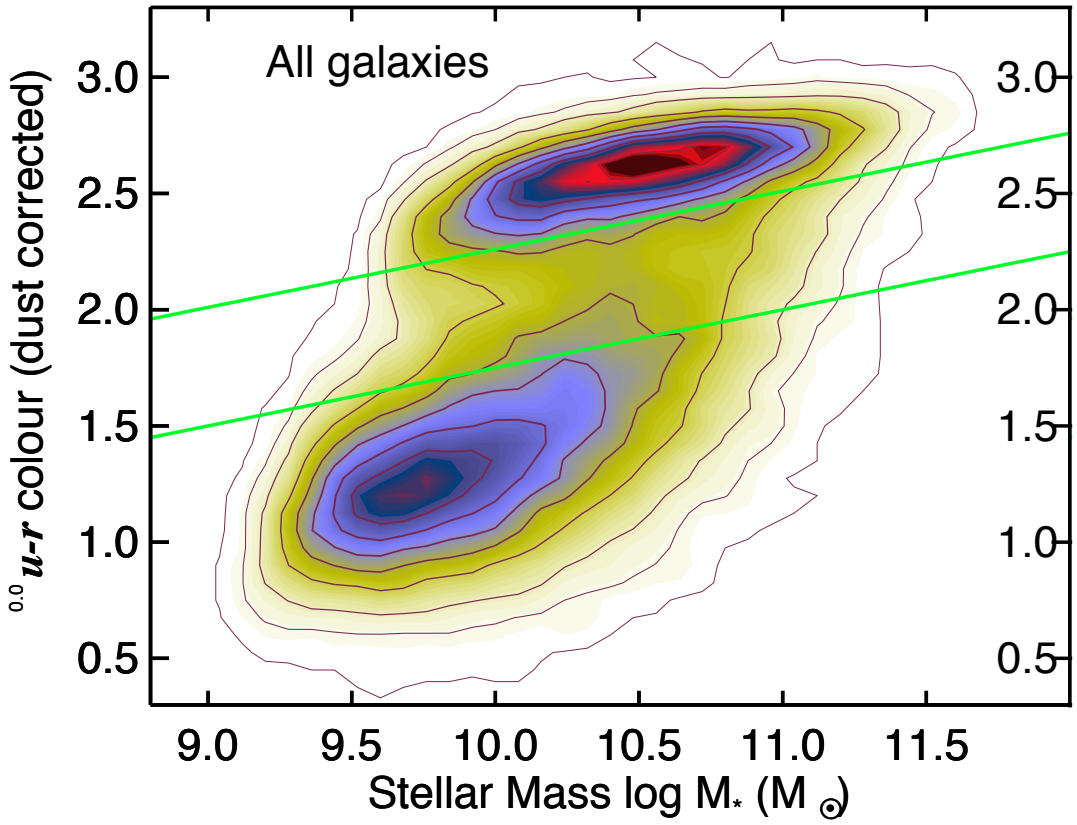

Figure 1.4: Colour-mass diagram for galaxies observed by the Sloan Digital Sky Survey. The x-axis shows the absolute galaxy stellar mass, and the y-axis shows the rest-frame corrected $u - r$ colour of the galaxy. The top peak (higher $u - r$) shows the galaxy 'red sequence', and the lower, broader, peak shows the 'blue cloud' population. The green lines mark a transition region between the blue cloud and red sequence known as the green valley. Image credit: Schawinski et al. (2014).

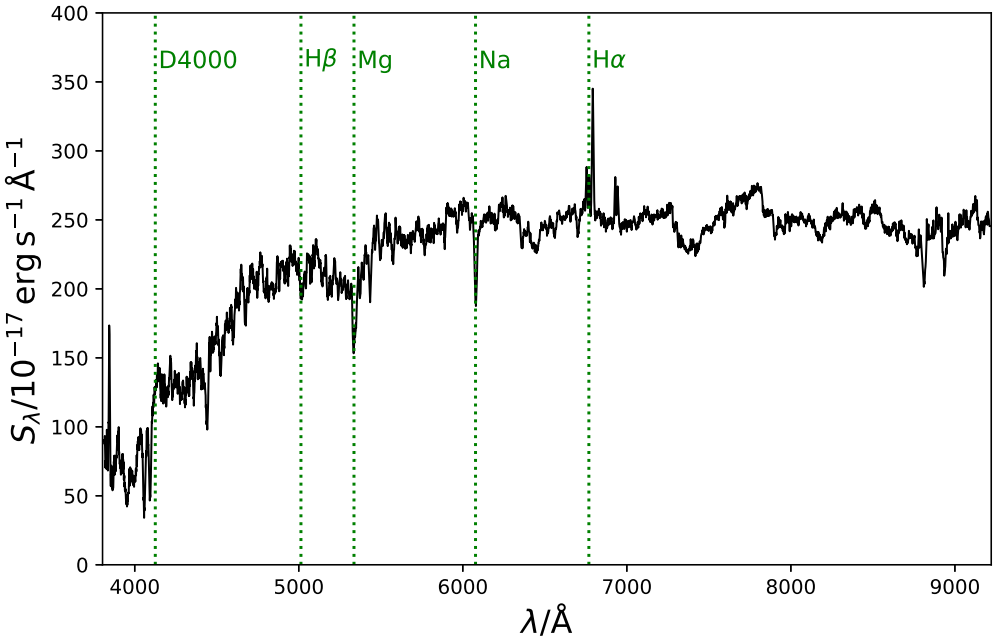

Figure 1.5: An example spectrum of an early-type galaxy obtained by the Sloan Digital Sky Survey (SDSS, York et al., 2000). Example features marked on the spectrum are, in increasing wavelength order, the 4 000 Å break, the Hβ ($\lambda_{\rm em}$ = 4861 Å), Mg triplet ($\lambda_{\rm em}$ = 5174.5 Å), Na doublet ($\lambda_{\rm em}$ = 5893 Å), and Hα ($\lambda_{\rm em}$ = 6563 Å) absorption lines. This particular galaxy, SDSS J111310.40+274905.6, has a redshift of z = 0.0313.

the recessional velocity is the sum of both the contribution from the Hubble flow, i.e., the cosmological redshift, and the peculiar velocity introduced by local gravitational sources, e.g., a nearby galaxy or galaxy cluster, acting on the motion of the galaxy in space. Furthermore, Hubble's law in this form is only valid in recent cosmological history. As redshift increases, and hence the age of the Universe decreases, the expansion rate of the Universe changes and thus the Hubble 'constant' is not constant (Hogg, 1999). This discrepancy approaches ~ 5 per cent by $z = 0.2$ (see Figure 1.6).

1.2.5 Star-formation rate

Using spectroscopic observations can provide more information than simply a distance measurement to a galaxy. Whilst galaxy colour can indicate the age of its stellar population, using the atomic transition lines visible in spectra more reliable determinations of the stellar population age can be quantified, and indeed the rate at which star formation is occurring within the galaxy, can be ascertained. In particular, emission lines such as [O II] $\lambda\lambda 3727, 3729$ and Hα are used to calculate this due to their association with a young stellar population (e.g., Kennicutt, 1992; Aragón-Salamanca et al., 2003; Wijesinghe et al., 2011; Gunawardhana et al., 2013). For example, Kennicutt et al. (1994); Kennicutt (1998); Madau et al. (1998) show that, for a Salpeter (1955) initial mass function, the star-formation rate, Ψ, may be calculated by

$$\frac{\Psi}{\mathrm{M}_\odot\,\mathrm{yr}^{-1}} = \frac{8 \times 10^{-42}}{\mathrm{erg\,s}^{-1}\,\mathrm{M}_\odot\,\mathrm{yr}^{-1}} L_{\mathrm{H}\alpha}. \tag{1.3}$$

Beyond optical spectroscopy, photometry from ultraviolet, infra-red, and radio bands may also be used to determine a galaxy's star-formation rate (e.g., Yun et al., 2001; Calzetti, 2007; Shabala et al., 2012; Cluver et al., 2014).

Star-formation within galaxies doesn't just build stellar mass, it is also responsible for the unexpected shape of the low-mass end of the galaxy luminosity function (Figure 1.3). A young stellar population in combination with supernovae will heat and shock the interstellar medium. In combination with the relatively shallow gravitational potential of low mass galaxies, this can allow gas to escape from the galaxy, forming an outflow (Samui, 2014; Hayward & Hopkins, 2017). This mechanism reduces the amount of cold gas available, and thus regulates stellar mass building in low-mass galaxies. These outflows can be observed

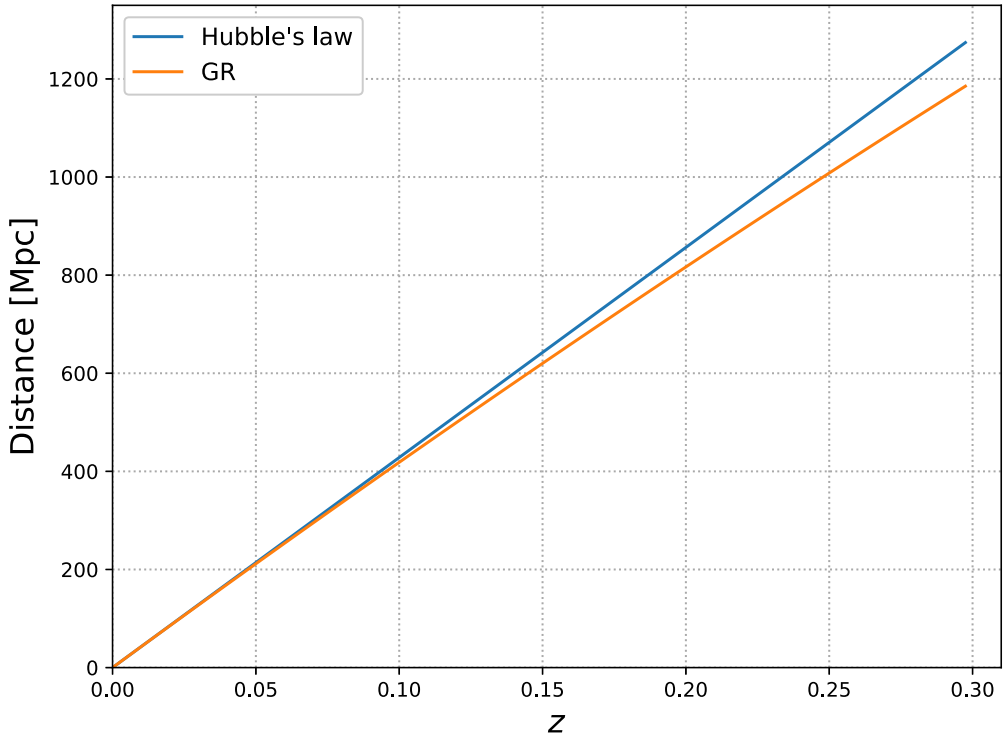

Figure 1.6: The deviation of comoving distance from Hubble's law with redshift. The blue line shows the comoving distance as a function of redshift using Hubble's law (eq 1.2). The orange line shows the general relativistic comoving distance as a function of redshift for a flat ΛCDM Universe. This accounts for the change in scale factor of the Universe with time, calculated by $D_{\text{comoving}} = \frac{c}{H_0}\int_0^z \frac{dz'}{E(z')}$, where $E(z) = \sqrt{\Omega_M(1+z^3)+\Omega_\Lambda}$ is a parameter accounting for the scale factor as a function of the mass and dark energy parameters of the assumed cosmological model (Hogg, 1999). For both calculations $H_0 = 70\,\text{km s}^{-1}$ Mpc is used. For the general relativistic calculation, the condition $\Omega_M = 0.3$, $\Omega_\Lambda = 0.7$ is assumed. At low redshift the differences are negligible and thus Hubble's law is a fair approximation. As redshift increases however, so does the discrepancy between the the two models.

Figure 1.7: The starburst galaxy M82 as imaged by the Hubble Space Telescope Advanced Camera for Surveys' Wide Field Channel. Note the outflow of matter from the central region of the galaxy. Image credit: NASA/ESA, J. Gallagher (University of Wisconsin), M. Mountain (STScI), and P. Puxley (National Science Foundation), obtained from http://hubblesite.org/image/1876/news_release/2006-14.

in the local Universe, with M82 being the achetypal example (See figure 1.7, Walter et al., 2002).

1.2.6 Transient events

A final broad class of observations that are relevant to extragalactic astronomy, is that of transient events. Whilst galaxies are clearly dynamic structures that evolve over time, that timescale is of the order $\sim 10^{6-9}$ yr, far beyond the lifetime of civilisations let alone individual observers. Transient events are observations that show rapid variability. AGN for instance can show variability on the order of a few hours to days (Lee et al., 2002), possibly due to magnetic flares in the accretion disk (Kawaguchi et al., 2000; Goosmann et al., 2006). Given

the finite speed of light, this in itself is evidence that a compact region is responsible for the observation. Taking the example of variability of the order 1 day, indicates that the AGN occupies a region with radius 1 light-day, or $\sim$ 170 AU, comparable to the size of the solar system[1].

More prominent examples of transient events however are supernovae. These stellar explosions, at luminosities $M_g < -20$ mag (De Cia et al., 2017), are of comparable brightness to galaxies. Moreover as point sources, supernovae are more readily detectable, magnitude for magnitude, than galaxies where the light is spread over a measurable area of the sky. That is to say, that when a supernova occurs in a galaxy, it is often prominent enough to be observed. Other extragalactic transient observables include gamma-ray bursts and gravitational waves (e.g., Klebesadel et al., 1973; Abbott et al., 2016).

The observation of type 1a supernovae, are of particular importance as they can provide a distance measure that is independent of redshift. In the instance of type 1a supernovae where the progenitor is a white dwarf that has exceeded the Chandrasekhar mass of $\sim 1.4\,M_\odot$ (Stoner, 1930; Chandrasekhar, 1931) due to the accretion of matter from an orbiting companion, the luminosity of the resultant supernova will be proportional to the square of the Chandrasekhar mass, and thus this mechanism provides a standard candle. It was through the observations of type 1a supernovae that it was discovered that the expansion of the Universe was accelerating (Schmidt et al., 1998; Perlmutter et al., 1999). The nature of the driver of this acceleration in the expansion of the Universe, known as dark energy, remains one of the key open questions in physics today.

1.3 Environment as a Driver of Galaxy Evolution

The Universe is far from a homogenous distribution of galaxies, and indeed observations show a distinct 'web' of matter in the Universe (see Figure 1.8). This cosmic web collects galaxies into clusters, regions of high galaxy density, at the nodes of the web (Bond et al., 1996). Between the clusters, filaments containing galaxies and galaxy groups span the cosmic voids

[1]As a point of interest, at the time of writing the Voyager 1 space probe was > 140 AU from the Sun, not dissimilar from the estimates of the size of AGN based on their variability. Voyager 1 distance taken from https://voyager.jpl.nasa.gov/mission/status/ on the 11th of February 2018.

(Kleiner et al., 2017). Despite their name, the voids do still contain galaxies, it is just that the number density of galaxies here is exceptionally low (Pan et al., 2012; Fraser-McKelvie et al., 2016).

Different galactic environments provide different mechanisms acting upon a galaxy throughout its evolution. Dressler (1980) showed that the morphology of a galaxy was dependent upon the galaxy density of the environment (see Figure 1.9). In dense environments, such as the cores of clusters, galaxies are more likely to be early type, whereas in less dense environments late type galaxies are more common. Furthermore, galaxies in denser environments tend to have older stellar populations than those in less dense environments (Thomas et al., 2005).

In the virialised cores of galaxy clusters, the temperature of the intra-cluster medium can reach temperatures of the order of megaKelvin (Fabian, 1994). At such temperatures the kinetic energy of the medium makes it unlikely that accretion on to the gravitational potential well provided by a galaxy will occur (Davies et al., 2017). Additionally, the halo of gas clouds and satellite remnants that normally surround a massive galaxy can be lost, which further prevents refuelling of the galaxy with cold gas. This process, known as 'strangulation', results in an effective cessation of star-formation once the galaxy has used up gas reserves, and an ageing stellar population ensues (Larson et al., 1980; Masters et al., 2010). The process of strangulation can be compounded by ram-pressure stripping (RPS, Gunn & Gott, 1972; Roediger, 2009). The stripping of the gas from a galaxy on its infall in to a cluster means that the gas supply of a galaxy is already depleted by the time it reaches an environment where strangulation becomes a dominant mechanism.

Outside the virialised core of clusters, the galaxy population is a mixture of infalling and backsplash galaxies (Gill et al., 2005; Pimbblet, 2011). In this region, the galaxy density is such that low-speed galaxy-galaxy interactions are prevalent. Both harassment and mergers can influence the gas distribution within a galaxy, and hence the star-formation and nuclear activity within that galaxy (Sanders et al., 1988; Barnes & Hernquist, 1991, 1996; Mihos & Hernquist, 1996; Moore et al., 1996, 1998). Additionally, RPS can act to change the morphology of galaxies as it naturally acts to thicken the stellar-disk component of spiral

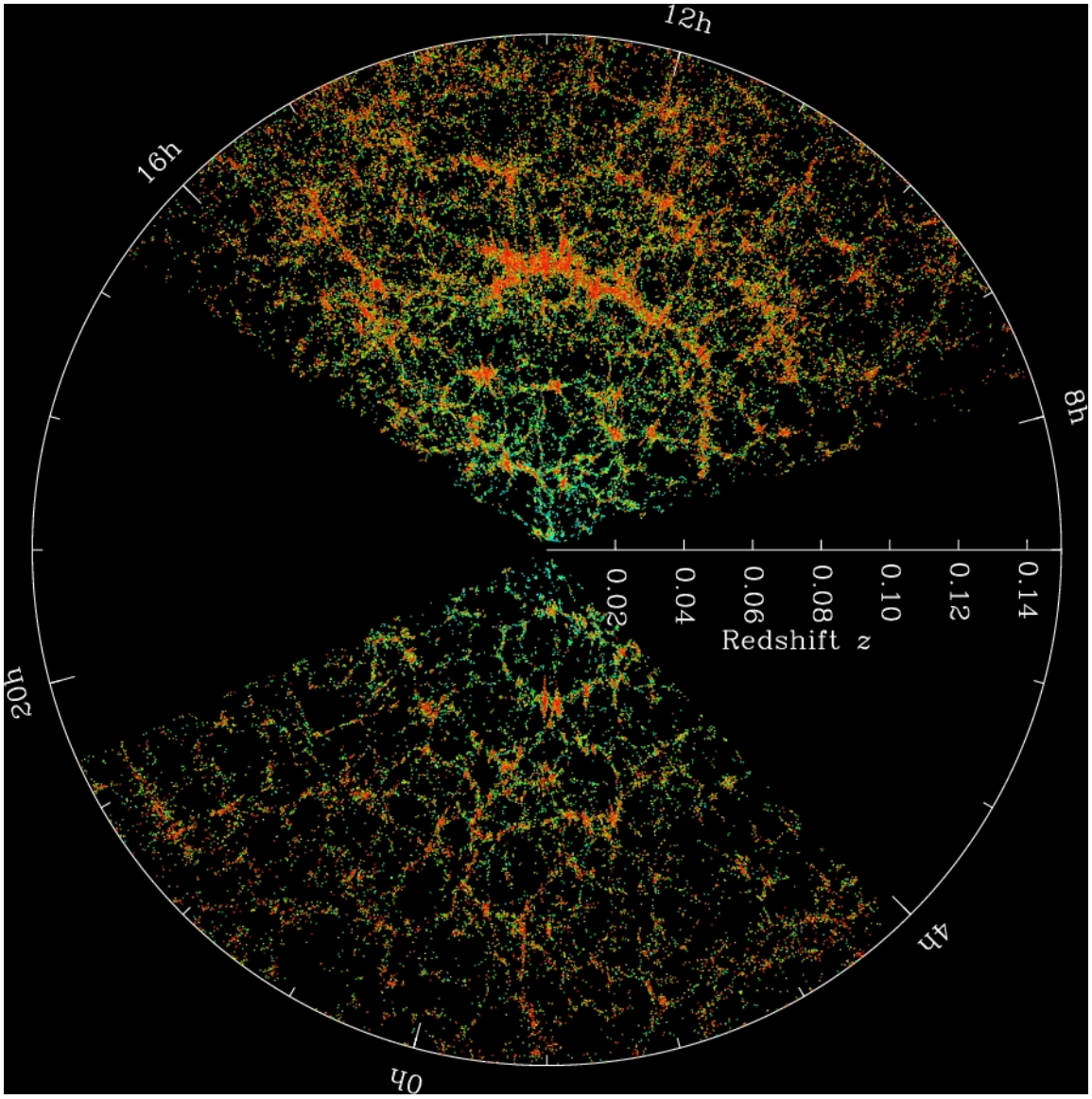

Figure 1.8: The large-scale structure of the Universe as observed by SDSS. Each dot represents a galaxy or collection of galaxies, with galaxy number density increasing from green to red. The collection of galaxies into clusters at the nodes of a web of filaments is readily apparent. Image credit: SDSS, obtained from http://www.sdss.org/science/.

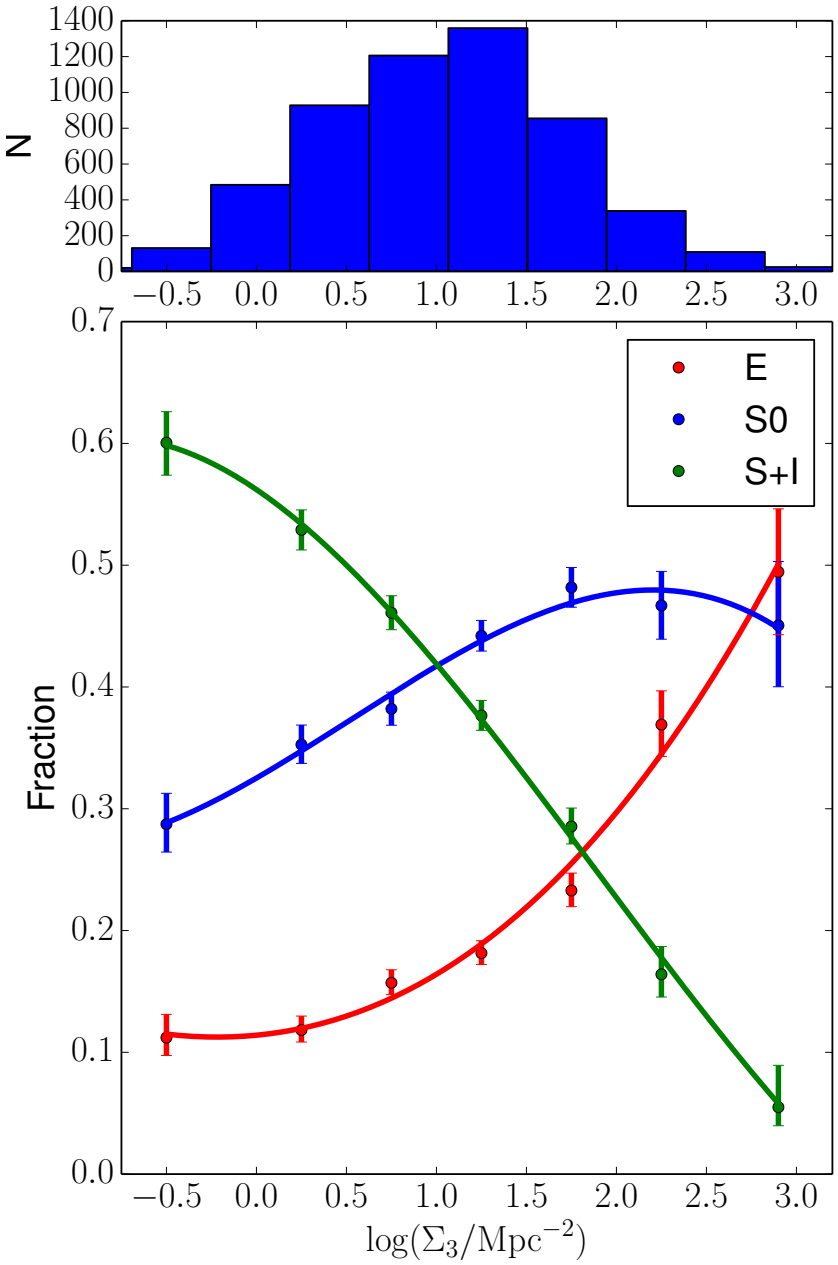

Figure 1.9: The morphology-density relationship as presented in Houghton (2015), an update to the work of Dressler (1980). The fraction of each morphology type elliptical (E, red), lenticular/S0 (S0, blue), and spiral and irregular (S+I, green) is shown per density bin. Density here is calculated as Σ_3, the projected denisty to the third nearest neighbour. The total number of galaxies at each density is shown in the histogram above the main plot. Originally Fig. 3 in Houghton (2015).

galaxies (Quilis, 2000). Furthermore, the stripping of gas can lead to turbulent gas tails trailing behind a galaxy. As the galaxy falls to the cluster centre, where the ram-pressures are most extreme, star-formation can occur in the turbulent gas tails. The result is a phenomenon known as 'Jellyfish galaxies', a name based on their similar appearance to the marine life-form with the same name (Roediger, 2009; Owers et al., 2012; Ebeling et al., 2014).

Galaxy groups are the low mass analogues of galaxy clusters. This group environment has been shown to both trigger star formation through the number of galaxy interactions (particularly in compact groups Hickson, 1997; Scudder et al., 2012a), as well as quench this process through RPS and tidal interactions (Crossett et al., 2017). Galaxy pairs provide a laboratory to test the effect of interactions on galaxies that will merge in the near future or are already in the process of merging, within a range of large scale environments (e.g., cluster, group, field, Ellison et al., 2008, 2010; Robotham et al., 2011). Galaxies in pairs have been shown to have enhancements in star-formation (Ellison et al., 2008; Scudder et al., 2012b), and are more likely to exhibit morphological disturbances (Ellison et al., 2010; Robotham et al., 2014). Furthermore, and of particular relevance to this thesis, the fraction of galaxies hosting an AGN has been shown to be enhanced by a factor of 2.5 in galaxy pairs with separations lower than 40 kpc relative to galaxies without a nearby neighbour (Ellison et al., 2011).

1.4 Active Galactic Nuclei

The first observations of AGN were made as far back as the first decade of the twentieth century, when Fath (1909a) observed strong emission lines in the 'spiral nebula' NGC1068. At the time the nature of spiral nebulae was unknown, and these observations, along with absorption lines in other spiral nebulae, were interpreted as being the result of a star cluster obscured by the gas of these nebulae (Fath, 1909b). It wasn't until the mid twentieth century however that it became apparent that a distinct type of phenomenon was being observed. Seyfert (1943) observed that spiral galaxies with apparently stellar cores, i.e., those with bright nuclei, exhibited strong ionisation lines in their spectra. Woltjer (1959) noted that the excitation in these Seyfert galaxies may be the result of the high density nature of the nucleus, postulating that the majority of galaxies may have such high-mass nuclei but that

galaxies with ionised nuclei may have more massive cores. The discovery of quasi-stellar radio sources (quasars, also referred to as quasi-stellar objects, QSOs, Matthews & Sandage, 1963) and their high redshifts (Greenstein & Matthews, 1963; Schmidt, 1963) added to the evidence that a 'different type' of galaxy existed.

We now know that Seyfert galaxies and quasars belong to the class of objects collectively called active galactic nuclei or AGN. At the core of every massive galaxy resides a super-massive black hole (SMBH), and an AGN refers to, specifically, the nucleus of a galaxy where we can observe the effects of the SMBH actively accreting matter (Salpeter, 1964; Zel'dovich, 1964). As matter is accreted onto the SMBH dynamic friction acts on the accretion flow to heat the infalling matter. This accretion flow and the black hole itself are collectively referred to as the central engine of the AGN. If the accretion rate, $\dot{M}$, is efficient enough, that is $\gtrsim 0.01\dot{M}_{\rm Edd}$, then an optically thick accretion disk forms. The Eddington accretion rate, $\dot{M}_{\rm Edd}$, given by

$$\dot{M}_{\rm Edd} = \frac{L_{\rm Edd} R}{GM}, \tag{1.4}$$

where $L_{\rm Edd} = 1.26 \times 10^{38} (M/{\rm M}_\odot)\,{\rm erg\,s^{-1}}$, is the accretion rate required to produce the Eddington luminosity. In such an accretion mode, a hot corona can form above the accretion disk leading to inverse Compton up-scattering of photons to X-ray energies (Urry & Padovani, 1995). The result is a non-thermal continuum associated with efficiently accreting black holes, that can dominate the spectral energy distribution of a galaxy hosting a powerful AGN at shorter wavelengths. Furthermore, the high-energy photons associated with with radiatively efficient AGN (both thermally produced UV and non-thermally produced X-ray) act to ionise the surrounding intragalactic medium, producing the emission lines associated with AGN. These high energy photons produced by the AGN contribute to the shape of the spectral energy distribution of the host galaxy, producing a feature known as the 'big blue bump' (Wilkes, 2004), shown in Figure 1.10.

Although as a distinct phenomenon AGN were originally discovered by radio astronomy (they were observed in the optical prior to this but their true nature was unknown, Matthews & Sandage, 1963), the effects of an AGN on their host galaxy make them observable across the electromagnetic spectrum (Mickaelian & Sanders, 2014). However, not all AGN are ob-

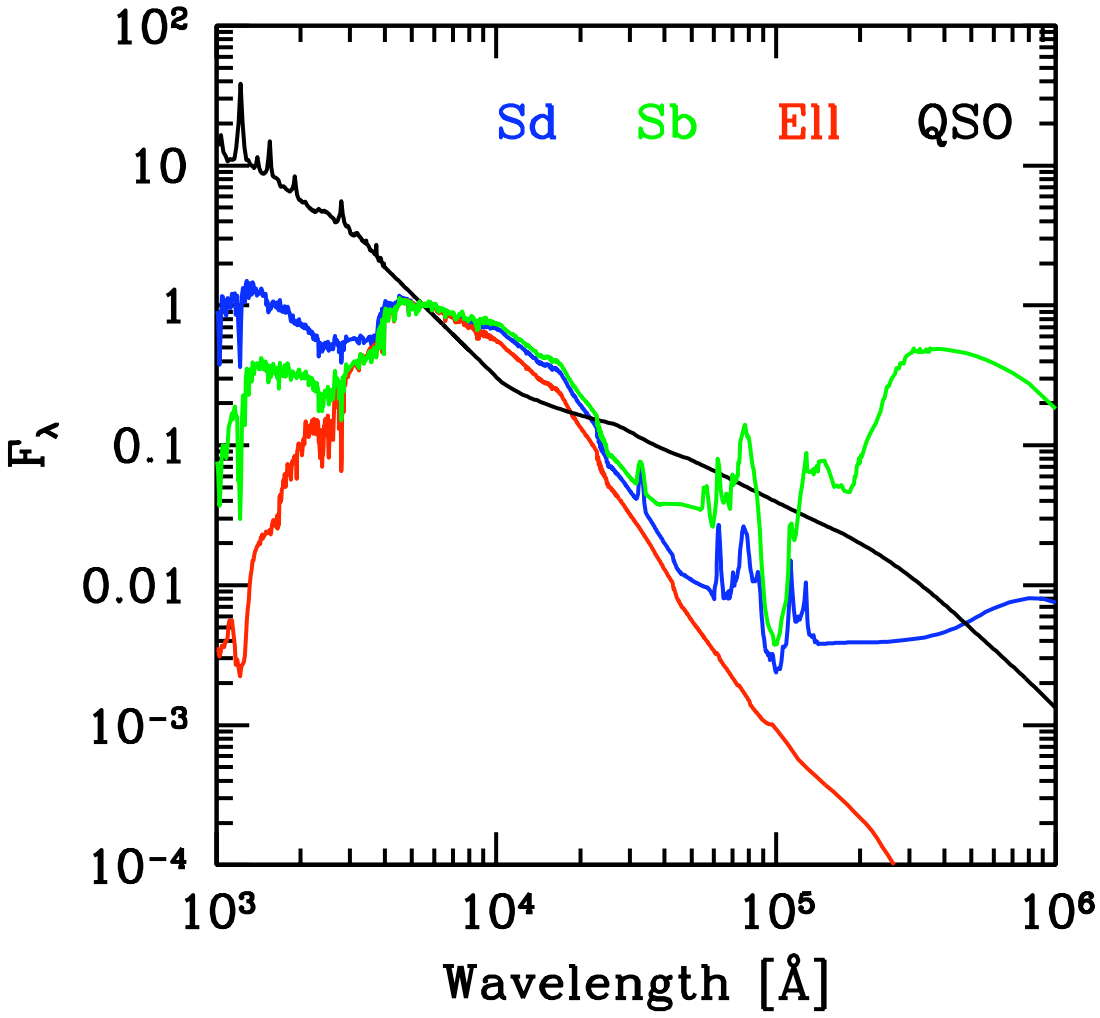

Figure 1.10: Template spectral energy distributions from the ultraviolet, 10^3 Å, to the far infrared, 10^6 Å, of spiral galaxies (Sd, Sb), an elliptical galaxy (Ell), and a quasar (QSO). The quasar, an AGN, has an entirely different shaped spectrum to the other types of galaxies, with substantially more flux in the ultraviolet, the AGN 'big blue bump' feature. This is the result of high-energy photons produced by the AGN's accretion disk. Image credit, Fig. 8 of Walcher et al. (2011).

servable in every band of the electromagnetic spectrum (Urry & Padovani, 1995). Therefore multi-wavelength observations can provide clues to the physics occurring in different AGN, and allow the population of AGN to be split in to different types of AGN. Given the observational history of AGN, and the sometimes fundamental differences in the physics that result in these observations, AGN are often split into those with radio emission, and those without (Wilson & Colbert, 1995).

1.4.1 Radio-loud AGN

The term radio-loud AGN (RLAGN) applies to galaxies where the radio emission is attributed to an AGN. In an AGN, the source of this radio emission is synchrotron emission from relativistic jets that are produced by the central engine of the AGN. Whilst the mechanism producing this jet is debated (e.g., Sauty et al., 2002; Beall, 2015), one of the favoured models is that of Blandford & Znajek (1977). In this model, strong magnetic fields within the accretion flow, coupled with the gravitational field of the rotating black hole, result in a 'force-free' zone in the central engine in which pair production occurs. These particles are then 'launched' along the magnetic poles of the system at relativistic speeds, thus creating the AGN jets. The interaction of these jets with the interstellar medium gives rise to the synchrotron emission and resultant radio luminosity of RLAGN. It is important to note that Bremsstrahlung from H II regions and supernovae shocks will also produce radio emission. Therefore, care must be taken to confirm that the radio emission is due to nuclear activity in order to classify a galaxy as hosting a RLAGN.

Accounting for ~ 10 per cent of the AGN population (Kellermann et al., 1989), RLAGN themselves can be further sub-classified. When the morphology of RLAGN is considered, Fanaroff & Riley (1974) noted that the radio luminosity of the source was correlated with where the strongest radio emission, known as the hot spot, was produced within the jet. By classifying as Fanaroff-Riley type 1 (FR I) jets with the hot spot near the galactic nucleus, and Fanaroff-Riley type 2 (FR II) jets where the hot spot was closer to the leading edge of the jet than the nucleus, Fanaroff & Riley (1974) showed that FR Is and FR IIs where relatively cleanly separated at radio luminosities of $L_{178\,\mathrm{MHz}} \sim 10^{25}\,\mathrm{W\,Hz^{-1}\,sr^{-1}}$. Examples of both FR I and FR II radio morphologies are shown in Figure 1.11.

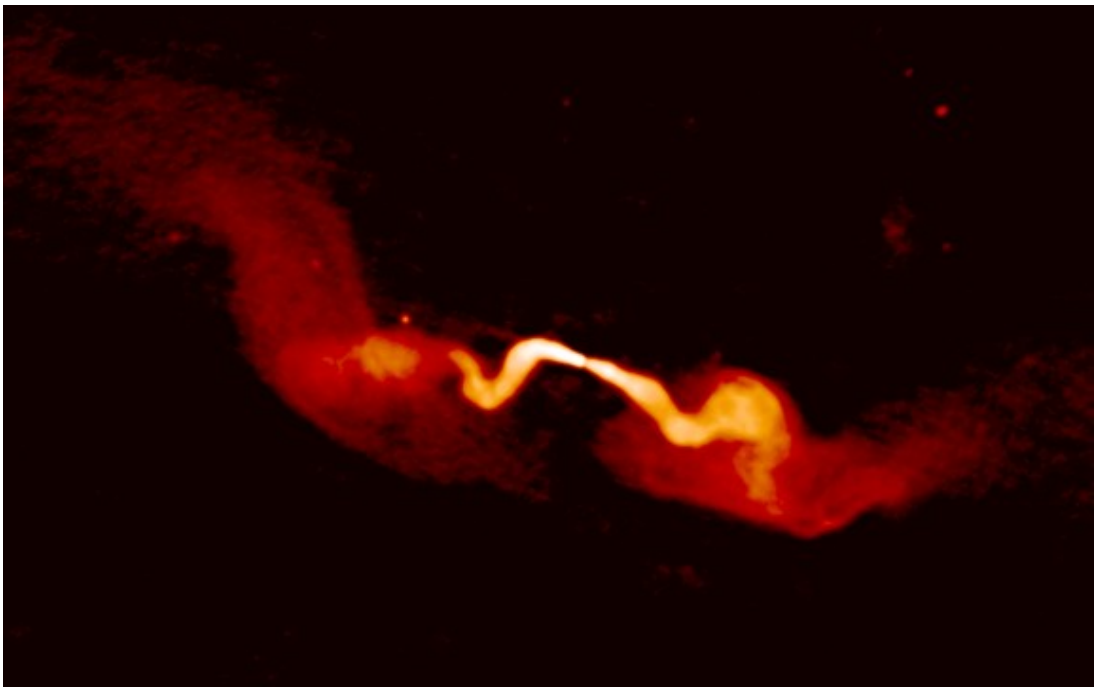

(a) FR I

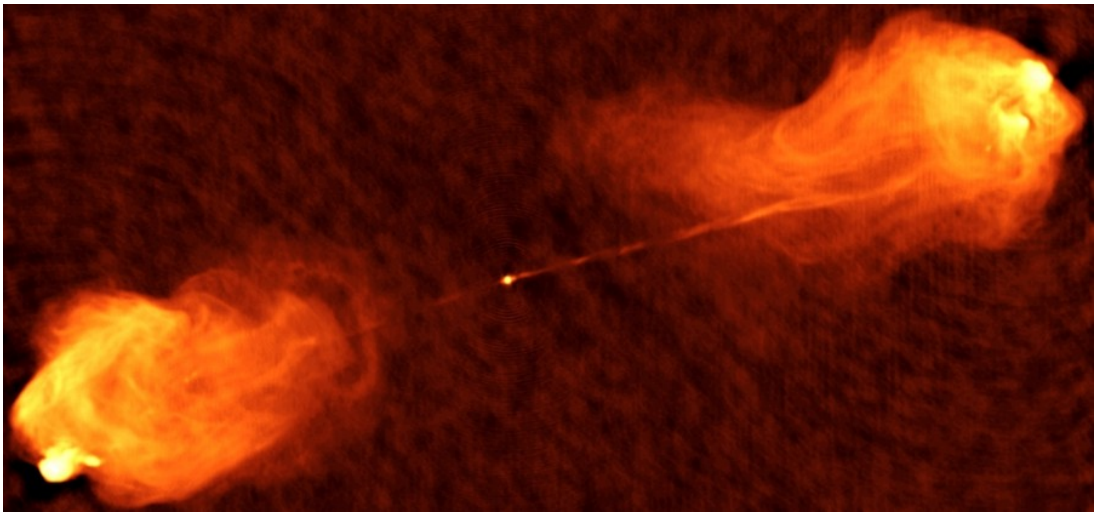

(b) FR II

Figure 1.11: Example radio morphologies obtained by the Very Large Array. Panel (a) shows the radio galaxy 3C 31 at 5 GHz, a typical FR I radio galaxy. Note that the brightest regions of the radio emission are nearer the nucleus than the leading edge of the jets/plumes. Panel (b) shows 3C 405, more often known as Cygnus A, at 1.4 GHz. In this image it is readily apparent that the brightest regions of radio emission are on the leading edge of the jets, in the radio lobes. This is typical of FR II morphology. Image credit: National Radio Astronomy Observatory/Associated Universities Incorporated, obtained from http://images.nrao.edu/AGN/Radio_Galaxies.

The relationship between radio morphology and power in RLAGN is evidence of a dichotomy in the RLAGN population (Fanaroff & Riley, 1974; Owen & Ledlow, 1994; Gopal-Krishna & Wiita, 2001). Optical spectroscopy of RLAGN adds to this with two distinct populations observed, those with, and those without the strong ionisation lines seen in optically selected AGN (e.g., Hine & Longair, 1979; Hardcastle et al., 2007; Best & Heckman, 2012). Those RLAGN exhibiting strong ionisation lines, known as high-excitation radio galaxies (HERGs) are often associated with the highest radio powers and, hence, FR II radio morphology. Low-exciation radio galaxies (LERGs) on the other hand are associated with lower radio powers and, often, FR I radio morphology.

The different spectral properties in the two RLAGN populations indicates the physical mechanism at the root of the dichotomy. As the ionisation in AGN is the result of an efficient accretion process, a lack of ionisation is suggestive of an inefficient accretion mode, i.e., $\dot{M} \ll 0.01\dot{M}_{\rm Edd}$ (Maraschi et al., 2012). The nature of the mechanisms that fuel such 'drip-feeding' of LERGs remains an open question (Hardcastle et al., 2007; Best & Heckman, 2012; Ellison et al., 2015), and is the basis of Chapter 4 of this thesis.

1.4.2 Radio-quiet AGN

Radio-quiet AGN are active galaxies that either have very low radio-luminosity, or are detected without the need for a radio observation. Examples of possible detection methods of radio quiet AGN include:

- direct observation of the high-energy photons (X-ray/UV) from the the central engine (Ward et al., 1980; Atlee & Mathur, 2009),
- Doppler broadening of Balmer emission due to high velocity gas in the vicinity of the black hole (Seyfert, 1943; Khachakian & Weedman, 1971),
- strong emission lines as the result of the ionisation of gas by the high energy photons produced by the central engine(Urry & Padovani, 1995),
- thermal emission from dust and gas heated by the AGN (infrared, de Grijp et al., 1985, 1987; Xu et al., 2015).

Unlike, RLAGN, AGN selected in bands other than the radio rely upon mechanisms that are indicative of an efficiently accreting nucleus. That is to say, whist HERGs may be the radio-loud analogues of radio-quiet AGN, LERGs need not be.

Optical spectroscopy has shown that the radio-quiet population of AGN can be sub classified into two distinct types, those with and those without broad Balmer emission lines (see Figures 1.12 and 2.3). This is also true of HERG population of RLAGN where emission lines can still be observed. Originally this observation was noted in the Seyfert galaxies, and broad- and narrow-line Seyferts were referred to as Seyfert 1s and Seyfert 2s (abbreviated to Sy1/2) respectively (Khachakian & Weedman, 1971). Since Seyfert galaxies are now known to be the same type of phenomenon as other AGN, this terminology has been expanded. A type 1 AGN is any AGN that exhibits broad (FWHM $\gtrsim 1000\,\mathrm{km\,s^{-1}}$ Osterbrock, 1981) Balmer emission, and a type 2 AGN is one shows only narrow emission lines.

1.4.3 AGN unification

Optical unification

In the early 1980s, the emergence of spectropolarimetric observations of galaxies led to the discovery of 'hidden' broad Balmer emission lines in type 2 AGN (Miller & Antonucci, 1983; McLean et al., 1983; Antonucci & Miller, 1985). Based on the thermal re-emission of light observed in the infrared in Seyfert galaxies, this polarisation of the broad emission lines is attributed to the scattering of light by a dust (Stein & Weedman, 1976; Neugebauer et al., 1976; Rieke, 1978; Rieke & Lebofsky, 1979; Angel & Stockman, 1980).

With a model in place to explain the masking of broad Balmer lines, the result of rapid orbital speeds close to the black hole, explaining the differences between type 1 and 2 AGN became a problem of geometry. Taking the Occam's razor perspective, the simplest explanation for the the differences between the two types of AGN is for the dusty scatterer to have a toroidal structure, and for the orientation of this torus relative to an observer to vary with the AGN type (Antonucci, 1993). In this model, widely known as AGN unification, the observer of a type 1 AGN has an unobscured view of the broad-line region of the AGN. For a type 2 AGN however, the torus is orientated to the observer such that the ring obscures this

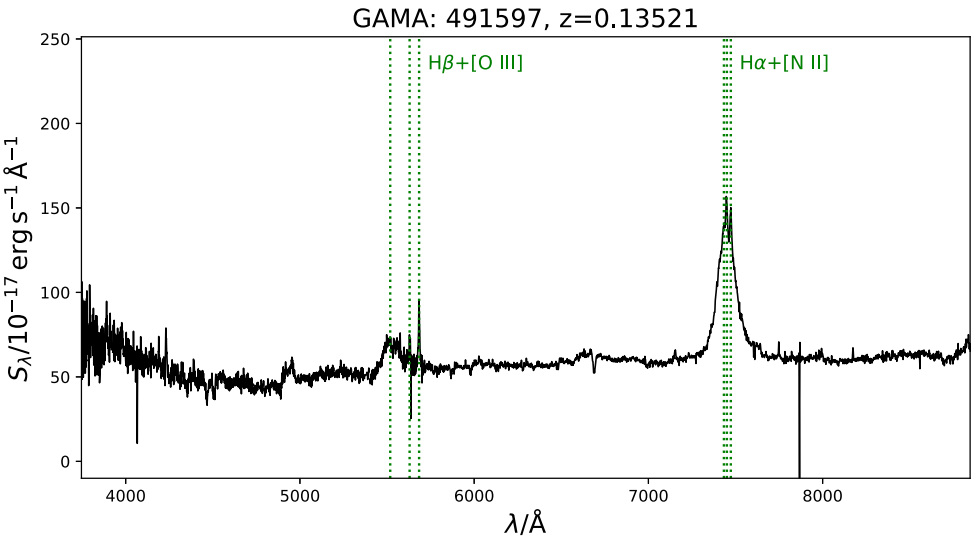

(a)

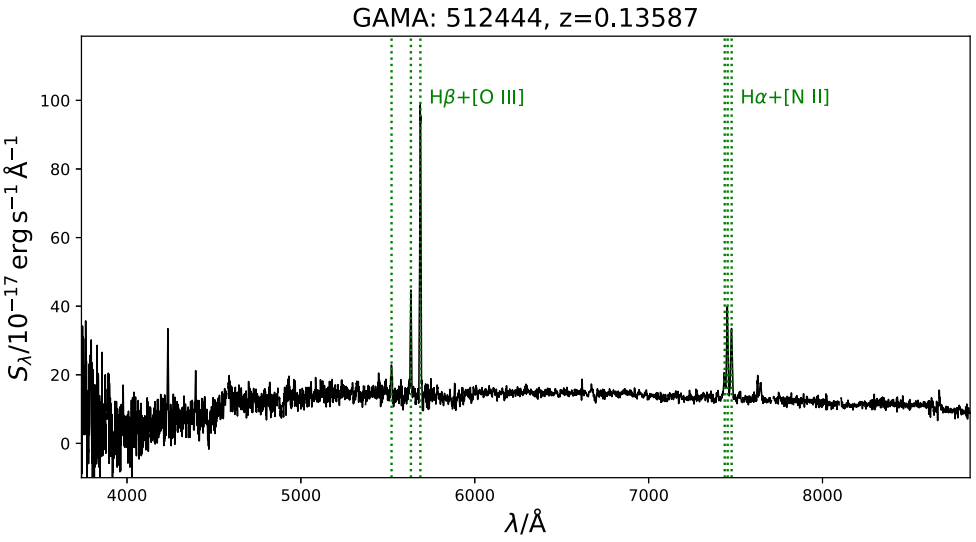

(b)

Figure 1.12: Example optical spectra of AGN from the GAMA survey. Panel (a) shows a typical type 1 AGN spectrum. The Hα, Hβ, and Hγ (at just under 5000 Å) emission lines are substantially broadened. Panel (b) shows a typical type 2 AGN spectrum. No broadening of the Balmer lines is seen, and the only evidence of accretion on to the central SMBH is the presence of the strong [O III] and [N II] ionisation lines. On both spectra, the GAMA ID and redshift of the galaxy is displayed above the spectrum, and the Hβ+[O III] $\lambda\lambda$4959 5007 and Hα+[N II] $\lambda\lambda$6548 6583 emission line complexes are highlighted.

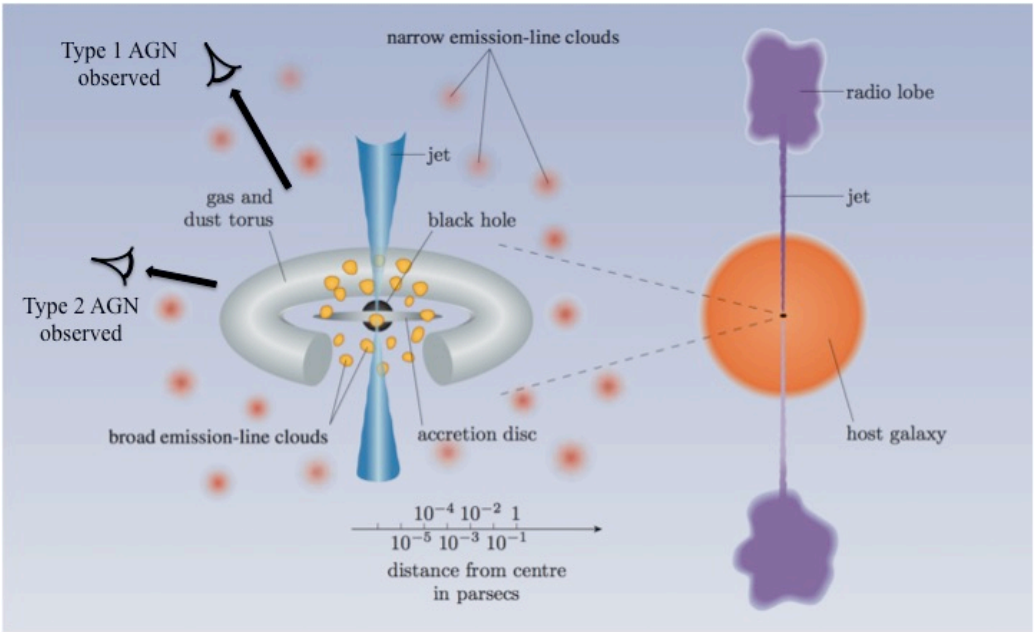

Figure 1.13: Diagram showing a 'toy model' of AGN unification. The left hand side shows a close up of the central engine, indicating the relative positions of the black hole, accretion disk, broad- and narrow-line regions, jets (for RLAGN), and the relative orientations of observers for type 1 and 2 AGN. The right hand side shows the relative positions of jets and radio-lobes in the case of RLAGN. Adapted from Serjeant (2010).

broad line region (see Figure 1.13).

Grand unification

In its simplest form, AGN unification was conceived as a model to explain why the spectra of some AGN exhibit broad Balmer lines, whereas others do not. This has been expanded over the years in order to encompass not only the two types of optical AGN, but the multiple types of radio AGN under a single 'grand-unification' model (Urry & Padovani, 1995). In particular, the emerging picture is one where the type of AGN observed is dependent on two physical parameters.

The mass accretion rate of the black hole, $\dot{M}$ has already been invoked as the crucial attribute in determining between low- and high- excitation radio galaxies. In this scenario, where the jet axis is perpendicular to the line of sight to the observer FR I and FR II morphologies will be observed respectively for inefficient and efficient accretion. In the case where the orientation is such that the jet axis is parallel to the line of sight to the observer, the respective

RLAGN observed will have compact morphologies and be typical of BL Lacertae objects (BL Lacs) and Flat Spectrum Radio Quasars (FSRQs, Urry & Padovani, 1995; Saripalli, 2012).

Taking $\dot{M}$ as the only physical parameter on which AGN classification depends does not explain why some AGN are radio-loud and others radio-quiet. Addressing this requires consideration of the state of the black hole itself. The spin of the black hole may be a key component in the production of a jet, and hence determining whether an AGN is radio-loud or not (McKinney, 2005; Sikora et al., 2007; Tchekhovskoy et al., 2010). Taking the spin parameter of a black hole,

$$a = \frac{Jc}{GM_\bullet^2}, \tag{1.5}$$

where J and $M_\bullet$ are the black hole angular momentum and mass respectively, spins greater than a critical spin parameter ($a_{\rm crit}$) may be necessary for jet production (Maraschi et al., 2012; Gardner & Done, 2018). However, observations of X-ray binaries, which involve accretion on to stellar mass black holes and are thus low mass analogues to AGN, have shown contrasting results with regard to the dependance of jet production on black hole spin. Kolehmainen & Done (2010) and Narayan & McClintock (2012) struggle to constrain the critical spin parameter, with values in the range $0.2 \leq a_{\rm crit} \leq 0.9$. Furthermore, Fender et al. (2010) and Russell et al. (2013) fail to find a correlation between black hole spin and jet power in X-ray binaries. Consequently, although it is widely believed that black hole spin is an important contributing factor, jet production in AGN remains an open problem (Fender, 2016). Should black hole spin be the main factor in jet production, then, taking into account the accretion rate and orientation of the dusty torus relative to the observer, a 'grand-unification' of AGN can be modelled as shown in Figure 1.14. The classification of major types of AGN under such a scheme are shown in Table 1.1

1.4.4 Triggering an AGN

Given that only $\sim$ 10 per cent of galaxies host an AGN (e.g., Martini et al., 2006; Ellison et al., 2011), the obvious question is why do some galaxies host an AGN where others do not? Clearly the process that switches on an AGN cannot be one that is in constant play. Given the physical mechanism that powers an AGN, accretion, either a fuel supply is present, or one

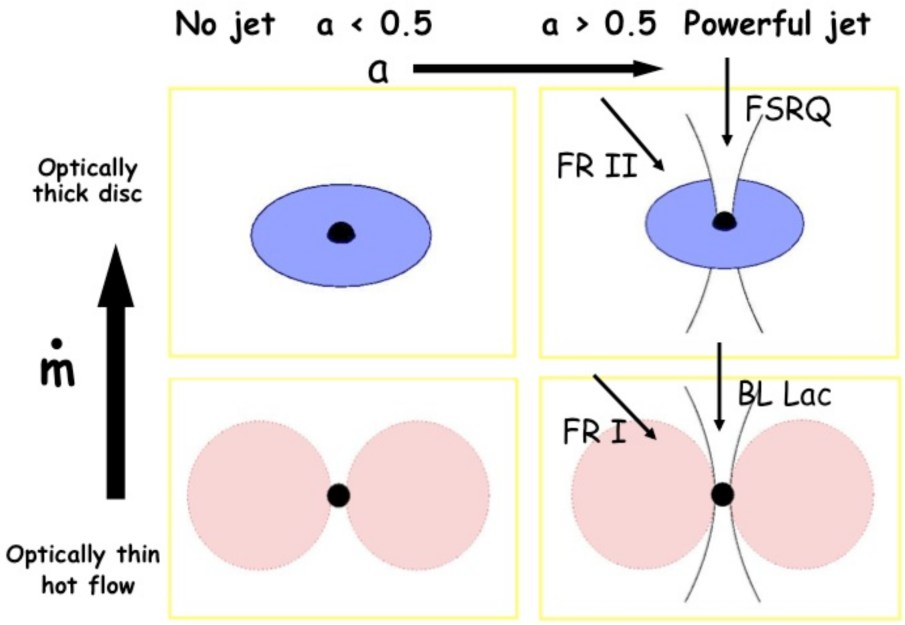

Figure 1.14: A 'toy model' of a grand-unification of AGN, encompassing radio-loud and radio-quiet AGN. Here only two physical parameters determine the type of AGN observed, black hole spin, a, and accretion rate, $\dot{M}$. Other observational differences between AGN are explained by orientation effects. In this model, the type of accretion flow is determined by $\dot{M}$, with high $\dot{M}$ responsible for geometrically thin accretion disks, and low $\dot{M}$ resulting in puffed up advection dominated flows. The presence, or absence, of a jet is determined by a. High black hole spins, i.e., $a > 0.5$ (Maraschi et al., 2012), can produce a jet and hence the AGN will be radio-loud. Image taken from Maraschi et al. (2012).

Table 1.1: Examples of where the main classes of AGN fit, if only approximately, in to the grand-unification model. The top two rows show example of AGN with $\dot{M} > 0.01\dot{M}_{\rm Edd}$, and the bottom two rows give example AGN with $a > a_{\rm crit}$. Naturally the middle row, the HERG population, is a occupied by AGN with both $\dot{M} > 0.01\dot{M}_{\rm Edd}$, and $a > a_{\rm crit}$.

	Jet axis ~ face-on	Jet axis ~ edge-on
Radio-quiet	Sy1	Sy2
HERG	FSRQ	FR II
LERG	BL Lac	FR I

must be introduced in order to trigger an AGN.

Galaxy mergers provide a highly plausible mechanism for AGN triggering by destabilising and introducing gas into the merger participants (e.g., Sanders et al., 1988; Di Matteo et al., 2005). Indeed, galaxies in very close pairs have been shown to have an excess of AGN relative to the rest of the population (Ellison et al., 2011). As close pairs are likely to merge in the near future (Robotham et al., 2014), then this excess of AGN is suggestive that some part of the early merger process provides conditions that are favourable to AGN triggering.

That AGN can be triggered in the early phases of a merger suggests that other externally driven processes may trigger AGN. Galaxy harassment may gravitationally perturb the gas content within a galaxy, and thus provides a plausible AGN triggering mechanism (Moore et al., 1996). Alternatively the tidal interactions from such harassment can leave tidal debris to act as a fuel reservoir an trigger an AGN via this process instead.

When falling into the gravitational potential of a cluster or massive group, galaxies are subject to RPS (Gunn & Gott, 1972). This process, whilst stripping the outer gas from a galaxy, can the destabilise gas within the galaxy and drive it toward the nucleus (Tonnesen & Bryan, 2009). Marshall et al. (2018) have shown using simulations (Croton et al., 2016) that should the ram pressure be more than twice the internal galaxy pressure then this mechanism provides a viable AGN trigger. This is supported observationally by the relative excess of AGN within cluster infall regions (Haines et al., 2012; Pimbblet et al., 2013; Pentericci et al., 2013), and in particular by the high frequency of AGN in 'jellyfish' galaxies, which are known to be experiencing RPS (Poggianti et al., 2017).

Finally, secular evolution may also result in an AGN phase for a galaxy. Processes such as accretion of molecular clouds and instabilities in gas within the galaxy (Bournaud et al., 2011; Gatti et al., 2016) can provide fuel for a potential AGN without need for a major environmental interaction. This provides a conceivable mechanism responsible for the population of AGN observed in cosmic voids (Constantin et al., 2008).

1.4.5 The role of AGN in galaxy evolution

Galaxy growth

An interesting phenomenon in their own right, AGN are also a key stage in the overall evolution of galaxies. It has been observed that the mass of the central black hole correlates with the velocity dispersion of the galactic bulge (see panel a of Figure 1.15 Ferrarese & Merritt, 2000; Gebhardt et al., 2000). It is also known from the Faber-Jackson relation that the velocity dispersion of early type galaxies, analogous to the bulge component of late-type galaxies, is related to the luminosity of the bulge by $L_{\mathrm{Bulge}} \propto \sigma^4_{\mathrm{Bulge}}$ (Faber & Jackson, 1976). Assuming a mass to light ratio, the mass of the bulge component of a galaxy is therefore correlated with the black hole mass (see panel b of Figure 1.15, Magorrian et al., 1998). This relation demonstrates that the SMBH and the host galaxy coevolve.

AGN feedback

The accretion of matter on the SMBH can affect the surrounding galaxy. Observations have shown that AGN preferentially inhabit the 'green valley' region of the colour-mass diagram (Hickox et al., 2009; Schawinski et al., 2010). Because of this, it is widely thought that AGN can quench star formation within a galaxy (Schawinski et al., 2007; Smethurst et al., 2016), and thus account for the shape of the high-mass end of the luminosity function (Croton et al., 2006, and see Figure 1.16). This process, known as AGN feedback, can be the result of either 'quasar-mode' or 'radio-mode' feedback, if not both (Hardcastle et al., 2007). Radio mode feedback occurs during inefficient accretion where jet processes can heat and mechanically remove the gas required for star formation (Ishibashi et al., 2014). Quasar mode feedback also heats the gas required for star-formation, but quasar winds rather than jet activity dominate the mechanical feedback in AGN that are efficiently accreting (Silk & Rees, 1998; Fabian, 2012). Conversely, the shocking and compression of gas can lead to a positive feedback process by triggering star-formation at large distances from the AGN (Ishibashi & Fabian, 2012).

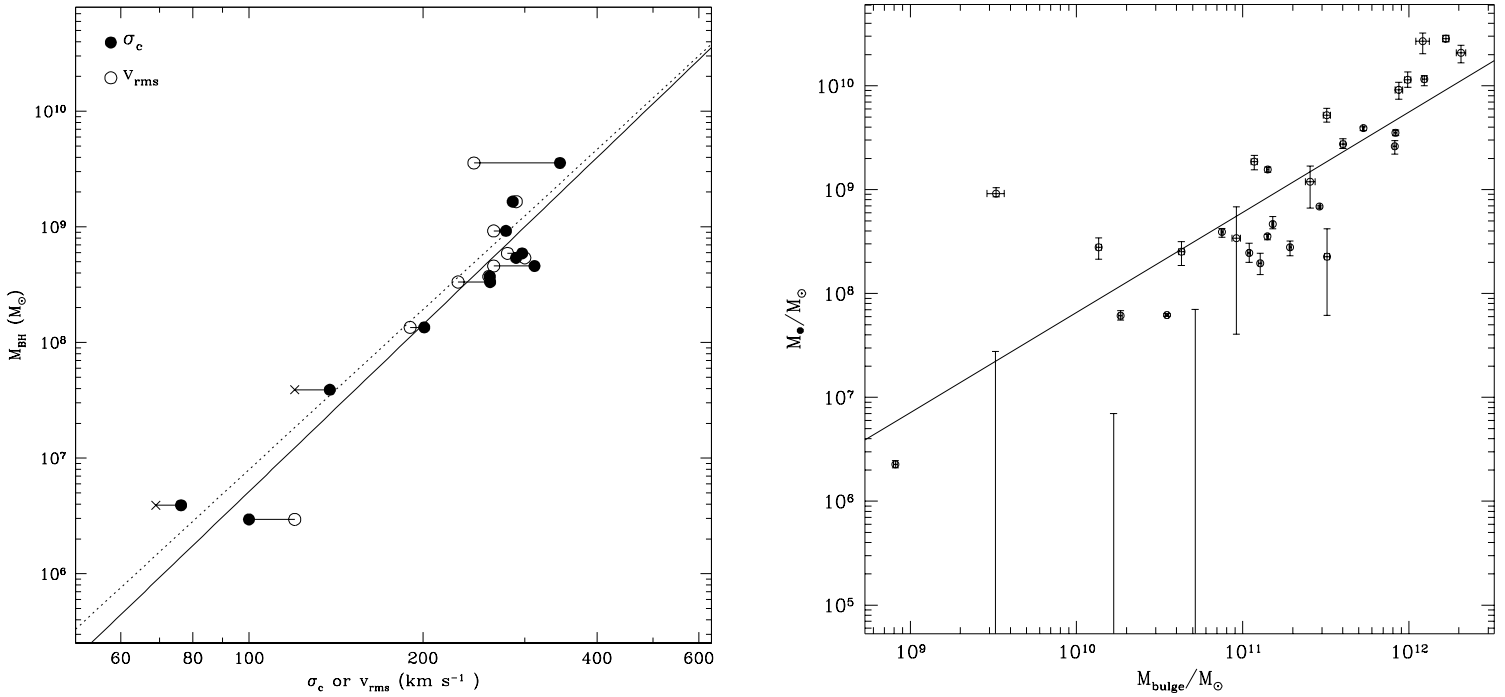

(a) (b)

Figure 1.15: Panel (a), taken from Ferrarese & Merritt (2000) shows the relationship between the mass of the central SMBH and velocity dispersion of the bulge taken from Ferrarese & Merritt (2000). The filled and unfilled circles represent velocities obtained from the the velocity dispersion of the bulge, and the rms velocity inside 1/4 of the effective galactic radius respectively. The solid and dashed lines are the respective relations to black hole mass. Panel (b), taken from Magorrian et al. (1998), shows the relationship between the masses of the central SMBH and the bulge.

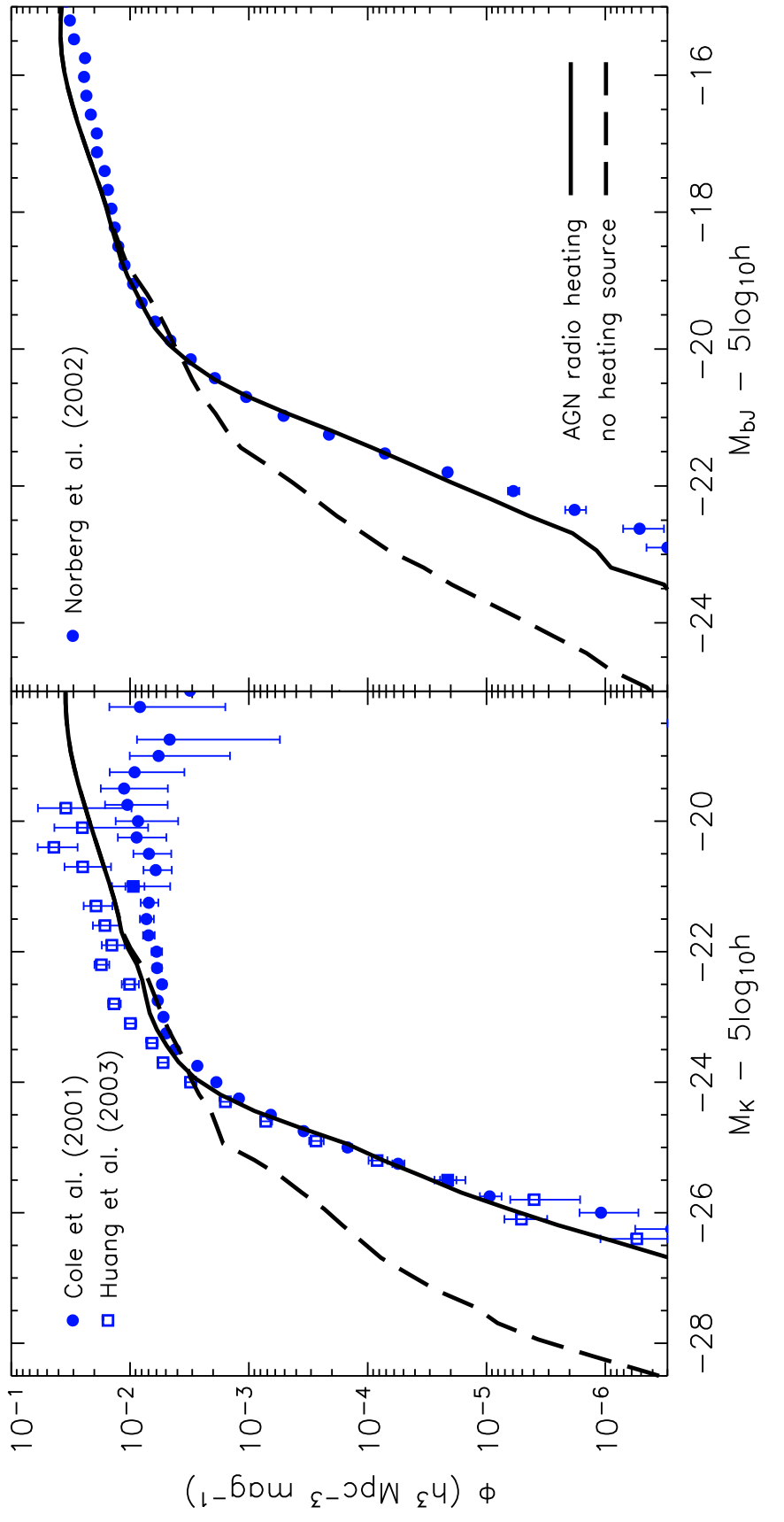

Figure 1.16: The simulated K- and b_J-band luminosity functions with (solid black line) and without (dashed black line) AGN feedback as presented in Croton et al. (2006). In the K-band observations from Cole et al. (2001) and Huang et al. (2003) are shown as blue circles and squares respectively. In the b_J-band observations from Norberg et al. (2002) are shown as blue circles. For both bands, the model with AGN feedback is required to match the observed luminosity function. The GADGET2 code Springel (2005) was used for these simulations. Originally Fig. 8 in Croton et al. (2006).

Effect on the galactic environment

The effect of an AGN is not only confined to its host galaxy. The same jets that are responsible for mechanical feedback, can have lengths on the scale of a few megaparsecs (Bagchi et al., 2014; Clarke et al., 2017) and can thus impact the surrounding galactic environment. AGN feedback may even provide a partial solution to the cooling-flow problem in clusters (Balogh et al., 2001; Peterson & Fabian, 2006; McNamara & Nulsen, 2007). That is to say the energy that AGN feedback supplies to the intra-cluster medium may prevent gas cooling and help to sustain the observed X-ray luminosities of cluster cores.

1.5 The Era of Wide-Field Multi-Object Spectroscopic Surveys

1.5.1 A brief history of survey astronomy

Whilst observations of individual galaxies can provide information about that particular galaxy, such observations do not describe a population of galaxies. To achieve this, large numbers of observations of different galaxies are required. Based on the cosmological principle that the Universe is isotropic (Newton, 1687), then, provided one samples a large enough area of the sky, an un-targeted survey of objects within the sample region should be representative of the population.

The first major attempt at this type of undertaking was by the Palomar Observatory Sky Survey (Palomar Observatory, 1949). This survey used the 48" Schmidt Telescope at the Palomar observatory to photograph the entire sky at $\delta > -27^o$ down to ~ 21 mag (Abell, 1959). By conducting this survey twice, once on red photographic plates and once on blue, basic photometry was able to be performed on objects across $\sim 3/4$ of the sky.

In order to map the local Universe in three dimensions a distance measurement must be obtained. In the closest galaxies this can be achieved using standard candles such as Cepheid variables. However, in more distant galaxies such objects would be too faint to be detected, and Hubble's law must be used to determine the distance to a galaxy by using its redshift. To do this reliably requires the spectrum of the galaxy to be observed. This led to the Centre for Astrophysics Redshift Survey in the late 1970's (Tonry & Davis, 1979), beginning the era of redshift surveys.

By the late twentieth century, redshift surveys had evolved into high-tech projects that would observe hundreds of galaxies at a time (e.g. the 2 degree Field Galaxy Redshift Survey Colless, 1999). This sheer number of simultaneous observations has clear advantages over single observations in that whole populations of galaxies can be studied, and results can be obtained with high statistical confidence. Furthermore, this type of observing program has provided strong evidence in support of the ΛCDM model of the Universe (e.g., Percival et al., 2002; Tegmark et al., 2004; Eisenstein et al., 2005).

Given the constraint on observing time available, and depending on the priorities of a particular survey, two broad classes of spectroscopic survey evolved. Wide and shallow surveys such as the 6 degree Field Galaxy Survey (Jones et al., 2004) focussed on mapping and studying wide areas of the sky but to relatively shallow depths, i.e., their observing time was focused on increasing the survey footprint. Conversely narrow and deep, also known as pencil beam, surveys prioritise observing objects at greater distances and lower luminosities over covering a large region of the sky, e.g. the DEEP 2 survey (Davis et al., 2003).

Two of these spectroscopic surveys have been used to produce the work in this thesis. The Sloan Digital Sky Survey, and the Galaxy And Mass Assembly survey both have specific traits that can be advantageous to modern day extragalactic astronomy. Both these surveys, as well as the advantages and disadvantages associated with using them, are described in depth below.

1.5.2 Sloan Digital Sky Survey

The Sloan Digital Sky Survey (SDSS, York et al., 2000), using the 2.5 m SDSS telescope, is the largest survey undertaken to date. Beginning in 1998 as an imaging survey in five optical and near infra-red bands, u, g, r, i, z centred on $3543, 4770, 6231, 7625$, and 9134 Å respectively. Imaging was obtained across $\sim 15\,000\,\mathrm{deg}^2$ down to $r \lesssim 22$ mag, with deeper imaging obtained in some targeted regions (e.g., stripe 82, Abazajian et al., 2009). This imaging survey acted as the input catalogue for a spectroscopic campaign which would obtain spectra for $> 10^6$ galaxies and quasars with $r < 17.77$ across $8\,000\,\mathrm{deg}^2$ as of the 7th data release (Abazajian et al., 2009).

The spectroscopic observations of SDSS are achieved by using fibre plug plates. The

fibres are positioned manually and cannot be moved between observerations, i.e., each field has its own plug plate. A consequence of this is that pairs of galaxies separated by $< 55''$ cannot both be observed spectroscopically (York et al., 2000). This effect, referred to as fibre collisions, can bias analyses conducted using this dataset where dense galactic environments such as, pairs, groups or clusters, are the target of the investigation (Patton & Atfield, 2008).

1.5.3 Galaxy And Mass Assembly

The Galaxy And Mass Assembly survey (GAMA, Driver et al., 2011; Liske et al., 2015) is a collection of surveys across multiple wavelengths and includes the GAMA spectroscopic survey. Throughout this thesis the acronym 'GAMA' is used explicitly to refer to the spectroscopic survey component unless otherwise stated. The GAMA spectroscopic campaign ran from 2008 until 2014, using the 2dF/AAOmega spectrograph (Saunders et al., 2004). Over 250 000 galaxies with $r < 19.8$ were observed across 286 $\deg^2$ of the equatorial and southern sky.

Although the survey footprint of GAMA is far smaller than that of SDSS, and naturally the number of observed targets is lower, there are two features of GAMA that make a better tool to use than SDSS for certain types of research. By observing targets that are two magnitudes fainter, GAMA can probe to lower stellar masses than SDSS for a given redshift limit (Taylor et al., 2011). Alternatively, for a given stellar mass limit, GAMA can observe to higher redshifts than SDSS.

The second advantage that GAMA has over SDSS is one of spectroscopic completeness. GAMA altered the position of spectroscopic fibres between re-observations of the same field. Thus, when the same field is re-observed, the second galaxy in a pair can be observed circumventing the fibre-collision problem. This is particularly true in the 180 $\deg^2$ of the GAMA equatorial regions (G09, G12, G15) that are used in this thesis. In these regions, each field is reobserved at least 6 times, and often more than 10 times for densest areas of sky that are preferentially targeted (Liske et al., 2015). This leads to a uniform spectroscopic completeness of > 98 per cent at $r < 19.8$. In contrast SDSS has ~ 94 per cent completeness at $r < 17.77$ across the survey footprint, but this decreases rapidly in densely populated regions of the sky (Strauss et al., 2002; Patton & Atfield, 2008).

1.6 The Scope of This Work

In Chapter 2, optical AGN unification is tested by an analysis of the type 1 and 2 AGN in galaxy pairs. This work is motivated by the premise that, should the orientation of the AGN relative to the observer be the primary property that determines AGN type, then one would expect like close environments for both types of AGN. However, some recent works (e.g., Villarroel & Korn, 2014; Jiang et al., 2016) have observed this not to be the case and hence questioned AGN unification. Exploiting the extremely high spectroscopic completeness of GAMA to provide a highly accurate catalogue of galaxy pairs, while using a double Gaussian emission line fitting routine to classify AGN to a high degree of accuracy, provides a high fidelity sample of broad- and narrow-line AGN in galaxy pairs. Chapter 2 therefore provides an independent test of the environment of type 1 and 2 AGN, and hence AGN unification, to previous studies that have had to rely on lower quality data. This work has been published as Gordon et al. (2017).

Chapter 3 tests the effect of galaxy location within large-scale structure on the triggering and inhibition of optically selected AGN. Previous works have shown that for massive galaxies in clusters, an AGN can be triggered on infall by, e.g., RPS and galactic interactions, whereas extreme RPS coupled with strangulation can inhibit AGN in cluster cores (Haines et al., 2012; Pimbblet et al., 2013; Poggianti et al., 2017). By once again exploiting the high spectroscopic completeness of GAMA, this Chapter represents the first in depth analysis of AGN location within the projected phase-space of galaxy groups to test if AGN evolve the same way in the group environment as in clusters. Covering the halo mass function in the range $11.5 \lesssim \log_{10}(M_{200}/\mathrm{M}_{\odot}) \lesssim 14.5$, this work includes the whole group mass function up to, and including, low mass clusters. It is important to distinguish that these are optically selected AGN, as that distinction implies an efficient accretion mechanism at play in the central engine. This Chapter makes no attempt to study the effect of group environment on RLAGN where the accretion mode need not be as efficient. This Chapter has been published as the journal article Gordon et al. (2018).

In Chapter 4 an outstanding problem in AGN science is addressed, namely what is the major fuelling pathway for LERGs? Given the inefficient accretion mode attributed to these

AGN, these galaxies are hypothesised to either be drip-fed by a low-impact external mechanism such as minor-mergers or cooling flows, or by internal stochastic processes (Hardcastle et al., 2007; Ellison et al., 2015). In this Chapter low-surface brightness tidal features that are the tell-tale sign of recent minor-merger history are looked for in order to test whether these events do indeed trigger LERGs. This work takes advantage of the large sky-coverage and overlap between several large surveys, including SDSS for spectral coverage, deep optical imaging from the Dark Energy Camera Legacy Survey, and radio observations from the Very Large Array.

Finally, Chapter 5 summarises the work presented in this thesis before going on to look at future directions for this line of research. In particular, Chapter 5.3 compares the strengths and weaknesses of different survey designs for large-scale spectroscopic surveys. This is then used to make predictions for the upcoming Taipan galaxy survey which exploits the contrasting strengths of both SDSS and GAMA. Some of the predictions made here are published in Section 3.4.1 of da Cunha et al. (2017).

2. Using Galaxy Pairs to Test AGN Unification

"Oh, people can come up with statistics to prove anything. Fourfty per cent of all people know that."

– Homer Simpson, *Homer the Vigilante (The Simpsons, 1994)*

2.1 Prologue

The following Chapter is the published work *"Galaxy And Mass Assembly (GAMA): active galactic nuclei in pairs of galaxies"*, MNRAS **465**, 2671 (Gordon et al., 2017). This paper was led by myself, and co-authored with, in authorship order, Matt Owers, Kevin Pimbblet, Scott Croom, Mehmet Alpaslan, Ivan Baldry, Sarah Brough, Michael J. I. Brown, Michelle Cluver, Chris Conselice, Luke Davies, Benne Holwerda, Andrew Hopkins, Madusha Gunawardhana, Jonathan Loveday, Ned Taylor, and Lingyu Wang. My responsibilities on this paper were driving the direction of the paper, data reduction and analysis, and the writing up of the paper, accounting for $\gtrsim$ 85 per cent of the workload. Chapter 2.3 introduces the GAMA emission line measurements catalogue SpecLineSFRv05 produced by Matt Owers and used in this work. The remaining co-authors provided scientific feedback on draft versions of the paper, and contributed to the GAMA observations and data products used in this work. Some minor rewording has taken place to reflect the nature of the work as part of a thesis rather than journal article (e.g., 'Section' is reworded as 'Chapter'), and, for that reason, the abstract for the paper is not reproduced here.

2.2 Introduction

Type 1 and Type 2 (T1 and T2 respectively hereafter) active galactic nuclei (AGN) are defined by the presence or absence of broad emission lines in their spectra, respectively. When Miller & Antonucci (1983) discovered the presence of hidden broad emission lines in the polarised spectra of T2 Seyfert galaxies it was suggested that a dusty torus around the active nucleus

was responsible for scattering the light, resulting in the so called “unified model of AGN". In the most simple interpretation of AGN unification, both T1 and T2 AGN are expected to be the same type of object and only the orientation of a circumnuclear dusty torus differs relative to the observer (Antonucci, 1993). If the unified model is a complete description then all T2 AGN should contain hidden broad lines. Problematically for AGN unification, these have only been discovered in approximately 50% of T2 AGN (Tran, 2001). This suggests that at least some T2 AGN are fundamentally different to T1 AGN. However, the lack of hidden broad lines in all T2 AGN might be solely explained by variable homogeneity and covering or obscuration factor of the dusty torus around the central engine (Elitzur, 2012).

If the differences in observed properties of T1 and T2 AGN are simply due to the orientation of the torus with respect to viewing angle, as predicted in the AGN unification scheme, then there should be no significant difference between the external environment of these two types of AGN. However, there have been observations that demonstrate that T1 and T2 Seyfert galaxies (Sy1 and Sy2 respectively hereafter) are not found in identical environments. Dultzin-Hacyan et al. (1999); Koulouridis et al. (2006) and Jiang et al. (2016) have all found that Sy2 galaxies are significantly more likely than Sy1 galaxies to be in a galaxy pair with a projected separation of less than 100 kpc h^{-1}. Furthermore, Krongold et al. (2002) found that Sy2s reside in similar environments to galaxies in the IRAS bright galaxy sample (Soifer et al., 1989; Sanders et al., 1995) whereas Sy1s do not. Krongold et al. (2002) and Koulouridis et al. (2006) suggest that this may imply an evolutionary path as a result of galaxy interactions from star-forming, to Sy2 through to Sy1 post interaction, and thus implying that AGN unification is an inaccurate model.

As well as the simple likelihood of an AGN to be of a particular type dependent upon the presence or absence of a nearby galaxy, Villarroel & Korn (2014) have conducted a thorough census of the properties of AGN neighbours. By using the Sloan Digital Sky Survey (SDSS, York et al., 2000) seventh data release (DR7, Abazajian et al., 2009) they found that in AGN-AGN pairs the neighbour of a T2 AGN was significantly more likely to also be a T2 AGN at projected separations below 200 kpc, further strengthening the validity of prior observations (e.g., Dultzin-Hacyan et al., 1999; Koulouridis et al., 2006; González et al., 2008; Jiang et al.,

2016). Further to this Villarroel & Korn (2014) found that the colour of the neighbouring galaxies differed with AGN type; the neighbours of T1s being redder than the neighbours of T2s. This implies that either the star-formation rate, metallicity or stellar population age of the neighbouring galaxy may affect the type of AGN triggered by the interaction.

As mergers are believed to be a primary source of fuel for AGN (Barnes & Hernquist, 1991), studying interacting galaxies where one galaxy hosts an AGN provides an opportunity to investigate how nuclear activity evolves from its earliest stages. As interacting galaxies appear in the sky as close pairs, a major drawback facing some previous studies using projects such as the SDSS (e.g., Villarroel & Korn, 2014) is the inability to detect the closest pairs of galaxies as a result of spectroscopic fibre collisions (Blanton et al., 2003). In these situations, including the work by Villarroel & Korn (2014), photometric data is often used to support the spectroscopic observations. This can result in less accurate z-space separations of the pairs being measured and a lack of emission line data to classify potential AGN. SDSS DR7 (York et al., 2000; Abazajian et al., 2009) contains about 1,050,000 galaxy spectra accounting for 94% of potential targets with the remainder being lost to fibre collisions (Strauss et al., 2002). Indeed, in dense regions of the sky, fibre collisions severely hamper the completeness of the SDSS spectroscopic catalogue (Patton & Atfield, 2008).

Surveys such as the Galaxy And Mass Assembly (GAMA) survey (Driver et al., 2011; Liske et al., 2015) circumvent the fibre collision problem by observing each field of view multiple times, moving the fibres between observations (Robotham et al., 2010). This results in a far more complete sample of close pairs with which to study galaxy interactions than is possible in spectroscopic surveys that do not use this technique. Indeed, the completeness of GAMA has already been used to better constrain the effect of close environment and galaxy interactions on galaxy evolution (Casteels et al., 2014; Robotham et al., 2014; Alpaslan et al., 2015; Davies et al., 2015, 2016). Given the questions asked of AGN in unification from observations over the last few decades, we aim to further scrutinise this widely accepted model by taking advantage of the high spectroscopic completeness of GAMA in order to thoroughly test the environment of broad and narrow line AGN. Furthermore, we investigate whether or not AGN with a single broad Balmer emission are indeed the same as AGN with

multiple broad Balmer emission lines by comparing how these populations behave under a range of environmental probes.

In Chapter 2.3 of this paper we describe the spectral emission line fitting method used to produce the data set from which we select our AGN. Chapter 2.4 outlines our method of selecting AGN using the resultant emission line catalogue and details how we select galaxy pairs. In Chapter 2.5 we analyse the environment of our AGN and discuss our observations which we compare to other observations in Chapter 2.6. Our conclusions are stated in Chapter 2.7. Throughout this chapter we use a standard flat ΛCDM cosmology: $h = 0.7$, $H_0 = 100h$ km s^{-1}Mpc^{-1}, $\Omega_M = 0.3$, $\Omega_\Lambda = 0.7$.

2.3 Data

The GAMA survey was undertaken between 2008 and 2014 (Driver et al., 2011; Liske et al., 2015) at the Australian Astronomical Observatory (AAO) using the 3.9m Anglo-Australian Telescope. GAMA obtained spectra for > 250000 galaxies with $r < 19.8$ mag using the 2dF/AAOmega spectrograph (Saunders et al., 2004). For each target the 2dF/AAOmega spectrograph obtains a blue spectrum covering the range 3750-5850Å and a red spectrum covering 5650-8850Å. These are spliced together at 5700Å resulting in a total spectrum, which has a mean resolution of $R \approx 1300$, with an observed wavelength range of 3750-8850Å (Hopkins et al., 2013). Covering ≈ 260 square degrees across 5 regions (G02, G09, G12, G15 and G23) GAMA is > 98% complete in the 3 equatorial regions G09, G12 and G15 (Liske et al., 2015) making observations from these regions highly valuable for observing close pairs of galaxies.

2.3.1 Emission line modelling

To select our AGN we require accurate emission line measurements for the spectra of the galaxies within GAMA. To this end we present and then use the SpecLineSFRv05 catalogue that provides line flux and equivalent width measurements for GAMA II spectra by modelling emission lines with either a single or double Gaussian profile. SpecLineSFRv05 is constructed by selecting the spectra in the GAMA SpecAllv27 dataset that have a redshift quality $nQ > 1$

(indicating a redshift has been measured, for a full description of redshift quality in GAMA see Driver et al., 2011; Liske et al., 2015) and a redshift $0.002 < z < 1.35$. The catalogue contains 427,829 entries and includes repeated measurements for some targets. In cases where objects have several spectra, the best redshift was used for the line measurements. The catalogue excludes a small number of targets which either do not have spectra available, or were taken with the Liverpool Telescope (Steele et al., 2004). Also excluded are additional spectra from the VVDS (VIMOS VLT Deep Survey, Le Fèvre et al., 2005, 2013).

This version of the resultant database is the first GAMA II emission line measurements catalogue (previous versions of the GAMA emission line measurement database have been for GAMA I, Gunawardhana et al., 2011) and differs from previous versions in that it also provides fits for spectra from SDSS, the 2 degree Field Galaxy Redshift Survey (2dFGRS, Colless, 1999), the 6 degree Field Galaxy Survey (6dFGS, Jones et al., 2004), the WiggleZ survey (Drinkwater et al., 2010), the Millennium Galaxy Catalogue (MGC, Liske et al., 2003), the 2dF-SDSS LRG and QSO survey (2SLAQ, Cannon et al., 2006; Croom et al., 2009) and the 2dF QSO redshift survey (2QZ, Croom et al., 2004). Each spectrum is fitted across 5 regions containing 12 physically important emission lines. The continuum in each of these regions is modelled as a straight line. The fitting is done with the IDL code MPFITFUN (Markwardt, 2009) which uses a Levenberg-Marquardt non-linear least squares minimisation to identify the best-fitting parameters for the model given the data and its associated uncertainties. The fitted spectral regions are:

- 3626-3779Å to model the [O II] lines at 3726Å and 3729Å.
- 4711-5157Å to model Hβ and the [O III] lines at 4959Å and 5007Å.
- 6270-6394Å covering the [O I] emission lines at 6300Å and 6364Å.
- 6398-6710Å modelling Hα and the [N II] lines at 6548Å and 6583Å.
- 6616-6831Å to model [S II] lines at 6716Å and 6731Å.

The resultant catalogue is organised into 3 data tables. The first table, SPECLINEGAUSSFITSIMPLE, contains line measurements derived from single-Gaussian fits as well as the strength

of the 4000Å break, measured using the method of Cardiel et al. (1998) using the continuum band definitions given by Balogh et al. (1999). There is also an estimate of the S/N per pixel in the continuum measured in the 153Å window from 6383 - 6536Å. This is 12Å blue-ward of the [N II](6548Å) line and is measured on the redshifted spectrum.

The second table, SpecLineGaussFitComplex, contains more complicated fits to the regions containing the Hα and Hβ lines. For Hα and Hβ, a second Gaussian component is added that may be either in absorption or broad emission. Model selection scores are described below (Chapter 2.3.3) and can be used to select those spectra where this extra component is justified given the improvement in the fit due to the extra components.

The third table, SpecLineDirectSummation, contains direct summation equivalent widths for 51 absorption and emission line species. The equivalent widths and their associated uncertainties are measured using the techniques outlined in Cardiel et al. (1998). There are no corrections made due to the effects of velocity dispersion, nor are there attempts to place Lick index measurements onto the Lick system.

2.3.2 Gaussian line fitting procedure

The fitting begins with a simple straight line fit to the spectral region of interest (listed above) and increases in complexity depending on the line species. Regions containing lines that are expected to only occur as narrow emission lines (e.g., [O II], [S II] and [O I]) have only one level of complexity above that of a straight line fit (the inclusion of the Gaussian lines for the narrow emission). For the regions containing Hα and Hβ, there are six different manifestations of absorption and emission. For example, the Hα + [N II] $\lambda\lambda$6548, 6543 region can contain the following combinations in increasing complexity (likewise for Hβ + [O III] $\lambda\lambda$4959, 5007):

- No emission or absorption, just continuum.
- Hα in absorption and no [N II] emission.
- [N II] λ6548 + Hα + [N II] λ6583 all with narrow emission.
- [N II] λ6548 + [N II] λ6583 in emission + Hα in absorption.
- [N II] λ6548 + [N II] λ6583 in emission + Hα in emission and absorption.

- [N II] λ6548 + [N II] λ6583 in emission + Hα in narrow plus broad emission.

Each of the above fits are performed on the data and a model selection score is given for the more complex model compared with the simpler one (see below). For models with the same number of fitted parameters, the model with the lowest χ^2 value is chosen. Examples of this line fitting for narrow and broad emission lines are shown in Figures 2.1 and 2.2.

In order to fit the model to the line region the following limits are set:

- Line position is limited to be within 200 km s^{-1} of the expected position given the redshift of the galaxy (the redshift has the heliocentric correction removed and SDSS spectra are converted from vacuum to air wavelengths).

- For the narrow emission line components, the width of the Gaussian, σ, is constrained to be in the range $0.75\sigma_{\rm inst} < \sigma < \sqrt{500^2 + \sigma^2_{\rm inst}}$ where $\sigma_{\rm inst}$ is the instrumental resolution of the spectrum in km s^{-1}. This constrains the width of the narrow-line components to be less than 500km s^{-1}.

- The boundaries on the amplitude for the line are estimated from the range in data near the expected position of the line. A small negative value is allowed for emission-only lines (e.g., [N II], [O II] etc.) in order to assess line detection limits.

- For broad emission lines, σ is constrained to be in the range $\sqrt{500^2 + \sigma^2_{\rm inst}} < \sigma < \sqrt{5000^2 + \sigma^2_{\rm inst}}$. A larger parameter space is allowed for the position of the broad component (400 kms^{-1}). The initial guess for intrinsic dispersion is 1000 km s^{-1}.

- For all doublet lines, the position and velocity dispersion of the weaker line is tied to that of the stronger line. Given that the [O II] doublet is rarely resolved, the amplitudes for [O II] $\lambda\lambda$3726, 3729 are tied to the ratio [O II] λ3726 = 0.35 $\times$ [O II] λ3729.

This method provides equivalent width (EW) and flux (F) for the fitted lines and are derived by:

$$EW = \frac{F}{C} = \frac{\sqrt{2\pi}A\sigma}{C} \tag{2.1}$$

Where A is the amplitude of the Gaussian, σ is the line dispersion (including instrument dispersion) and C is the continuum at the position of the emission line given by the equation

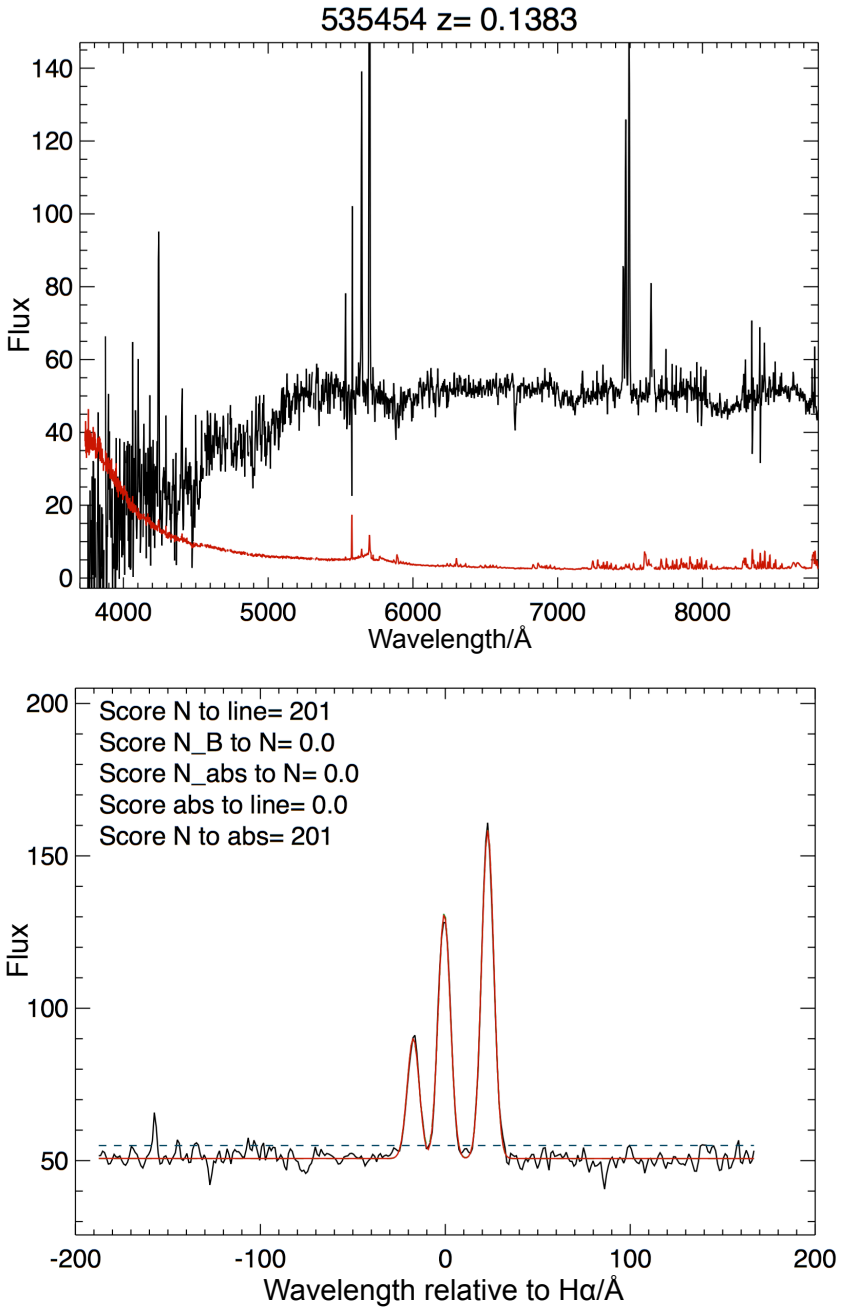

Figure 2.1: Example of Gaussian fit to a narrow Hα emission line. Top: AAOmega spectrum of the galaxy (GAMA CATAID = 535454). Bottom: fitting of the 6398-6710Å region containing Hα and the two [N II] lines. The scores in the top left of the bottom panel are the model selection scores (see Chapter 2.3.3) for the different complexities of fitting model. 'Line' is the continuum only model, 'N' is the narrow emission model, 'N_B' is the narrow + broad emission model, 'abs' is the absorption only model and 'N_abs' is the narrow emission + absorption model. The score of 201 involving the the narrow model and either just the continuum or absorption 'N to line' and 'N to abs' of 201 indicates that this is this is the preferred fit.

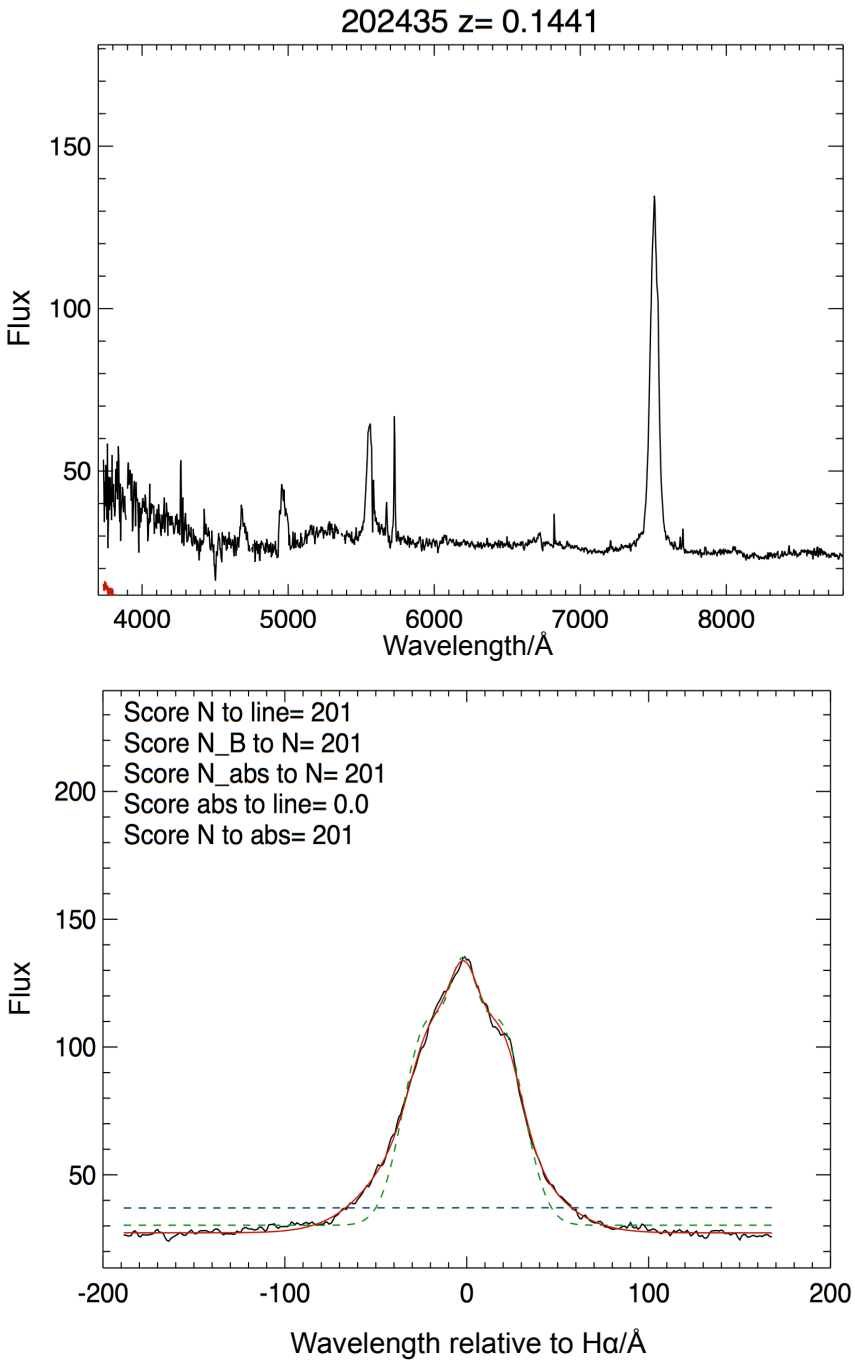

Figure 2.2: Example of Gaussian fit to a broad Hα emission line. Top: AAOmega spectrum of the galaxy (GAMA CATAID = 202435). Bottom: fitting of the 6398-6710Å region containing Hα and the two [N II] lines. The score of 201 involving the the most complex model 'N_B to N' of 201 indicates that this is this is the preferred fit (see Chapter 2.3.3).

of the linear fit to the continuum. The uncertainties on measurements are propagated in quadrature from the errors of their dependences. That is to say for EW, $\Delta EW = |EW| \times \sqrt{(\Delta A/A)^2 + (\Delta\sigma/\sigma)^2 + (\Delta C/C)^2}$. All the equivalent widths are corrected by $(1+z)$ and are thus rest-frame measurements.

2.3.3 Model selection

Given the increasing complexity of the models, it is important to ensure that the data are not being over-fit because of the extra freedom allowed by the additional model parameters. There are many model selection methods, each with its own advantages and drawbacks. In an attempt to overcome the drawbacks of different methods, three model selection methods have been used to give a single model selection score. Two of the model selection methods have their roots in Bayesian statistics and are estimators of the 'Bayes Factor'. Since a full Bayesian approach would be rather time-consuming for 400,000 spectra, two analytic approximations are used to estimate the Bayes Factor. The first is the change in the Bayesian information criterion (ΔBIC), where the BIC for each model is given by:

$$\mathrm{BIC} = \chi^2 + d(\ln N_{\mathrm{data}} - \ln 2\pi) \tag{2.2}$$

Where d is the number of free parameters of the fit, N_{data} is the number of data points and $\Delta\mathrm{BIC} = \mathrm{BIC}(1) - \mathrm{BIC}(2)$ for models 1 and 2. As can be seen, the BIC strongly penalises models with additional parameters. The second Bayes factor estimator is the Laplacian approximation (BF) given by:

$$\mathrm{BF} = \frac{P(D|M1)}{P(D|M2)} = \frac{\int P(D|P1, M1) \times P(P1|M1) dP1}{\int P(D|P2, M2) \times P(P2|M2) dP2} \tag{2.3}$$

$P(D|M1)$ is the marginal likelihood for model 1, D is the data, and $P1$ is the parameter of model 1. Under the assumption that the probability distribution of $P(D|P1, M1)$ has a well defined peak around the best-fitting parameters and the shapes of the distribution are approximately Gaussian, Laplace's approximation can be used (Kass & Raftery, 1995) to simplify the integrals to:

$$\begin{aligned}\int P(D|P1, M1) \times P(P1|M1) dP1 &= P(D|M1) \\ &= 2\pi^{d1/2} \times \sqrt{\Sigma 1} \times \exp(-\chi(1)^2/2) \times P(P1|M1)\end{aligned} \tag{2.4}$$

Table 2.1: Using −2 log(BF) and ΔBIC to compare evidence in favour of model one over model 2.

−2 log(BF) and ΔBIC	Evidence favouring $M1$ over $M2$
0 to 2	Not stong
2 to 6	Positive
6 to 10	Strong
> 10	Very strong/decisive

$d1$ is the number of free parameters in the model $M1$, $\Sigma 1$ is the covariance matrix for the best fitting model as determined by 'mpfitfun', and the prior $P(P1|M1)$ is a uniform prior defined by the limits on parameters $P1(1), P1(2)...P1(d1)$.

Models that have larger $P(D|M)$ values are preferred. For this method, the addition of extra model parameters is strongly penalised by the $P(P|M)$ term which, for uniform priors, drops significantly due to the additional volume probed by the parameter space in the more complicated model. The Bayes Factor and ΔBIC have the proportionality $-2\log(\mathrm{BF}) \approx \Delta\mathrm{BIC}$ so the same criteria can be used to evaluate the strength of evidence of M1 vs M2 and vice-versa. The criteria are taken from Kass & Raftery (1995) and are cast in terms of comparing model M1 to M2 in Table 2.1.

Aside from the two methods above, we incorporate the F-test using the algorithm of Markwardt (2010). This tests whether the change in the χ^2 value is significant given the change in the DOF for the more complicated model and returns a p-value as an indicator of significance. For the purposes of model selection, only when $p < 0.01$ is $M1$ favoured over $M2$. The three methods are used to give a single score (mod_score) that can be used as an indicator that the more complicated model is favoured over the simpler model (e.g., a double-Gaussian over a single-Gaussian fit for Hα). The score is determined as, for $x = -2\log(\mathrm{BF12}), \Delta\mathrm{BIC}$:

- If $2 \leq x < 6$, mod_score = mod_score + 1
- If $6 \leq x < 10$, mod_score = mod_score + 10
- If $x \geq 10$, mod_score = mod_score + 100

In addition to this if the p-value from the F-test is less than 0.01, then 1 is added to the mod_score. For example, if both $-2\log(\mathrm{BF12})$ and ΔBIC were greater than 10 and the F-test gave a p-value of less than 0.01 then the resultant mod_score would be the maximum possible 201 indicating that model 1 is strongly favoured over model 2. As each model is compared to every other model, the comparison of the most complex of these models where the comparison score is 201 is the preferred model.

2.4 AGN and Galaxy Pairs in GAMA

2.4.1 Spectroscopic classification of AGN

The classification of AGN is not a discrete process, there exists a continuum between the truly broad line QSO's, which exhibit strong broad emission in Hα, Hβ, Hγ and Hδ, through to the narrow line T2s, which exhibit no observed broad component in their permitted emission lines (see Figure 2.3). As such we create 3 catalogues of AGN based on the emission line properties taken from the GAMA emission line properties database (described in Chapter 2.3). Only data from SDSS and AAOmega obtained spectra are used as only these spectra have been flux calibrated (Hopkins et al., 2013). Catalogue 1 consists of 'bona fide' type AGN that have broad emission components detected for both Hβ and Hα. Catalogue 2 contains intermediate type AGN that show evidence for broad-line emission, but the total flux in the emission lines are dominated by the narrow component. These AGNs are often referred to as type 1.5, 1.8 and 1.9 AGN (Osterbrock, 1981). Our final AGN catalogue contains the T2 AGN that are classified based on their emission line ratios as per Kewley et al. (2001). Example spectra from each of these catalogues is shown in Figure 2.3.

In order to ensure that the Hα line is detected reliably by the AAOmega spectrograph we limit our study to a redshift of $z < 0.3$. To ensure only reliable spectra are used we select only those with $nQ \geq 3$ indicating that there is a $> 90\%$ chance that the redshift is accurate (Driver et al., 2011; Liske et al., 2015). Furthermore, we require S/N > 3, S/N is measured as Flux/ΔFlux for all emission lines required to classify a galaxy as an AGN type. To ensure in cases where the red and blue components of 2dF/AAOmega spectra have not been spliced cleanly that this splicing does not result in a false detection of a Hβ broad line, we exclude

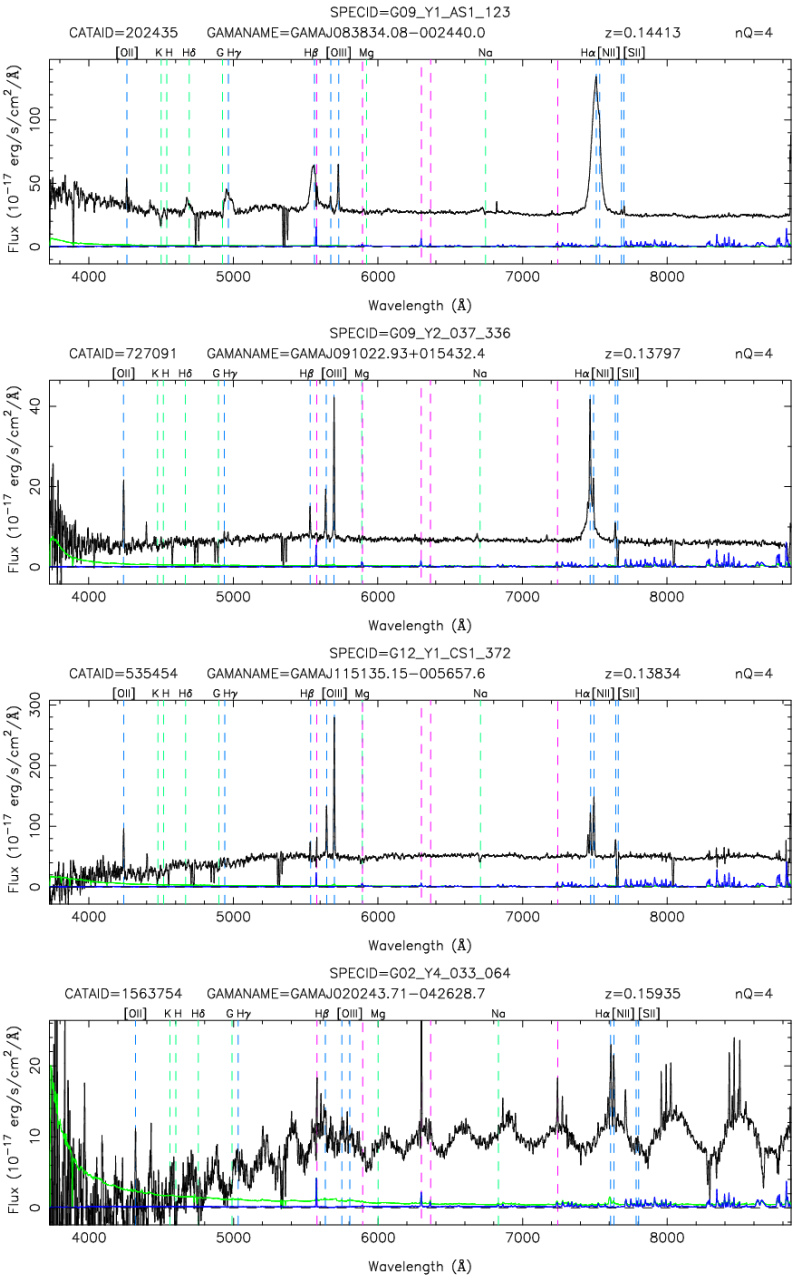

Figure 2.3: From top to bottom: A typical 'bona fide' T1 AGN spectrum; a typical 'intermediate' type BLAGN spectrum; a typical T2 AGN spectrum; and example AAOmega spectrum affected by time dependent fringing, 19% of our selected broad line spectra were discarded from our data as a result of this. These images are obtained from the GAMA (Driver et al., 2011; Liske et al., 2015) 'single object viewer' online tool.

all galaxies with $0.170 < z < 0.175$ from selection. In order to provide a clean detection of the Hα line that is free from telluric contamination by the A-band Fraunhofer lines we also exclude galaxies with $0.157 < z < 0.163$.

To select our bona fide T1 catalogue we select galaxies that have a broad component, i.e. a FWHM $\geq$ 1200 km s^{-1}, in Hα and Hβ. This is selected for by requiring that for Hα and Hβ the complex double Gaussian model is preferred to more simple emission line fits. We require that the flux of the broad component of a line be greater than the flux from the narrow component. Also, in agreement with Osterbrock (1981), we select only galaxies where the Hα:Hβ broad flux ratio is less than 5 to be classified as bona fide T1 AGN. For quality control purposes we select only from spectra where for both Hα and Hβ the amplitude and dispersion of the broad component are not pegged at the parameter boundaries.

To select our intermediate type AGN we require that at least the Hα line has a broad component, i.e. that the complex double Gaussian model is preferred for this line. As with the T1 selection we require for quality control purposes that the amplitude and dispersion of the broad component Gaussian of Hα to have not pegged at the parameter boundaries. Furthermore, to ensure that a broad Hα line is the result of nuclear activity we require that there is a significant [O III] λ5007 detection. The [O III] λ5007 is considered to be an indicator of nuclear activity (Pimbblet et al., 2013). Specifically [O III] λ5007 has been shown to be consistently present in AGN selected by hard X-ray emission (Heckman et al., 2005) and indeed [O III] λ5007 luminosity scales with X-ray luminosity suggesting it is a useful indicator of AGN power (Heckman et al., 2005; Ueda et al., 2015). We define a significant detection of [O III] λ5007 in this context to be an equivalent width greater than 3Å.

Approximately 5% of AAOmega spectra suffer from a time-dependent fringing artefact (Hopkins et al., 2013, shown in Figure 2.3). For the purposes of emission line modelling this can mimic the presence of a broad line. Therefore, to remove any affected spectra we have selected, the broad line AGN (BLAGN; T1bona fide and intermediate) catalogues were visually inspected for this and the affected spectra discarded. We found that 19% of our broad line AGN were affected and therefore discarded. Further to this 6 of our intermediate type AGN were removed from consideration due to spectra that showed evidence of contamination

by another object, e.g., a nearby bright star.

To select the T2 catalogues we select from those galaxies not selected as BLAGN and require that the amplitude, dispersion and position of the narrow Gaussian have fitted successfully for Hβ, [O III] λ5007, Hα and [N II] λ6583. We correct the flux measurements of the Balmer emission lines for stellar absorption as per the method of Hopkins et al. (2013):

$$S_{\rm cor} = \left(\frac{\rm EW + 2.5\AA}{\rm EW}\right) S_{\rm obs}\,, \tag{2.5}$$

where $S_{\rm cor}$ is the corrected flux measurement, $S_{\rm obs}$ is the observed flux measurement, and EW is the measured equivalent width of the emission line.
This fixed 2.5Å equivalent width correction is found to be appropriate after comparison of the Gaussian fits to the emission lines in GAMA data with the GANDALF v1.5 (Sarzi et al., 2006) fits of the spectra which intrinsically account for stellar absorption. A full description of this comparison is given in Section 6.4 and, in particular, shown in Figure 13 of Hopkins et al. (2013). Furthermore, to test if this might bias our AGN selection, we compare differences in the position on a Baldwin-Philips-Terlevich (BPT, Baldwin et al., 1981) diagram for our measurements versus those from the MPA/JHU SDSS emission line catalogue (Tremonti et al., 2004). For galaxies that lie in the AGN region of the BPT diagram, the median difference in the ratios $\log_{10}$([N II]/Hα) and $\log_{10}$([O III]/Hβ) between our corrected and the MPA/JHU SDSS catalogues are -0.01 and -0.02, with scatter 0.02 and 0.06, respectively. The scatter in these differences is comparable to the median of the standard errors on the distributions of those ratios (0.02 and 0.05 for $\log_{10}$([N II]/Hα) and $\log_{10}$([O III]/Hβ), respectively). Thus, we conclude that no substantial bias in our T2 selection is induced by using the fixed 2.5Å correction for stellar absorption.

We measure the ratios of the [N II] λ6583 to Hα flux and [O III] λ5007 to Hβ flux in order plot a BPT diagram (see Figure 2.4). The ionising radiation emitted by an AGN is harder than that produced by star-formation and, therefore, the two ionising sources excite line species at different rates. These differences manifest themselves in the BPT diagram (Figure 2.4), which reveals that star-forming galaxies and AGN lie in relatively distinct regions. Kewley

et al. (2001) defined AGN on this diagram as having:

$$\log\left(\frac{[\mathrm{O\,III}]\ \lambda5007}{\mathrm{H}\beta}\right) > \frac{0.61}{\log\left(\frac{[\mathrm{N\,II}]\ \lambda6583}{\mathrm{H}\alpha}\right) - 0.47} + 1.19 \tag{2.6}$$

where Hβ, [O III] λ5007, Hα and [N II] λ6583 refer to the flux measurements of those emission lines.

The Kewley et al. (2001) criterion is a conservative segregator of nuclear from star-forming activity. Ergo, some of the galaxies that are close, but fail to satisfy this criterion may be star forming galaxies that also host an AGN. This criterion also selects galaxies with low ionisation nuclear emission regions (LINERs) which are often defined (Kauffmann et al., 2003) as having:

$$\frac{[\mathrm{O\,III}]\ \lambda5007}{\mathrm{H}\beta} < 3 \tag{2.7}$$

Where Hβ and [O III] λ5007 refer to the flux of the hydrogen beta and [O III] λ5007 emission lines respectively. Although sometimes considered to be a subclass of weak AGN, there is some controversy over the nature of LINERs. Recent evidence suggests that black hole accretion may not sufficiently explain these objects, with photoionisation by an ageing stellar population being invoked as a possible explanation (Cid Fernandes et al., 2011). Further to this, spatially resolved integral field unit spectroscopy observes LINER emission to be extended across kpc scales within a galaxy and not just confined to the nucleus (Singh et al., 2013; Belfiore et al., 2016). This further suggests a non-nuclear origin for the ionisation within these galaxies. As such we exclude these galaxies from our sample of AGN, that is our sample of T2 AGN must satisfy equation 2.6 but not equation 2.7.

Obtaining stellar mass estimates for AGN is non-trivial. The GAMA stellar mass catalogue (Taylor et al., 2011) provides stellar masses for every galaxy within the survey as obtained through modelled photometry (Taylor et al., 2011, for a full description see). However, for some AGN, particularly QSOs and T1 AGN, the power-law contribution to the continuum may dominate over the stellar component (note the increase in continuum flux at the blue end of the T1 spectrum in the top panel in Figure 2.3), making the stellar mass measurements unreliable. The [O III] λ5007 emission line is expected to occur due to nuclear ionisation of

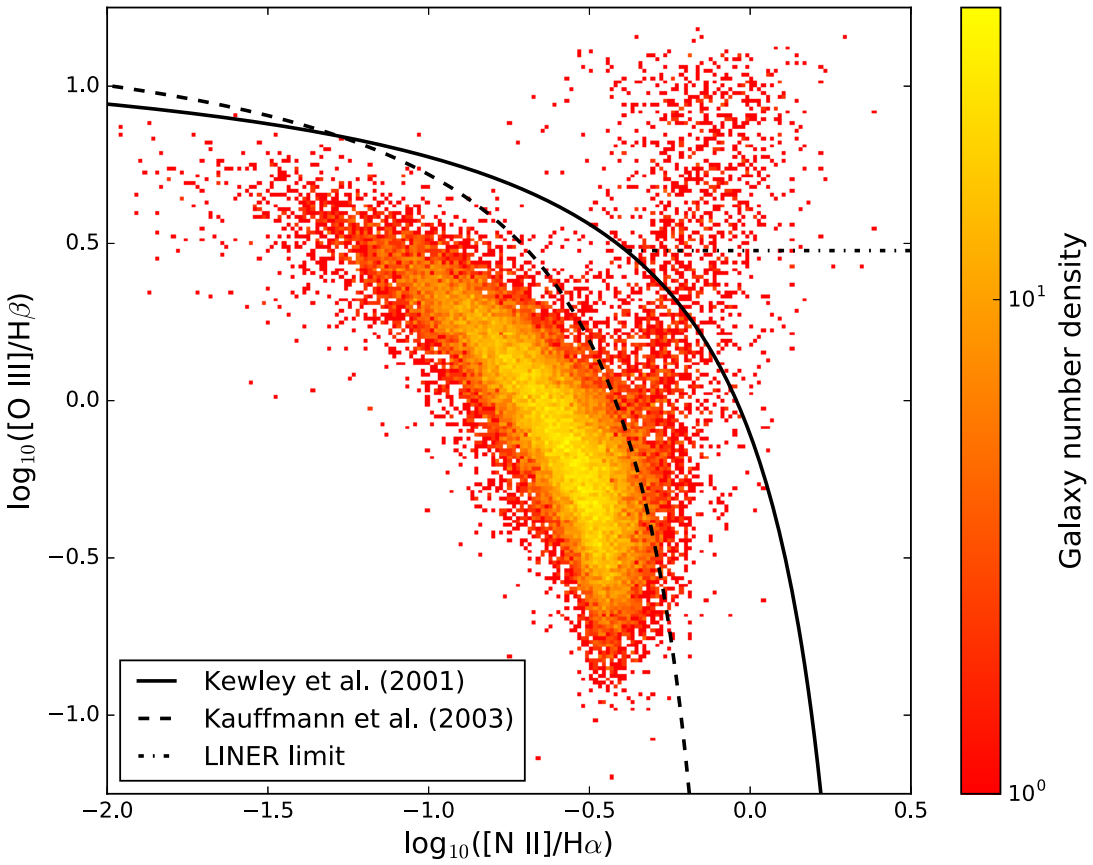

Figure 2.4: 2-dimensional histogram BPT plot of our galaxy sample. The black dot-dashed line is [O III] λ5007/Hβ = 3 to identify LINERs, the black solid curve is the Kewley et al. (2001) line to separate AGN from star forming galaxies and the black dashed line is the Kauffmann et al. (2003) line to segregate star-forming galaxies from AGN. The subtle difference between the objective of the Kewley et al. (2001) and Kauffmann et al. (2003) lines leaves a region between these two curves where the line ratios can be explained by a combination of star-forming and nuclear activity. For our data we classify galaxies above both the Kewley et al. (2001) and [O III] λ5007/Hβ = 3 lines as T2 AGN.

the narrow line region and acts as a proxy for AGN power (Heckman et al., 2005; Pimbblet et al., 2013). Thus for our analysis we decide to match our AGN on [O III] λ5007 luminosity rather than stellar mass when comparing between AGN types. Furthermore, we note that it is very difficult to correct [O III] λ5007 for extinction due to contamination of the observed Balmer decrement by the broad line region (Kauffmann et al., 2003). This issue is further compounded by the differing spatial scales likely to be associated with the broad Balmer and [O III] λ5007 emission regions in the galaxy, hindering the accuracy of any dust correction calculations based on the Balmer decrement from the broad line region. Consequently we compare AGN of different types by their observed [O III] λ5007 luminosity.

For our work we choose to group our AGN into three [O III] λ5007 luminosity bins: low ($\log_{10}L_{[\mathrm{O\,III}]} \leq 41.5$), mid ($41.5 < \log_{10}L_{[\mathrm{O\,III}]} \leq 42$), and high ($\log_{10}L_{[\mathrm{O\,III}]} > 42\,\mathrm{erg\ s^{-1}}$). These bins were to chosen to approximately split the populations into equal subsets while maintaining numbers in each separation bin when AGN in galaxy pairs are considered (see Chapter 2.5.1). The observed [O III] λ5007 luminosity distributions of the T1, extended T1 and T2 AGN samples are shown in Figure 2.5. We note the higher [O III] λ5007 luminosity distribution of our T2s compared to our T1s and extended T1 catalogue. We attribute this to the weaker dependence on the strength of [O III] λ5007 emission line in the selection of these catalogues, and indeed total lack of dependence on this emission line in the case of the bona fide T1 catalogue.

Given the multiple spectra available for some of the galaxies within GAMA we use the spectrum with the most reliable redshift from a particular source. By proxy this subsets only the best quality spectrum for each galaxy as detected by a particular survey. That is to say if a particular galaxy had, for example, 5 spectra obtained within the catalogue, say 2 from GAMA, 2 from SDSS and 1 from 2dFGRS, we would be left with 3 spectra for this galaxy. The 2dFGRS spectrum and the best quality SDSS and GAMA spectra. Furthermore, we only use spectra from either SDSS or GAMA as within our catalogue only these are flux calibrated and hence only these will provide reliable measurements for the [O III] λ5007 luminosity. We select our T1 catalogue first then remove the GAMA catalogue ID (CATAID) of that galaxy from consideration for the other two catalogues. That is to say if a spectrum is selected as a

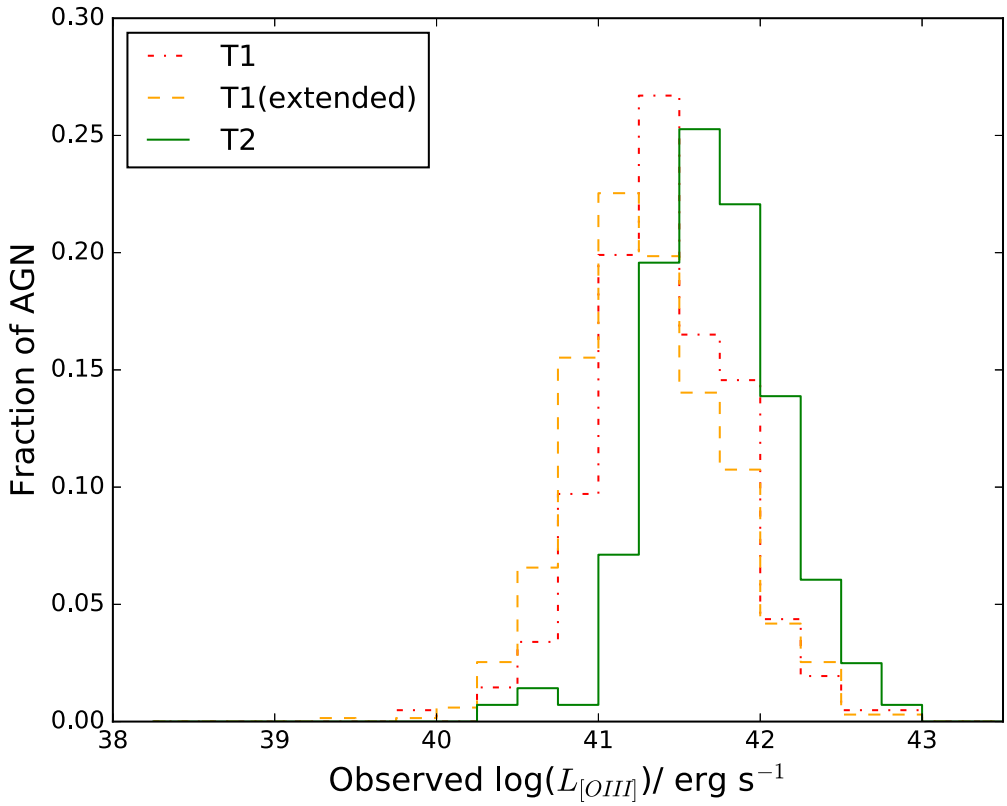

Figure 2.5: The distribution of observed (not extinction corrected) [O III] λ5007 luminosities in our sample by AGN type.

bona fide T1, then it cannot be reselected as an intermediate type or T2 AGN whose selection criteria it may also satisfy. We then remove any galaxies selected as intermediate type AGN from consideration as T2 AGN. To ensure each galaxy is only counted once in each catalogue, any duplicate CATAIDs (e.g. a GAMA and an SDSS spectrum for a particular galaxy) are removed from the catalogues.

This method is chosen over the more simple method of only selecting the spectrum with the most reliable redshift overall (regardless of survey) before applying our AGN selection criteria. We take this approach in order to ensure that some borderline AGN are not selected against due to a line of consequence being less well observed in the most reliably redshifted spectrum. When these two approaches are compared only 7 AGN are not selected by the simpler method that are selected by our method.

In total we find 954 AGN of all types across 4 catalogues: bona fide T1s; $1 < T < 2$; an extended catalogue which includes any AGN with a broad Hα component, i.e. the $1 < T < 2$ catalogue appended to the bona fide T1 catalogue; T2. As a result of our selection of only AGN with high S/N on all emission lines required for classification, these numbers are lower than might be expected. Indeed, Miller et al. (2003) have shown that using such unambiguous detections of all required emission lines may exclude up to half of the the AGN population that do not satisfy such strict selection criteria, consequently our AGN selection is conservative. The numbers of galaxies in each of our AGN catalogues is shown in Table 2.2. All of the AGN are selected from the three 60 square degree GAMA equatorial fields (G09, G12, G15). We note that our AGN types have similar redshift distributions, inseparable by use of a Kolmogorov-Smirnov (KS) test, enabling a fair comparison of the environment of these catalogues. The redshift distributions of our AGN are shown in Figure 2.6.

We further to this find 111 LINERs which satisfy the Kewley et al. (2001) criteria but have an [O III] λ5007/Hβ flux ratio of less than 3. Our sample contains fewer LINERs than might be expected given that this class of galaxy may account for as much as one third of the local galaxy population (Heckman, 1980). We attribute this to two factors. Firstly, as these are weak emission line galaxies they are intrinsically harder to detect when a good signal to noise cut is applied. Indeed, in our sample of LINERs the median Hβ equivalent width is less

Table 2.2: The final number of selected AGN of each type in our sample. Also included is the number LINERs detected in our data selection.

AGN catalogue	No. of galaxies
T1 (bona fide)	209
1 < T < 2 (intermediate type)	464
T1 (extended; bona fide + intermediate catalogues)	673
T2	281
LINER	111

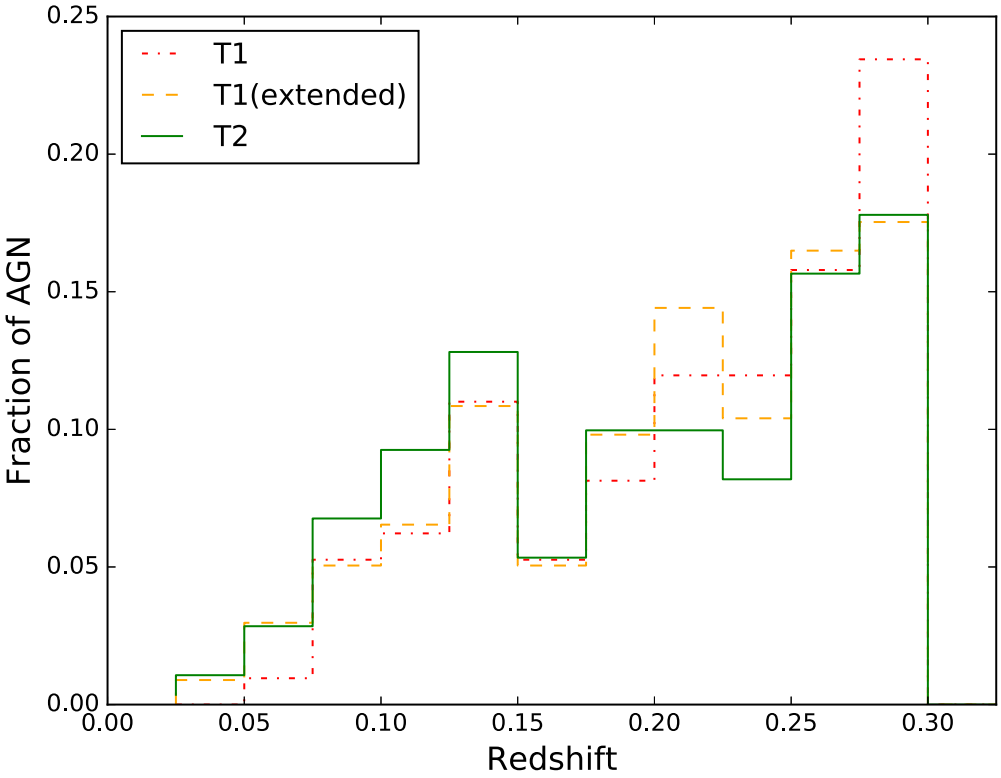

Figure 2.6: The redshift distribution of the AGN in our sample by AGN type.

than 3Å and thus only the highest quality spectra will detect these using our selection criteria. Secondly, the 2.5Å Balmer absorption correction used is a general correction (Hopkins et al., 2013) and not optimal for the older stellar population associated with LINERs (Cid Fernandes et al., 2011).

2.4.2 Selection of galaxy pairs

In order to directly compare our results to those of Villarroel & Korn (2014), we find all the GAMA galaxies within a projected separation $\mathrm{d}R \leq 350\,\mathrm{kpc}\,h^{-1}$ and redshift difference $|\Delta z| \leq 0.012$ of an AGN. This creates our pair catalogue, note that each AGN may be in a single pair, multiple pairs or not in a pair at all. The large limit placed on the redshift separation of our pairs prevents us from reliably selecting pairs from the GAMA group catalogue $\mathrm{G^3Cv08}$ (Robotham et al., 2011).

These criteria result in a catalogue of 766 galaxies neighbouring 329 of our T1s (extended catalogue). Of these, 195 galaxies are neighbours to 81 of our bona fide T1s. For our T2 population we find that there are 273 neighbouring galaxies to 132 T2 AGN. The velocity separation used here is rather large. However, velocity difference is less significant than projected separation in finding true galaxy pairs (Nazaryan et al., 2013). This is shown in our sample, of which 79% of the neighbours of the bona fide T1s, and 82% of the neighbours of both the extended catalogue T1s and the T2s have $|\mathrm{d}V| \leq 1000\,\mathrm{km\ s^{-1}}$. When we take a subset of those neighbouring galaxies in 'close pairs', i.e. within the GAMA group catalogue $\mathrm{G^3Cv08}$ pair criteria (Robotham et al., 2011, 2014) of $\mathrm{d}R \leq 100\,\mathrm{kpc}\,h^{-1}$ and $|\mathrm{d}V| \leq 1000\,\mathrm{km\ s^{-1}}$ we find that there are 28 neighbours to 22 of our bona fide T1s, 152 neighbours to 120 of the extended catalogue T1s and 59 neighbouring galaxies to 50 T2s.

2.5 Analysis and Discussion

2.5.1 Type 1 and type 2 AGN fractions in galaxy pairs

Given the previous results calling in to question AGN unification (Dultzin-Hacyan et al., 1999; Krongold et al., 2002; Koulouridis et al., 2006; González et al., 2008; Villarroel & Korn, 2014; Jiang et al., 2016), our ambition is to test these results as thoroughly as possible

using the high spectroscopic completeness of GAMA. The pair fraction has been used heavily as a proxy for identifying the impact of environment due to galaxy-galaxy interactions in, e.g., triggering star-formation, AGN and for measuring the galaxy merger rate (Owers et al., 2007; Ellison et al., 2011; Patton et al., 2013; Robotham et al., 2014). This is the measure that frequently shows evidence of a difference between T1 and T2 AGN when such a result is found. Therefore, we compare the fraction of AGN with a neighbour within both the larger and tighter pair selection (see Figures 2.7 and 2.8).

We find no significant difference in the fraction of T1 and T2 AGN found in a pair using our own pair criteria regardless of which T1 selection is used. This observation stands when only AGN in the same [O III] λ5007 luminosity bin are compared. Furthermore, in contrast with the results of Dultzin-Hacyan et al. (1999); Koulouridis et al. (2006) and Jiang et al. (2016), we find no significant difference in the fraction of T1 and T2 AGN found in pairs with $\mathrm{d}R < 100\,\mathrm{kpc}\,h^{-1}$ and $|\mathrm{d}V| < 1000\,\mathrm{km\,s^{-1}}$. Again, this result does not change when only AGN with similar [O III] λ5007 luminosity are compared. However, we do note that for both pair criteria there is suggestive, though still insignificant, evidence that the bona fide T1s may be marginally less likely to be found in a galaxy pair than AGN from either of the other two catalogues. With more data to reduce the statistical uncertainties, this may indeed support prior observations of more T2s with a close neighbour than T1s. The errors on this and the other fractional measurements throughout this chapter are binomial assuming a beta distribution (Cameron, 2011).

Pair separations of $\mathrm{d}R < 100\,\mathrm{kpc}\,h^{-1}$ and $|\mathrm{d}V| < 1000\,\mathrm{km\,s^{-1}}$ or similar are commonly used in literature (e.g., Ellison et al., 2008; Robotham et al., 2014, the former using $\mathrm{d}R < 80\,\mathrm{kpc}\,h^{-1}$ and $|\mathrm{d}V| < 500\,\mathrm{km\,s^{-1}}$) as this includes the scale of the Milky Way - Magellanic cloud system, and indeed these galaxies have most likely recently interacted or are currently interacting. In order to assess the fraction of AGN that are that are most likely to have undergone a recent interaction, or are currently interacting, would require an investigation of pairs separated by $\mathrm{d}R < 20\,\mathrm{kpc}\,h^{-1}$ and $|\mathrm{d}V| < 500\,\mathrm{km\,s^{-1}}$ (Robotham et al., 2014). Given the relatively small size of our sample we are limited on this front, however we observe that $2.39^{+0.74}_{-0.46}$% and $5.69^{+1.72}_{-1.09}$% of our extended catalogue T1s and T2s respectively are in these

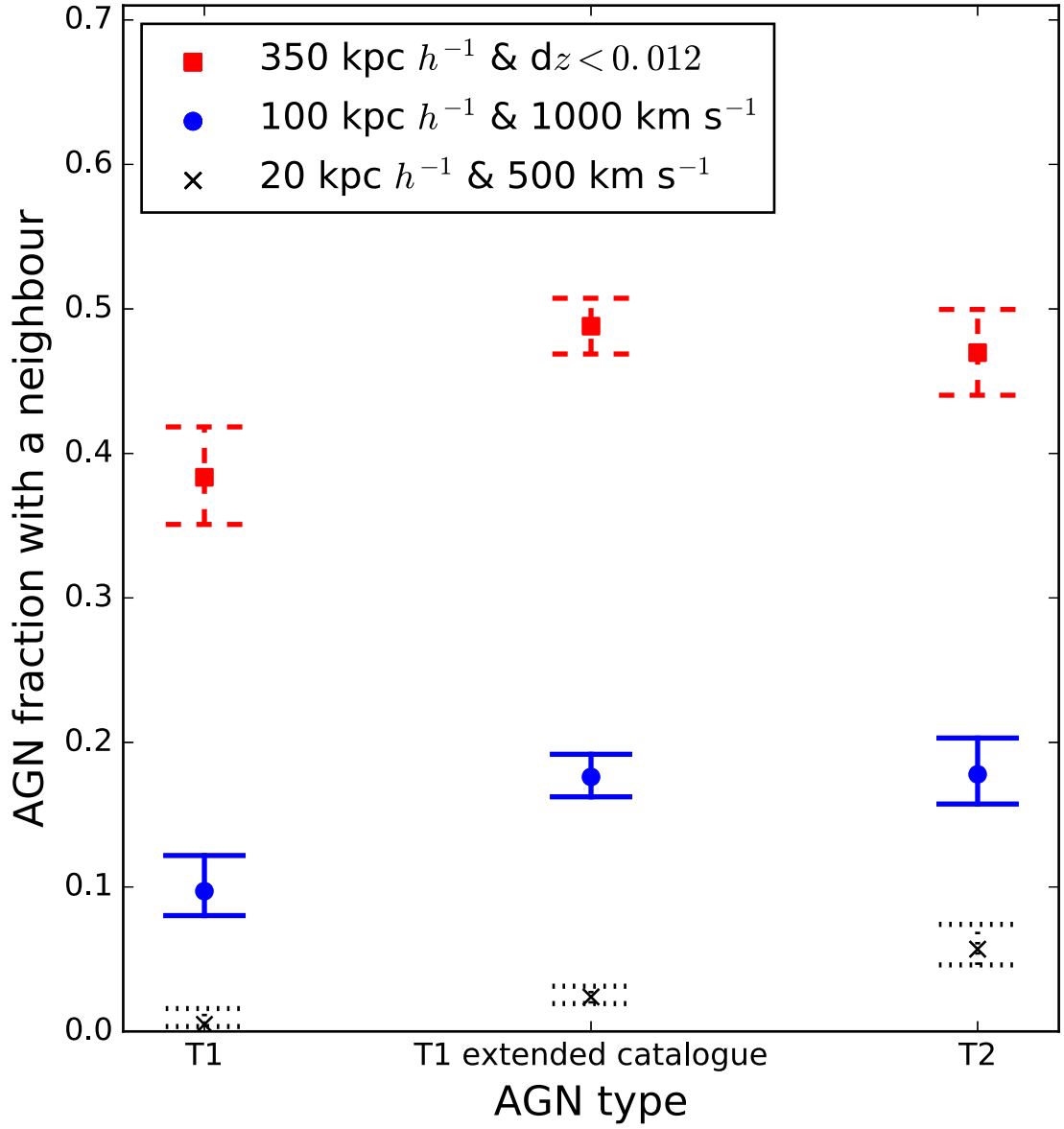

Figure 2.7: The likelihood of AGN of each type to be in a pair or a close pair. The red squares use our own criteria of dR < 350 kpc h^{-1} and Δz < 0.012. The blue circles use the GAMA definition of a pair (Robotham et al., 2014) of dR < 100 kpc h^{-1} and dR < 1000 km s^{-1}. The black crosses use only pairs which are likely to be directly interacting (Robotham et al., 2014), i.e., those with dR < 20 kpc h^{-1} and dR < 500 km s^{-1}. We note that for the closest pair criterion (the black crosses) only 1 pair is found with a T1 and 16 pairs with T1(extended catalogue) and T2 AGN. This plot includes AGN of all [O III] λ5007 luminosities and the error bars are binomial.

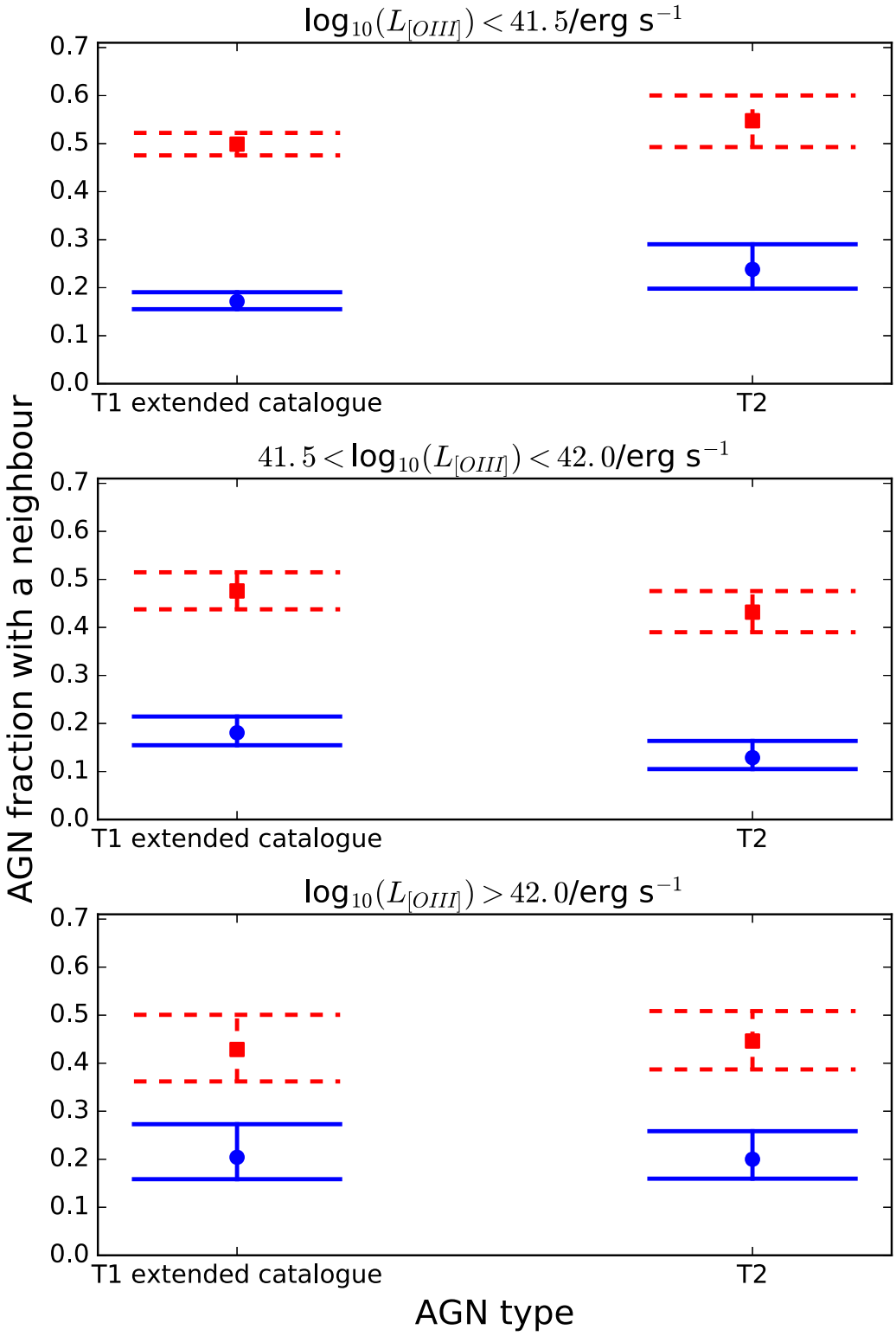

Figure 2.8: The likelihood of AGN of each type to be in a pair or a close pair by luminosity bin. The legend is the same as in figure 2.7 and due to low numbers the only the extended catalogue T1s compared to the T2s and pairs with dR < 20 kpc h^{-1} and dR < 500 km s^{-1} are not included.

very tight pairs and are hence likely to be undergoing a merger. Casteels et al. (2014) found that less than 2% of galaxies with $8.5 < \log(M_\star/M_\odot) < 11$ are undergoing a merger at any one time, thus our observations suggest that there may be an excess of T2s undergoing mergers.

We also calculate the pair fraction of our AGN as a function of pair separation. We separate our pairs into 50 kpc h^{-1} bins and calculate the pair fraction in each bin. We define the pair fraction, f, as:

$$f = \frac{N_{\rm pair}}{N_{\rm total}} \tag{2.8}$$

Where $N_{\rm pair}$ is the number of AGN of that type and [O III] λ5007 luminosity bin in a pair of the appropriate separation and $N_{\rm total}$ is the total number of AGN of that type and [O III] λ5007 luminosity bin. We compare the pair fractions of both the bona fide and extended T1 AGN catalogues with the T2 catalogue (see Figure 2.9) and find no difference in the pair fractions with AGN type. We repeat this using only the nearest neighbour to each AGN such that each AGN is only used in one pair, the closest possible. Here we find no difference between either of our T1 populations and the T2s. As using either the T1 extended catalogue or the bona fide catalogue makes no difference to our results, we show the extended catalogue comparison with the T2s in Figure 2.9 to make use of higher AGN numbers and reduce the uncertainties.

2.5.2 Neighbouring galaxies of AGN

In order to test the colour differences of neighbouring galaxies to AGN found by Villarroel & Korn (2014), we look at the properties of the neighbouring galaxies within our pairs. We use only those pairs where the neighbouring galaxy is not within any of our AGN or LINER catalogues, that is to say we exclude AGN-AGN and AGN-LINER pairs. We find that the vast majority of our AGN pairs are retained, with only 3, 9 and 4 AGN-AGN or AGN-LINER pairs respectively in our bona fide T1, extended T1 (including the bona fide T1s) and T2 AGN pair catalogues. With such low numbers, we are unable to investigate whether or not there are any trends in AGN-AGN pairs and restrict ourselves to AGN-non AGN pairs.

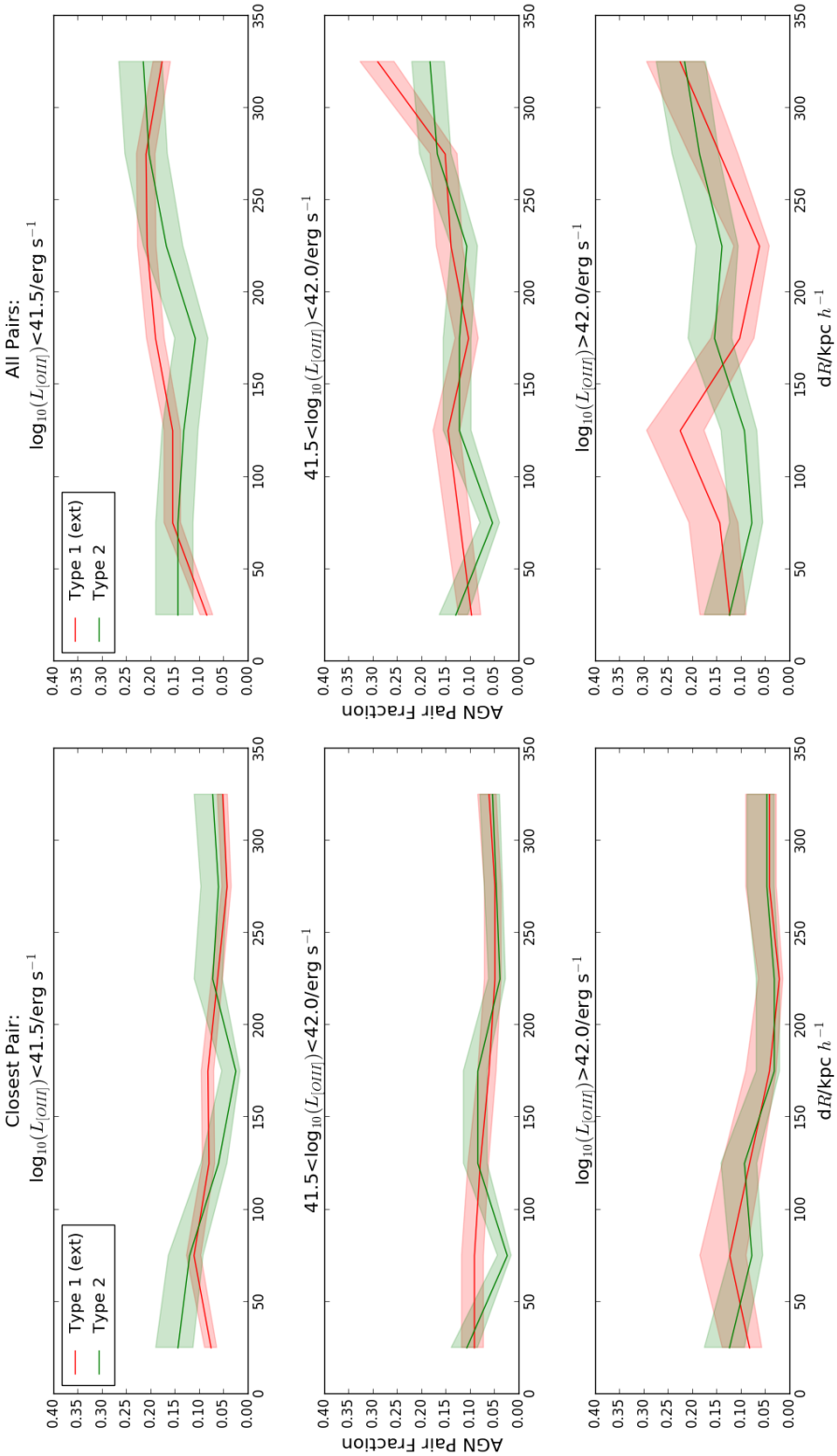

Figure 2.9: The fraction of our AGN sample found in pairs of galaxies by projected separation. Red lines represent the T1 (extended catalogue) AGN and green lines the T2s. The shaded regions are the one sigma binomial error limits. Left column: T1 (extended catalogue) and T2 AGN pair fractions by pair separation for only the closest pair (in projection) for each AGN, low to high $L_{[\mathrm{O\ III}]}$ AGN from top to bottom. Right Column: T1 (extended) catalogue and T2 pair fractions for all pairs satisfying our pair criteria, low to high $L_{[\mathrm{O\ III}]}$ from top to bottom.

Table 2.3: Results of the 2 sample KS tests applied to the $u-r$, SFR and sSFR distributions of neighbouring galaxies of the extended T1 and T2 AGN. The p-values for all the AGN in pairs and those that a matched to others with $41.5 < \log_{10}(L_{[\mathrm{O\,III}]}) \leq 42.0$ are shown.

Neighbour property	p(all $L_{[\mathrm{O\,III}]}$)	$p(41.5 < \log_{10}(L_{[\mathrm{O\,III}]}) \leq 42.0)$
$u-r$	0.117	0.569
$g-i$	0.110	0.736
SFR	0.676	0.675
sSFR	0.833	0.815

Colours and stellar masses

We compare the $u-r$ colours of the neighbouring inactive (in a nuclear sense) galaxies of T1, extended T1 and T2 AGN in pairs. The $u-r$ colours are taken from the GAMA stellar mass catalogue (StellarMassesv18, Taylor et al., 2011) and are taken from the modelled AB rest-frame SDSS u and r bands. These magnitudes are extinction and k-corrected. The distributions of the $u-r$ when the neighbours of AGN of all [O III] λ5007 luminosities are considered appear to similar between AGN type (see Figure 2.10). To statistically assess this apparent similarity we perform a KS test on the colour distributions of the neighbours of T2 and extended catalogue T1s to maximise the numbers of galaxies used in this analysis. We find that the probability that the colour distribution of the neighbouring galaxies of T1-extended and T2 AGN are drawn from the same parent population to be greater than 11%, with a p-value of 0.117. That is to say we cannot confidently say the distributions are drawn from different parent populations. This result doesn't change if the subset of neighbours of bona fide T1s are used instead of the neighbours of the whole extended T1 catalogue. When only AGN in our middle (and largest for numbers of AGN) [O III] λ5007 luminosity bin ($41.5 < \log_{10}(L_{[\mathrm{O\,III}]}) \leq 42.0$) are used, the KS derived p-value increases to 0.569, again indicating that the neighbouring galaxies of the AGN are likely to be drawn from the same parent sample. We apply this same test to the rest-frame, extinction-corrected $g-i$ colours of the neighbouring galaxies of AGN we find similar results. The results of the KS tests performed on the colour distributions are shown in Table 2.3.

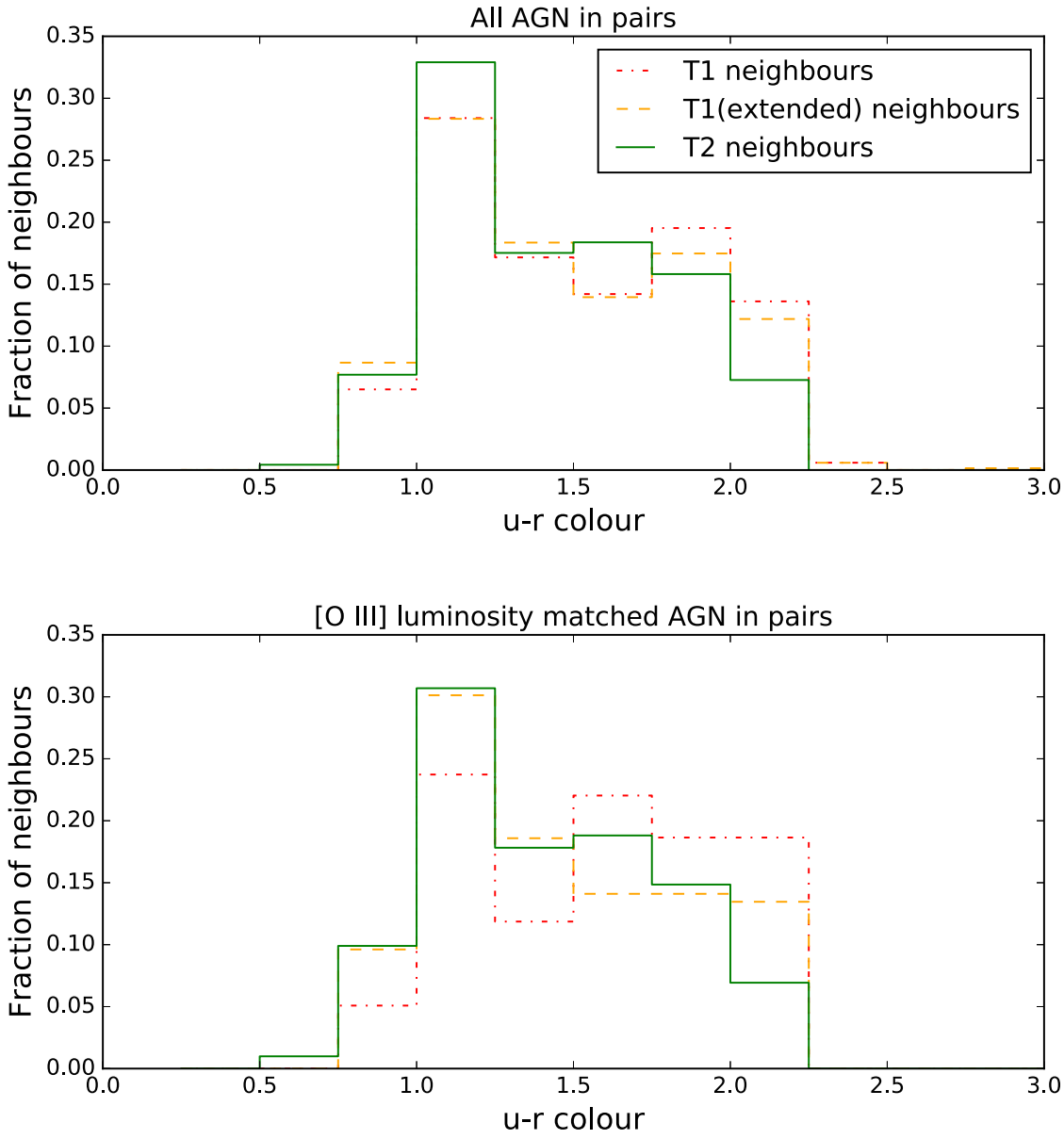

Figure 2.10: Histograms showing the $u - r$ colour distributions of non-AGN neighbouring galaxies of AGN in pairs. Upper panel: all our AGN in pairs, lower panel: only AGN with $41.5 < \log_{10}(L_{[\mathrm{O\,III}]}) \leq 42.0$ in pairs.

We also compare the stellar masses of the neighbouring galaxies. The distributions are shown in Figure 2.11. These distributions are not separated by KS testing, giving a p-value of 0.324 when the extended T1 AGN neighbour masses are compared the T2 neighbour masses for all AGN [O III] λ5007 luminosities.

Star formation

Given the availability of spectra for all galaxies in our pairs, we compare the star-formation rates (hereafter SFR) of the neighbours where possible. This data is taken from the GAMA II emission line physical properties catalogue (to be produced as EmLinesPhysv05, Hopkins et al., 2013), where the star formation rate (in $M_\odot$ yr^{-1}) assumes a Chabrier (2003) IMF and is found using:

$$\mathrm{SFR} = \frac{L_{\mathrm{H}\alpha,\mathrm{int}}}{2.16 \times 10^{34}} \tag{2.9}$$

Where good mass data is available for the neighbouring galaxies this is taken from the GAMA stellar mass catalogue (Taylor et al., 2011) and this is used to calculate the specific star formation rates (hereafter sSFR) where possible. The distributions of the SFRs and sSFRs are shown in Figures 2.12 and 2.13 respectively. There is no apparent trend in SFR or sSFR of the neighbouring galaxy with AGN type and this is confirmed by performing KS tests on these distributions. The results of the KS tests for SFR and sSFR distributions are also shown in Table 2.3. When only AGN of similar [O III] λ5007 luminosity are used we still see no difference in either SFR or sSFR of the neighbouring galaxies.

We use the BPT criteria to classify the neighbours of the AGN, which are not themselves AGN or LINERs, as star-forming galaxies. We classify those neighbouring galaxies with all four emission lines with S/N > 3 and that satisfy the Kauffmann et al. (2003) criteria as star forming galaxies. We then compare the fraction of neighbouring galaxies classed as star formers by AGN type and find no difference in this fraction. This lack of difference in star-forming neighbour fraction is consistent regardless of [O III] λ5007 luminosity bin matching. The fraction of star-forming neighbours by AGN type is shown in Figure 2.14. These observations suggest that if the presence of an AGN is more likely in environments conducive to triggering star formation, then this does not differ with AGN type.

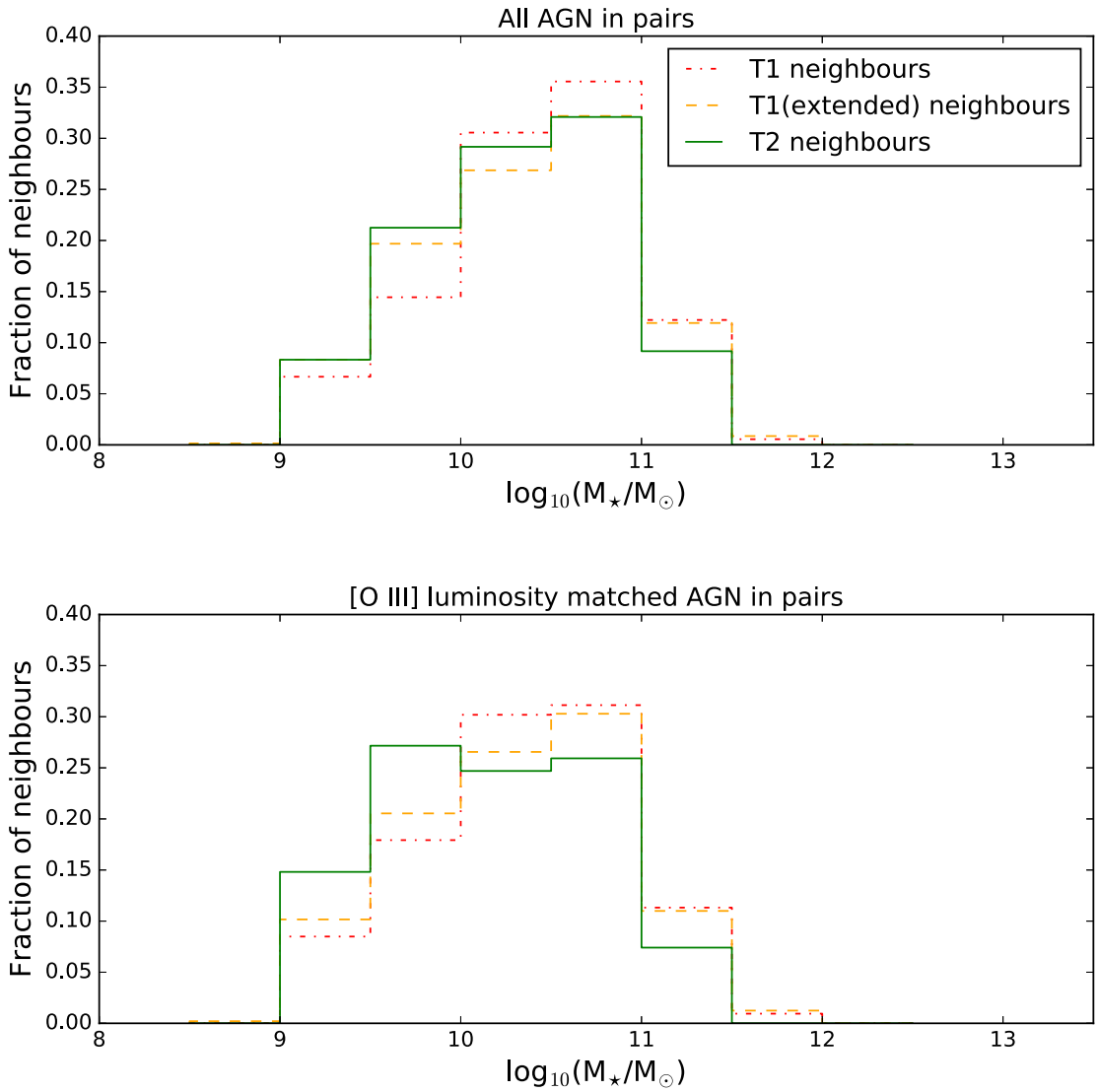

Figure 2.11: Histograms showing the stellar mass distributions of the neighbouring galaxies to the AGN in pairs by AGN type. Upper panel: all our AGN in pairs, lower panel: only AGN with $41.5 < \log_{10}(L_{[\mathrm{O\,III}]}) \leq 42.0$ in pairs.

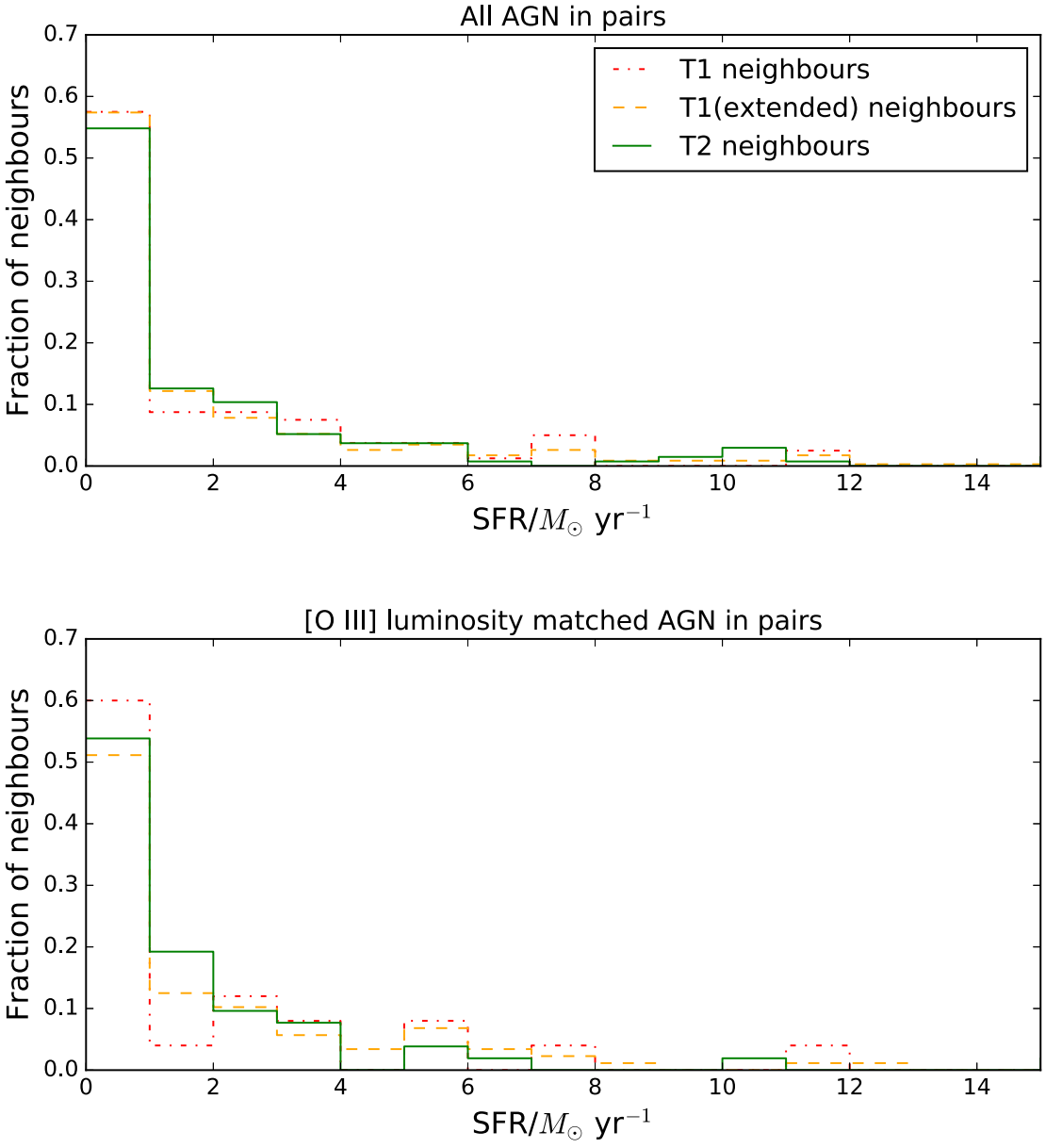

Figure 2.12: Distribution of star formation rates for neighbouring galaxies of AGN in pairs that are not themselves AGN hosts and for which reliable emission line data is available. Upper panel: all our AGN in pairs, lower panel: only AGN with $41.5 < \log_{10}(L_{[\mathrm{O\,III}]}) \leq 42.0$ in pairs.

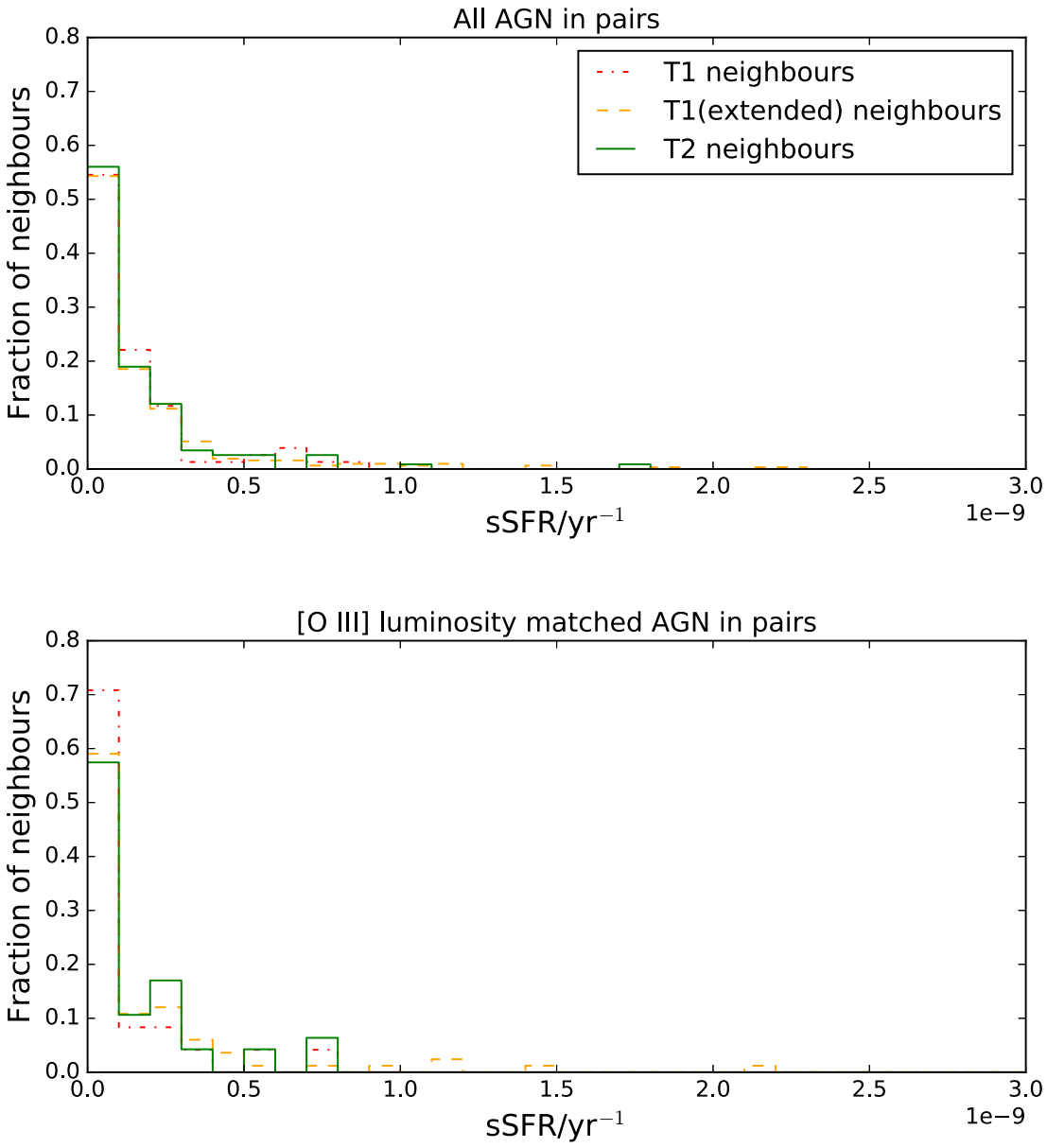

Figure 2.13: Distribution of specific star formation rates for neighbouring galaxies of AGN in pairs which are not themselves AGN hosts and for which reliable emission line data is available. Upper panel: all our AGN in pairs, lower panel: only AGN with $41.5 < \log_{10}(L_{[\mathrm{O\,III}]}) \leq 42.0$ in pairs.

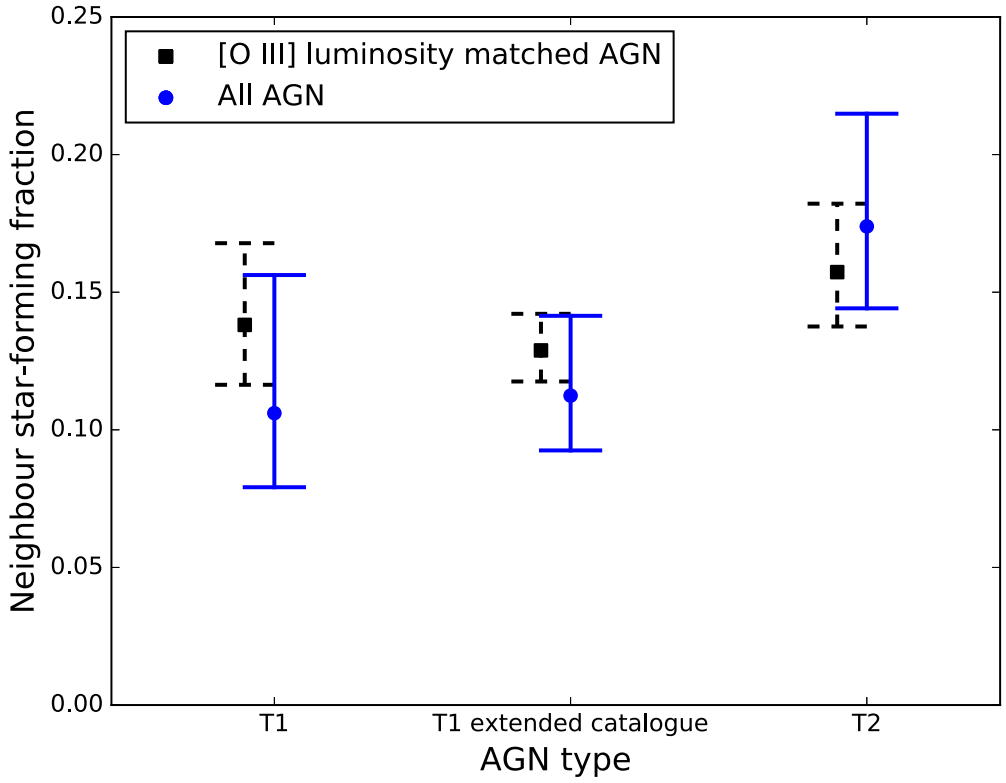

Figure 2.14: Fraction of neighbouring galaxies of AGN that are classified as star forming by Kauffmann et al. (2003). The blue circles with solid error bars represent all our AGN in pairs. The black squares with dashed error bars are representing AGN with $41.5 < \log_{10}(L_{[\mathrm{O\,III}]}) \leq 42.0$ in pairs. The error bars are binomial and the two populations are horizontally offset from each other for clarity.

Fifth nearest neighbour

Finally, we use the version 5 of GAMA environmental measures catalogue (EnvironmentMeasuresv05, Brough et al., 2013) to assess the environmental density of our AGN by type using the measurement to the fifth nearest neighbour (Σ_5). The environmental measures catalogue only uses galaxies with an absolute magnitude in the r band of $r_{\mathrm{abs}} < -20$ and is limited to a redshift of $z < 0.18$. This reduces the sample of AGN we can measure this for to 59, 219 and 112 for out T1 bona fide, T1 extended and T2 AGN catalogues respectively, of which 31, 147 and 77 have neighbouring galaxies. Upon using only AGN from our middle [O III] λ5007 luminosity bin these numbers drop to 18 (6 with a neighbour) T1bona fide catalogue, 45 (27) T1 extended catalogue and 49 (33) T2.

Table 2.4: Results of the 2 sample KS tests applied to the $u-r$, $g-i$, SFR and sSFR distributions of neighbouring galaxies of the extended T1 and T2 AGN with $z < 0.18$ to enable comparison with the GAMA environmental measures catalogue. Also included are the KS test results of the Σ_5 measure for the AGN. The p-values for all the AGN in pairs and those that a matched to others with $41.5 < \log_{10}(L_{[\mathrm{O\,III}]}) \leq 42.0$ are shown.

Neighbour property	p(all $L_{[\mathrm{O\,III}]}$)	$p(41.5 < \log_{10}(L_{[\mathrm{O\,III}]}) \leq 42.0)$
$u-r$	0.0248	0.199
$g-i$	0.0119	0.108
SFR	0.600	0.914
sSFR	0.437	0.758
Σ_5	0.126	0.508

Given the low numbers of bona fide T1s at $z < 0.18$, we only compare AGN from the extended T1 catalogue with the T2s. The median Σ_5 values of the extended T1 and T2 AGN in the environmental measure catalogue are $1.92^{+1.23}_{-0.87}$ and $1.94^{+0.81}_{-0.89}$ Mpc respectively, where the lower and upper bounds refer to the 25th and 75th percentiles. When we apply a KS test the Σ_5 distributions we find no difference between the extended T1 and T2 populations (see Table 2.4). In order to compare the colours and (s)SFRs with the Σ_5 we redo these tests for only AGN with $z < 0.18$. Here we again find that there is no significant difference in either the $u-r$, $g-i$, SFRs or sSFRs of the neighbouring galaxies of different AGN types.. A similar result is found when only AGN from our middle [O III] λ5007 luminosity bin are compared. The full results of these KS tests are given in Table 2.4. Our data suggests the T1 and T2 neighbours are drawn from the same population.

2.5.3 The effect of pair separation on neighbour properties

The use of any neighbouring galaxy within $\mathrm{d}R < 350\,\mathrm{kpc}\,h^{-1}$ and $|\Delta z| \leq 0.012$ is somewhat liberal and is likely to include galaxies that are not truly interacting. To this end we take a subset of only those galaxy pairs that satisfy the more rigid criteria of $\mathrm{d}R < 100\,\mathrm{kpc}\,h^{-1}$ and $|\mathrm{d}V| < 1000\,\mathrm{km\ s^{-1}}$. This is chosen to approximate the scale of the Milky Way - Magellanic clouds interacting system (Robotham et al., 2014), and thus contain only interacting galaxies. Furthermore, we investigate the effect when only the closest neighbour of an AGN is used in

this analysis rather than all neighbours satisfying the pair criteria. We redo all our neighbour property analysis for this close pairs data and find no differences in any of the neighbour properties when the extended T1 AGN are compared with the T2 AGN. The bona fide T1s are not used in comparison with the T2s here due to low numbers. We find no difference between T1 and T2 AGN when either of these pair criteria are used, using any of our neighbour property tests.

Of particular interest is the analysis when only pairs with $\mathrm{d}R < 100\,\mathrm{kpc}\ h^{-1}$ and $|\mathrm{d}V| < 1000\,\mathrm{km\ s^{-1}}$ are considered. Figure 6 in Robotham et al. (2014) shows that the fraction of galaxies that show signs of interaction in their morphologies increase as projected separation and, to a lesser extent, velocity difference decrease. Those galaxies that have $\mathrm{d}R < 20\,\mathrm{kpc}\ h^{-1}$ and $|\mathrm{d}V| < 500\,\mathrm{km\ s^{-1}}$ are especially likely to show morphological disturbance. We show in Chapter 2.5.1 that there may be an excess of T2s in pairs this close relative to the extended T1s and indeed the general galaxy population (Casteels et al., 2014). We only have one bona fide T1 in a pair this close and as such do not compare the fraction of bona fide T1s to our other AGN populations here. Krongold et al. (2002) and Koulouridis et al. (2006) have previously suggested a model whereby galaxy interactions trigger star-formation before narrow line nuclear activity is produced during the interaction, with broad line nuclear activity occurring later, post interaction. Further still, the observations of Satyapal et al. (2014) show that closer projected separation is linked to an increase in obscured AGN fraction, while Kocevski et al. (2015) and Fan et al. (2016) show an increased merger fraction in obscured AGN.

If AGN are preferentially obscured by close interactions and mergers (see in particular Section 5.2 of Cattaneo et al., 2005 and Figure 10 of Kocevski et al., 2015), then this could potentially be the result of a couple of different mechanisms. First, it may be the case that the either the gravitational effects of close interactions disturb the galaxy so as to disturb the morphology of the dust content of the torus and hence increase the chance of obscuration of an active nucleus. Second, the increased accretion onto the black hole could draw more dust toward the central engine and hence increase both the covering factor and opacity of the obscurer. If our observations hold up with a larger observed population they may provide

supporting evidence for such models.

2.6 Comparisons with Contrasting Observations

2.6.1 The potential dependence of small-scale clustering of Type 2 AGN on [O III] λ5007 luminosity

Our observations are consistent with the the assumption that, being physically the same, T1 and T2 AGN reside in similar environments. We observe a potential excess of Type 2 AGN relative to the general galaxy population in pairs separated by $\lesssim 20$ kpc. Our observations of the Type 1 AGN population in these close pairs is perfectly consistent with the general galaxy population based on the work of Casteels et al. (2014) and Robotham et al. (2014). These observations are viable within AGN unification should mechanisms such as close gravitational interactions increasing the torus covering factor, and hence the likelihood of nuclear obscuration, be invoked.

Like ourselves Dultzin-Hacyan et al. (1999), Koulouridis et al. (2006), and Jiang et al. (2016) detect a relative excess in the number of neighbours of Type 2 AGN at the sub 100 kpc scale. Additionally, and supporting our observations, Jiang et al. (2016) note that this excess is greatest at the sub 30 kpc scale and arrive at the same conclusion as ourselves as to the physics responsible for this. Unlike our observed over-clustering of Type 2 AGN however, the observations Dultzin-Hacyan et al. (1999), Koulouridis et al. (2006), Jiang et al. (2016), and Krumpe et al. (2018) have high statistical significance.

A possible explanation for this can be seen by comparing the [O III] 5007 luminosity distributions of Jiang et al. (2016) and this work. The distribution of Type 2s in Jiang et al. (2016) is offset $\sim$ 2 orders of magnitude lower than ours, and their Type 1 $L_{[\mathrm{O\,III}]\,5007}$ is offset approximately half an order of magnitude lower than our sample. This implies that the excess clustering observed may be dependent on the luminosity of the AGN. The upper left hand panel of figure 2.9, which compares the fraction of neighbours of Type 1 and 2 AGN with a neighbour as function of pair separation at $\log_{10}(L_{[\mathrm{O\,III}]\,5007}/\mathrm{erg\,s^{-1}}) < 41.5$, supports this hypothesis with an excess of Type 2 AGN having a neighbour within 50 kpc at $\sim 2\sigma$ confidence. The covering factor of the torus has been shown to decrease with increasing

[O III] 5007 luminosity (Arshakian, 2005). Consequently high [O III] 5007 luminosities could act to counter the increase in nuclear obscuration as the result of close gravitational interactions, and thus offset the increase in clustering at small scales around Type 2 AGN.

2.6.2 The like colours of the neighbours of type 1 and type 2 AGN

The most puzzling aspect of our results is our inability to replicate the observations of Villarroel & Korn (2014) with our data. In particular, we find no difference in the colours of the neighbouring galaxies. As such this inevitably raises questions as to whether or not our comparison with Villarroel & Korn (2014) is a fair one, if ourselves and Villarroel & Korn (2014) are segregating our AGN in a similar manner, or if some other kind of selection effect may be biasing one of our results.

The strongest colour difference in the neighbours of T1 and T2 AGN observed by Villarroel & Korn (2014) occurs when the pair is separated by less than 100 kpc h^{-1}. As our comparison of the colour distributions takes into account pair separations up to 350 kpc h^{-1} it is logical to ask if our results change if we limit the analysis to sub 100 kpc h^{-1} pairs. For this separation we only have 20 neighbours with reliable observed colours to out bona fide T1 AGN. As such, we only compare our extended T1 to our T2s in this test. Given that Villarroel & Korn (2014) select their T1 AGN only on the presence of a broad Hα line, we consider this to be a fair comparison of our observations with those of Villarroel & Korn (2014).

For AGN-galaxy pairs with $\mathrm{d}R < 100$ kpc h^{-1} and $|\mathrm{d}V| < 1000$ km s^{-1} we find mean $u-r$ colours of the neighbours of the extended T1 and T2 AGN to be 1.49 ± 0.04 and 1.49 ± 0.05 mag respectively. If we limit our selected AGN to only those with $41.5\,\mathrm{erg\,s^{-1}} < L_{[\mathrm{O\,III}]} < 42.0\,\mathrm{erg\,s^{-1}}$, the mean neighbour $u-r$ colours are 1.53 ± 0.07 for the extended T1s and 1.56 ± 0.09 for the T2s. The errors are estimated using the standard error of the mean. Given the scale of our errors, compared to the scale of the difference in colour observed by Villarroel & Korn (2014) (≈ 0.3 in their spectroscopic sample, rising to ≈ 0.5 in their photometric sample), then we would expect to see a similar colour difference in our sample should one exist. Furthermore, the KS derived p-values for the colour distributions of the neighbouring galaxies of the extended T1 and the T2 AGN being statistically similar to be 0.989 and 0.910 for all AGN of all [O III] λ5007 luminosities and $41.5\,\mathrm{erg\,s^{-1}} < L_{[\mathrm{O\,III}]} < 42.0\,\mathrm{erg\,s^{-1}}$ respectively.

That is to say, when we observe the pairs where Villarroel & Korn (2014) found the strongest difference in colour between the neighbours of T1 and T2 AGN, we find no such difference.

The incompleteness of the SDSS spectroscopic sample may contribute to the colour differences (Villarroel & Korn, 2014) observe in the neighbours of Type 1 and 2 AGN. The SDSS spectroscopic survey targeting strategy preferentially targets QSOs (Strauss et al., 2002). Given that these are classified as QSOs based on their photometry, these are likely to be unobscured AGN and hence Type 1 AGN (e.g. note the big blue bump present in quasar SEDs as shown in Figure 1.10). That is to say, for densely populated regions of the sky (e.g. the cores of galaxy clusters) Type 1 AGN may be prioritised over Type 2 AGN for spectroscopic observation. A result of this is that the Type 1 population observed by Villarroel & Korn (2014) may be found in a denser large-scale environment on average that their Type 2 sample. Dense environments are known to be hostile to star-formation (e.g., Fraser-McKelvie et al., 2014; Barsanti et al., 2018), and hence galaxies in such environments have redder colours. Therefore, should the Type 1 sample of Villarroel & Korn (2014) be in a denser large scale environment than their Type 2 population as a result of the spectroscopic targeting of SDSS, then this may contribute to the colour difference they observe in the neighbours of these populations.

2.6.3 AGN selection

Villarroel & Korn (2014) select their T1 AGN based solely on having a broad Hα line, defined in their paper as $\sigma > 10$ Å, based on the fit of a single Gaussian to the emission line. In the case of a broad emission line this may inaccurately model the shape of the emission line and hence provide inaccurate measurements on properties such as equivalent width. Further to this, the selection of T1 AGN based solely on Hα likely includes partially obscured AGN (similar to our extended T1 selection). As we have shown, at least for our data, the partially obscured AGN population behaves similarly to the unobscured population (our bona fide T1 selection). As such we do not expect that this is the cause of the discrepancy between our observations.

There are also differences in how we select our T2 AGN. More specifically, like Villarroel & Korn (2014) we use equation 2.6 (Kewley et al., 2001) to select our T2s. This is a

conservative measure of nuclear activity and excludes composite star-forming galaxies with AGN component as well as some LINERs. However, in order to ensure the fidelity of our T2 sample, we further to this exclude as a LINER any galaxy that satisfies equation 2.7. Villarroel & Korn (2014) describe their method of selecting T2s in section 1.1.3 of the supplementary information of their paper, and how they remove LINERs in section 1.1.1. As they use the Kauffmann et al. (2003) criteria to select their T2s. Consequently, their T2 population may be more complete than ours, but may suffer from contamination by star-forming and composite SF-AGN galaxies. Further to this our exclusion of LINERs appears to be done using a different methodology. As such, it may the case that Villarroel & Korn (2014) and ourselves have T2 samples that are not drawn from the same parent population.

2.7 Summary and Conclusions

In this work we have analysed the environment of 954 spectroscopically-selected AGN from the GAMA II galaxy survey (Driver et al., 2011; Liske et al., 2015). Exploiting the high spectroscopic completeness of GAMA (Robotham et al., 2010) allows us to test recent observations suggesting different types of AGN reside in differing environments (Dultzin-Hacyan et al., 1999; Krongold et al., 2002; Koulouridis et al., 2006; Villarroel & Korn, 2014; Jiang et al., 2016). Thus, using GAMA we are able to comprehensively question the validity of the simple AGN unification scheme proposed by Antonucci (1993).

Having compared the fraction of T1 and T2 AGN found in pairs we find no significant differences, contrasting with previous works (Dultzin-Hacyan et al., 1999; Koulouridis et al., 2006; Jiang et al., 2016). This similarity in environment is maintained when our AGN-galaxy pairs are binned by projected separation and AGN [O III] λ5007 luminosity. Taking the case of the simple AGN unification scheme, should orientation of the AGN relative to our line of sight be the only difference between T1 and 2 AGN, and should this orientation be approximately random, then one would expect to see no differences in the pair fraction of AGN by type. Furthermore, we observe no significant difference in the neighbours of AGN of different types. The $u-r$, $g-i$, stellar masses, SFRs and sSFRs of the neighbouring galaxies all have similar distributions, confirmed by KS testing, with AGN type. Ergo, our observations here

support the AGN unification model.

The one environmental difference we do note with AGN type occurs in galaxy pairs separated by less than 20 kpc h^{-1} in projection. We find an excess of T2s in sub 20 kpc h^{-1} pairs relative to the extended T1 and general galaxy population in such close pairs. One possible explanation for this could be that the simple AGN unification model holds except in the case of close gravitational interactions, where the geometry of the dust distribution in the galaxy is disrupted such that the likelihood of obscuration is increased. Alternatively, it may be that the interaction between galaxies drives more dust toward the nuclear region and it is this way that the probability of obscuration is increased. In summary, our main findings are:

i The fraction of AGN found in pairs does not vary significantly with AGN type or pair separation down to 50 kpc h^{-1}. At separations of < 20 kpc h^{-1} and 500 km s^{-1} there appears to be an excess of T2 AGN but more data will be required to confirm this.

ii The $u-r$ colour of the inactive neighbouring galaxies of AGN in pairs of galaxies does not appear to change depending on whether the AGN is of the broad or narrow line variety in contrast with Villarroel & Korn (2014). The same result is found for the $g-i$ colours of the neighbouring galaxies to the AGN.

iii We find no difference in either the SFR or sSFR among the neighbouring galaxies of T1 and 2 AGN. We also find no difference in the fraction of these neighbours that are classed as star-forming according to a BPT diagram.

iv Comparing the distances to the 5th nearest neighbour of our AGN fails to find a difference between our broad and narrow line AGN populations.

v Our results are generally consistent with the unified model of AGN proposed by Antonucci (1993) and further still support the observations of Satyapal et al. (2014) and Kocevski et al. (2015).

The major hinderance to our observations has been our small sample size. GAMA II is highly complete allowing for spectroscopic observations of very close pairs of interacting galaxies. However, the survey footprint in the 3 equatorial regions (G09, G12, G15) is limited

to $\approx$ 180 square degrees. The small survey volume limits our ability to make statistically significant claims for well-matched AGN subsets, e.g., very close pairs with AGN of similar [O III] λ5007 luminosity. Therefore, we state that although most of our results are consistent with AGN unification, the apparent excess in T2s in very close pairs with $\mathrm{d}R < 20\,\mathrm{kpc}\,h^{-1}$ and $|\mathrm{d}V| < 500\,\mathrm{km\,s^{-1}}$ suggest that AGN unification may not be a complete model. The question of AGN unification is thus likely to remain an open one for the foreseeable future.

To answer this will likely require a spectroscopically complete survey with a larger volume to provide a statistically robust complete spectroscopic analysis of AGN environment. Such a dataset may be available within the next few years from TAIPAN (Transforming Astronomical Imaging surveys through the Polychromatic Analysis of Nebula). A major component of TAIPAN will be the Taipan galaxy survey (Hopkins et al., 2014; da Cunha et al., 2017) which will use the TAIPAN spectrograph (Kuehn et al., 2014) on the UK Schmidt Telescope at the AAO. The Taipan galaxy survey aims to observe $\approx$ 1000000 galaxies at $z < 0.3$ with high spectroscopic completeness across the Southern sky. This survey is currently in the advanced planning phase and is expected to commence 4 years of operations in the first half of 2018[1].

2.8 Acknowledgements

The authors wish to thank the anonymous referee for their constructive comments. YAG acknowledges the financial support of the University of Hull through an internally funded PhD studentship that has enabled this research to be undertaken, as well as discussions with Jacob Crossett and Dane Kleiner. MSO acknowledges the funding support from the Australian Research Council through a Future Fellowship (FT140100255). MLPG acknowledges CONICYT-Chile grant FONDECYT 3160492.

GAMA is a joint European-Australasian project based around a spectroscopic campaign using the Anglo-Australian Telescope. The GAMA input catalogue is based on data taken from the Sloan Digital Sky Survey and the UKIRT Infrared Deep Sky Survey. Complementary imaging of the GAMA regions is being obtained by a number of independent survey

[1]In the original publication of this paper, the expected survey date was stated as 2017. This has been updated in this thesis to reflect the unforeseen delays in survey operations.

programmes including GALEX MIS, VST KiDS, VISTA VIKING, WISE, Herschel-ATLAS, GMRT and ASKAP providing UV to radio coverage. GAMA is funded by the STFC (UK), the ARC (Australia), the AAO, and the participating institutions. The GAMA website is http://www.gama-survey.org/.

Funding for SDSS-III has been provided by the Alfred P. Sloan Foundation, the Participating Institutions, the National Science Foundation, and the U.S. Department of Energy Office of Science. The SDSS-III web site is http://www.sdss3.org/.

SDSS-III is managed by the Astrophysical Research Consortium for the Participating Institutions of the SDSS-III Collaboration including the University of Arizona, the Brazilian Participation Group, Brookhaven National Laboratory, Carnegie Mellon University, University of Florida, the French Participation Group, the German Participation Group, Harvard University, the Instituto de Astrofisica de Canarias, the Michigan State/Notre Dame/JINA Participation Group, Johns Hopkins University, Lawrence Berkeley National Laboratory, Max Planck Institute for Astrophysics, Max Planck Institute for Extraterrestrial Physics, New Mexico State University, New York University, Ohio State University, Pennsylvania State University, University of Portsmouth, Princeton University, the Spanish Participation Group, University of Tokyo, University of Utah, Vanderbilt University, University of Virginia, University of Washington, and Yale University.

This research made use of Astropy, a community-developed core Python package for Astronomy (Astropy Collaboration, 2013).

3. The Triggering and Inhibition of AGN in Large Scale Structure

"Stress and pain are the fundamental engines for improvement"

– Marco Pignatari, *private communication (2017)*

3.1 Prologue

Numerous studies have shown that central environment of massive clusters is hostile to efficiently accreting AGN (e.g. Gilmour et al., 2007; Gavazzi et al., 2011; Pimbblet et al., 2013, and references therein). The following chapter is the first in-depth study that probes down the halo mass function to test if the same effect is present in the less massive group population. This chapter has been published in the journal article MNRAS **475**, 4223 under the title *"Galaxy And Mass Assembly (GAMA): the effect of galaxy group environment on active galactic nuclei"* (Gordon et al., 2018). I led this paper and was responsible for the scientific direction of the work, data reduction and analysis, and the writing up of the paper, accounting for > 90 per cent of the work. My co-authors, Kevin Pimbblet, Matt Owers, Joss Bland-Hawthorn, Sarah Brough, Michael J. I. Brown, Michelle Cluver, Scott Croom, Benne Holwerda, Jonathan Loveday, Smriti Mahajan, and Lingyu Wang, provided scientific feedback on draft versions of the paper, and contributed to the GAMA observations and data products used throughout. As with Chapter 2, the differences between the thesis chapter and published article are negligible, limited to minor rewording and removal of the article abstract.

3.2 Introduction

Active galactic nuclei (AGN) are powered by the active accretion of matter onto the central super-massive black hole (SMBH) of a galaxy. Consequently, AGN may be triggered by mechanisms that introduce a new supply of cold gas, i.e., mergers (Sanders et al., 1988;

Krongold et al., 2002), that can then act as a fuel supply for nuclear activity. Alternatively, physical mechanisms that have the potential to destabilise the cold gas reservoirs already within a galaxy, such as harassment (Moore et al., 1996) or ram pressure stripping (RPS, Poggianti et al., 2017; Marshall et al., 2018), may trigger an infall of this gas toward the nucleus, where it can then be accreted by the SMBH.

Determining if these mechanisms actually do trigger AGN can be achieved by environmental analysis of the AGN host galaxies. The incidence of AGN has been shown to be enhanced in galaxies in very close pairs, and thus likely in the process of merging, relative to those galaxies not in a pair (Alonso et al., 2007; Woods & Geller, 2007; Ellison et al., 2011). Galaxy harassment and RPS occur within the denser environment of galaxy clusters. Here the infall of a galaxy toward the bottom of the gravitational potential well can both increase the number of high velocity close encounters a galaxy has (Moore et al., 1996), and subject the galaxy to the pressure of intra-cluster medium (ICM).

In the cluster environment at low-intermediate redshift, studies have shown that efficiently accreting AGN, i.e., not the radio-mode dominated AGN with intrinsically lower accretion rates (Hardcastle et al., 2007; Best & Heckman, 2012), preferentially inhabit regions of cluster projected phase-space associated with the infalling population (e.g., Ruderman & Ebeling, 2005; Haines et al., 2012; Pimbblet et al., 2013; Pentericci et al., 2013; Ehlert et al., 2013). That is to say AGN are found amongst the cluster population experiencing harassment and RPS for the first time (Mahajan et al., 2012).

In contrast to the infall region, the cluster cores have generally been observed to be relatively barren of AGN (Gilmour et al., 2007; Gavazzi et al., 2011; Pimbblet & Jensen, 2012, cf., Ruderman & Ebeling, 2005). That is not to say that AGN aren't found at all in cluster cores, indeed a small fraction of brightest cluster galaxies are known to harbour AGN (e.g., Best et al., 2007; Fraser-McKelvie et al., 2014; Green et al., 2016), but that they are relatively rare in comparison to the infall regions of the structure. This dearth of AGN in cluster cores may be the result of nuclear activity having run its course during the time it takes for the galaxy to fall into the cluster centre. Alternatively, it may be the case that the environment of the cluster core is unfavourable to AGN. The cores of relaxed massive clusters

have had time to virialise, and consequently the galaxy interactions in this region are high speed in nature and less conducive to galaxy mergers. The resultant lack of low-speed galaxy-galaxy interactions (Ostriker, 1980) may prevent AGN from being triggered in this region. Furthermore, the ram pressure experienced by galaxies close to the cluster centre may be too high to trigger an AGN (Marshall et al., 2018), instead stripping the galaxy of its gas. This may present observationally as one-sided tails (e.g. Kenney et al., 2004; Fumagalli et al., 2014) or 'jellyfish' galaxies should star formation occur in those tails (e.g. Owers et al., 2012; Ebeling et al., 2014). Such stripping would eventually starve an AGN of a potential fuel supply. A further mechanism which may inhibit nuclear activity in cluster cores is the temperature of the ICM. As the ICM may be of the order of tens of megaKelvin (Fabian, 1994), accretion onto galaxies is unlikely (Davies et al., 2017). In combination, these mechanisms result in galaxies in the cluster core that have an intrinsically low reservoir of cold gas (Giovanelli & Haynes, 1985) and thus cannot easily fuel an AGN.

Whilst these effects are well established in clusters, they may not extend to groups. Unlike clusters, which may contain many thousands of galaxies, groups have only up to a few tens of members, and significantly lower halo masses. The dynamics of the group environment may permit more galaxy-galaxy interactions that are effective in driving gas toward the galactic nucleus within in the group centre. Furthermore, the lower halo masses of groups will result in a smaller heating effect from the virial shock acting on the intra-group medium (IGM, Grootes et al., 2017). This may allow for easier, or more rapid, accretion of the IGM onto galaxies and act as a potential fuel reservoir. Finally, the lower density of the galaxy groups results in lower ram pressures affecting infalling galaxies (Marshall et al., 2018). Consequently RPS will be less likely to strip a galaxy of a large fraction of its gas. Ergo, these environmental differences between group and cluster galaxies may foster the presence of AGN in the cores of groups.

While galaxy groups have been shown to have a higher global AGN fraction than clusters (Shen et al., 2007; Arnold et al., 2009; Tzanavaris et al., 2014; Oh et al., 2014), it is unestablished whether the effects of position in projected phase-space seen in clusters are present or absent in groups. Where efforts have been made to study the effect of groups on AGN

these studies are limited by small numbers of detected groups. This hinders the ability to stack groups to perform a phase-space analysis with any level of statistical confidence. The Galaxy And Mass Assembly survey (GAMA, Driver et al., 2011; Liske et al., 2015) is highly spectroscopically complete (98 per cent at $r < 19.8$ mag, Liske et al., 2015) making it well suited to environmental analyses of galaxies (e.g., Brough et al., 2013; Casteels et al., 2014; Robotham et al., 2014; Alpaslan et al., 2015; Davies et al., 2016; Ching et al., 2017; Gordon et al., 2017; Barsanti et al., 2018). GAMA is thus ideal for studying the lower halo mass regime of galaxy groups and has detected more than 23000 groups with 2 – 316 members (Robotham et al., 2011).

In this work we investigate the effect of the group environment on galactic nuclear activity by using spectroscopically selected AGN and version 9 of the GAMA group catalogue. We analyse prevalence of AGN as a function of group mass and position in group projected phase-space. For our analysis we only use groups with at least 5 members (full details are given in Chapter 3.3.2). We are thus expanding on the work of Pimbblet et al. (2013) and probing further down the group halo mass function, and, as a result of the depth of GAMA, to lower galactic stellar masses.

In Chapter 3.3 we detail the GAMA survey and the specific data used in this work. Our results are given in Chapter 3.4, and our discussion is presented in Chapter 3.5. Chapter 3.6 is a summary of our conclusions. Throughout this chapter a standard flat ΛCDM cosmology is assumed with $h = 0.75$, $H_0 = 100h\,\mathrm{km\,s^{-1}\,Mpc^{-1}}$, $\Omega_M = 0.25$ and $\Omega_\Lambda = 0.75$.

3.3 Data

3.3.1 Galaxy And Mass Assembly

The GAMA survey spectroscopic campaign was undertaken with the Anglo-Australian telescope (AAT) at Siding Spring Observatory between 2008 and 2014 (Driver et al., 2011; Liske et al., 2015). During this period, spectra with a resolution of $R \approx 1300$ covering the wavelength range 3750 – 8850 Å were obtained using the 2dF/AAOmega spectrograph for over 250,000 galaxies (Hopkins et al., 2013). The GAMA survey footprint covers 5 regions of the sky totalling 286 deg^2 with extremely high spectroscopic completeness. Specifically, at

$r < 19.8$ mag, completeness is > 98 per cent in the three equatorial regions (G09, G12, G15), which we use in this work.

3.3.2 Galaxy groups

The GAMA group catalogue G^{3}Cv09

The depth and completeness of GAMA naturally lends itself to the reliable detection of galaxy groups of lower mass than would be possible with a shallower and less spectroscopically complete survey. The resultant GAMA group catalogue is constructed through the use of a friends-of-friends (FoF) algorithm (Robotham et al., 2011). We use the latest version of the group catalogue, G^{3}Cv09, which covers the three GAMA equatorial regions, and contains 75029 galaxies in 23654 groups with $z < 0.6$. The number of group members, $N_{\rm FoF}$, ranges from 2 (14876 groups) to 316 (Abell 1882, Owers et al., 2013).

We select the groups for use in this work to be within a suitable redshift so that we can be confident in our mass completeness, and having enough group members such that low group multiplicity does not bias our projected phase-space analysis. To determine a redshift limit to use we use the distribution of maximum observable redshift of the GAMA galaxies at $r < 19.8$ mag, as calculated by Taylor et al. (2011). By limiting our analysis to $z < 0.15$, we are able to probe down to a stellar mass of $10^{9.9}$ M$_\odot$ with 90 per cent completeness.

Group membership

The FoF algorithm used to determine the group membership in G^{3}Cv09 is more reliable at detecting low mass groups than halo-galaxy grouping methods (Robotham et al., 2011). However, this method preferentially detects group members at low projected radii (Barsanti et al., 2018), and hence will bias the results of any projected phase-space analysis conducted. To counter this, we define our own group sample membership, using the GAMA group catalogue as a starting point. Using the observed group velocity dispersion, $\sigma_{\rm group}$, we calculate R_{200} as per (Carlberg et al., 1997),

$$R_{200} = \frac{\sqrt{3}\sigma_{\rm group}}{10H(z)}, \tag{3.1}$$

and the halo masses, M_{200}, using

$$M_{200} = \frac{\sigma^3_{\rm group}}{1090^3 h(z)} 10^{15}\,{\rm M}_\odot \tag{3.2}$$

derived by Munari et al. (2013). Using the central galaxy from the respective FoF group as our group centre, we then count galaxies within $3.5\sigma_{\rm group}$ and $3.5R_{200}$, comparable to the analysis conducted by Pimbblet et al. (2013), as group members. When compared to mock catalogues, derived group parameters are shown to be more reliable for GAMA groups with $N_{\rm FoF} \geq 5$ (Robotham et al., 2011) suggesting that these groups are more representative of the expected group population. We thus use only these groups as the seeds for our group sample.

At high projected separation and velocities, interloping field galaxies that are serendipitously selected in the group may be a source of substantial sample contamination (Rines et al., 2005; Oman & Hudson, 2016; Owers et al., 2017). To counter this, we further require that galaxies satisfy the infall criteria of spherical Navarro-Frenk-White (NFW, Navarro et al., 1996) profiles as per the method used by Barsanti et al. (2018). That is,

$$V_{\rm infall}(R/R_{200}) < V_{200}\sqrt{\frac{2}{R/R_{200}}\frac{\ln(1+\kappa R/R_{200}) - (\kappa R/R_{200})/(1+\kappa R/R_{200})}{\ln(1+\kappa) - \kappa/(1+\kappa)}}, \tag{3.3}$$

where κ is the Dolag et al. (2004) halo concentration index given by

$$\kappa(M_{200}, z) = \frac{9.59}{1+z_{\rm group}}\left(\frac{M_{200}}{10^{14}\,{\rm M}_\odot\,h^{-1}}\right)^{-0.102}, \tag{3.4}$$

$z_{\rm group}$ is the median redshift of the group, and $V_{200} = \sqrt{{\rm G}M_{200}/R_{200}}$.

One potential complication of this method is the potential for galaxies being assigned to multiple groups. In this event, a galaxy is assigned to the group that provides the smallest value for the parameter C (Smith et al., 2004). C is given by

$$C = \frac{(cz_{\rm gal} - cz_{\rm group})^2}{\sigma^2_{\rm group}} - 4\log_{10}\left(1 - \frac{R}{R_{\rm group}}\right) \tag{3.5}$$

where R is the projected separation of the galaxy from the group centre, and $R_{\rm group}$ is $3.5R_{200}$. We further require that at least 5 members are assigned to each group via this method to be counted in our projected phase-space analysis, resulting in a sample of 723 groups at $z_{\rm group} < 0.15$.

Group substructure

For high-multiplicity groups, we do not wish to bias our results due to any significant substructure that may be present in the group core. To ensure this is not the case, we subject large groups to a Δ, or DS (Dressler & Shectman, 1988) test for subclustering. Note that it is the centres of groups in which we are concerned about substructure. To find substructure here would indicate that the group is not a virialised structure and hence unsuitable for our analysis of projected phase-space as this may affect the likelihood of AGN to be found in this region. Moreover, such central substructure may influence the measured dynamical mass of a group. The DS test is sensitive to substructure in group sizes as low as 30 members. We therefore perform this test on groups with at least 30 members within R_{200} of the group centre. Of our 723 groups, 41 satisfy this criterion.

To apply the DS test, for each galaxy, i, the n nearest neighbours are used to determine a local mean velocity and velocity dispersion. These are then compared to the group global values and a statistic, δ, can be calculated by:

$$\delta_i^2 = \frac{n+1}{\sigma_{\rm global}}[(v_{\rm local} - v_{\rm global})^2 + (\sigma_{\rm local} - \sigma_{\rm global})^2] \tag{3.6}$$

where v is the mean velocity and σ the velocity dispersion. For each group a cumulative statistic, Δ is obtained by $\Delta = \Sigma\delta_i$. Pinkney et al. (1996) and Einasto et al. (2012) recommend that the number of nearest neighbours, n, be the square root of the number of galaxies used to determine the the cumulative statistic, Δ, i.e., $n = \sqrt{N_{R<R_{200}}}$. A p-value for the absence of substructure is obtained by calibrating Δ by the use of Monte Carlo simulations whereby $p = N(\Delta_{\rm MC} > \Delta_{\rm obs})/N({\rm MC})$. Such simulations are performed by randomly shuffling the galaxy velocities, therefore removing any locally coherent velocity substructure information that is the result of dynamical substructure within the group. For our DS tests we run 1000 Monte Carlo simulations. Given this, and the sensitivity of the DS test to substructure of the order 1/7 of the total cluster mass (Pinkney et al., 1996), a low p-value is indicative of significant substructure. Of the 41 groups we subjected to the DS test, 18 resulted in $p < 0.01$, and were hence eliminated from the analysis.

This leaves us with 7498 galaxies with $M_* > 10^{9.9}\,{\rm M}_\odot$ in 695 groups of between 5 and 418

Table 3.1: The number of group members(N), group velocity dispersion ($\sigma_{\rm group}$), radius (R_{200}), and mass(M_{200}) of the groups used for the projected phase-space analysis in this paper. For each property, the mean, standard deviation and the 0th, 25th, 50th, 75th, and 100th percentiles are given.

Group property	μ	σ	Min	Q_1	Q_2	Q_3	Max
N	21.49	26.89	5.00	9.00	15.00	25.00	418.00
$\sigma_{\rm group}$[km/s]	248	103	69	173	228	304	718
R_{200} [kpc/h]	548	226	159	381	504	675	1567
$\log_{10}(M_{200}/{\rm M}_\odot)$	13.06	0.54	11.53	12.71	13.07	13.45	14.56

members, the distributions of the group multiplicity, velocity dispersions, and halo masses of this sample are described in Table 3.1, and the halo mass and redshift distributions are shown in full in Figure 3.1.

3.3.3 AGN selection

A complete AGN sample

The GAMA AGN sample of Gordon et al. (2017) contains 954 broad- and narrow-line AGN, relying on the Kewley et al. (2001) criteria,

$$\log_{10}\left(\frac{[\text{O III}]\ \lambda5007}{\text{H}\beta}\right) > \frac{0.61}{\log_{10}\left(\frac{[\text{N II}]\ \lambda6583}{\text{H}\alpha}\right) - 0.47} + 1.19 \tag{3.7}$$

to classify narrow-line AGN on a Baldwin-Phillips-Terlevich (BPT, Baldwin et al., 1981) diagnostic diagram. This requires the detection of four emission lines, Hβ, [O III] λ5007, Hα, [N II] λ6583 at S/N $>$ 3, and, consequently, is a conservative selection in that it prioritises sample fidelity ahead of completeness. Cid Fernandes et al. (2010) found that only forty per cent of emission line galaxies in the "right wing" and AGN areas of the BPT diagram may be detected with S/N $>$ 3 in both Hβ and [O III] λ5007, and thus be selected as AGN. That is to say, in order to preserve sample fidelity, the criteria of Kewley et al. (2001) may miss a majority of narrow-line AGN.

To account for this, Cid Fernandes et al. (2010) proposed selecting narrow-line AGN on the basis of the two stronger emission lines, Hα and [N II] λ6583. Using these two emission lines, AGN may be selected by comparing the ratio of [N II] λ6583 to t Hα, to the equivalent width

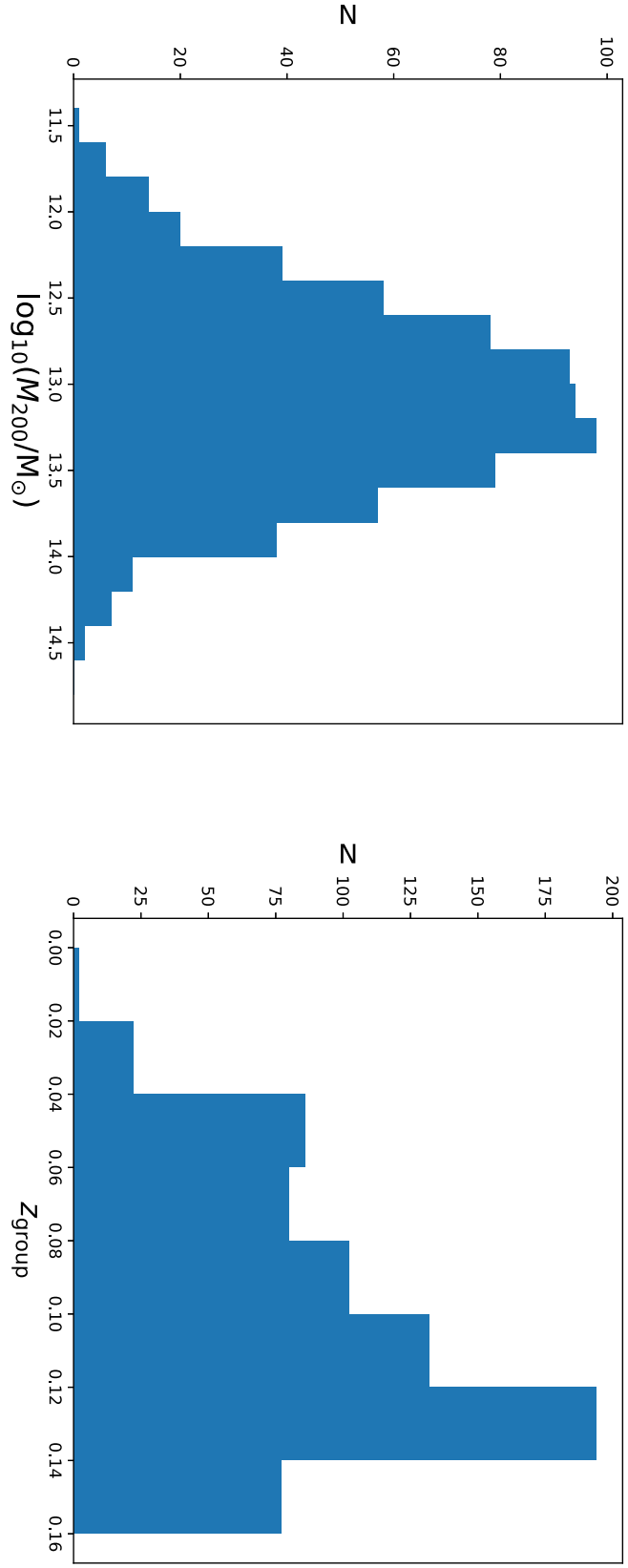

(a) (b)

Figure 3.1: The distributions of the halo mass (M_{200}, a) and median redshift (b) of our group sample.

of Hα. The resultant so called 'WHAN' diagram (Cid Fernandes et al., 2011) categorises emission line galaxies (ELGs) as having $\mathrm{EW}_{\mathrm{H}\alpha} > 3$ Å, and:

- star-forming, $\log_{10}\left(\frac{[\mathrm{N\,II}]\ \lambda6583}{\mathrm{H}\alpha}\right) < -0.4$
- weak AGN, $\log_{10}\left(\frac{[\mathrm{N\,II}]\ \lambda6583}{\mathrm{H}\alpha}\right) > -0.4$ and $\mathrm{EW}_{\mathrm{H}_\alpha} < 6$ Å
- strong AGN, $\log_{10}\left(\frac{[\mathrm{N\,II}]\ \lambda6583}{\mathrm{H}\alpha}\right) > -0.4$ and $\mathrm{EW}_{\mathrm{H}_\alpha} > 6$ Å

where the category 'weak AGN', are the less powerful counterparts to the 'strong AGN', but where the AGN is still considered to be the dominant ionisation mechanism (Cid Fernandes et al., 2011). Galaxies with $\mathrm{EW}_{\mathrm{H}\alpha} < 3$ Å are considered to be passive in nature.

To select our AGN using the WHAN criteria, we select the best spectrum available for galaxies in our group sample with $nQ \geq 3$, i.e., a greater than 90 per cent confidence in the measured redshift (Driver et al., 2011; Liske et al., 2015). We use only spectra with Hα and [N II] λ6583 in emission. This requires that the Gaussian has been successfully fit to each line in SpecLineSFRv05, the values and errors on flux and equivalent widths to be greater than zero, and the signal to noise ratio on both lines is greater than 3. For AAT obtained spectra we use only those spectra unaffected by fringing [1]. Furthermore, it is difficult to obtain reliable mass estimates for broad-line AGN (Gordon et al., 2017) and we hence exclude them from this analysis. Thus, we only use galaxies that do not have a broad component to the Hα line, i.e., a single Gaussian fit is preferred (see Chapter 2.3.3).

These criteria select 2864 emission line galaxies from the 7498 in our group sample. In order to account for Balmer absorption, the flux and equivalent width of the Hα line are corrected, as per Hopkins et al. (2013), by:

$$S_{\mathrm{H}\alpha,\,\mathrm{intrinsic}} = S_{\mathrm{H}\alpha,\,\mathrm{observed}}\left(\frac{\mathrm{EW}_{\mathrm{H}\alpha} + 2.5\ \text{Å}}{\mathrm{EW}_{\mathrm{H}\alpha}}\right) \tag{3.8}$$

[1] Approximately 5 per cent of AAOmega spectra suffer from a time-dependent fringing artefact (Hopkins et al., 2013, see also Chapter 2.4 and Figure 2.3), this is flagged in the GAMA catalogue AATSpecAllv27.

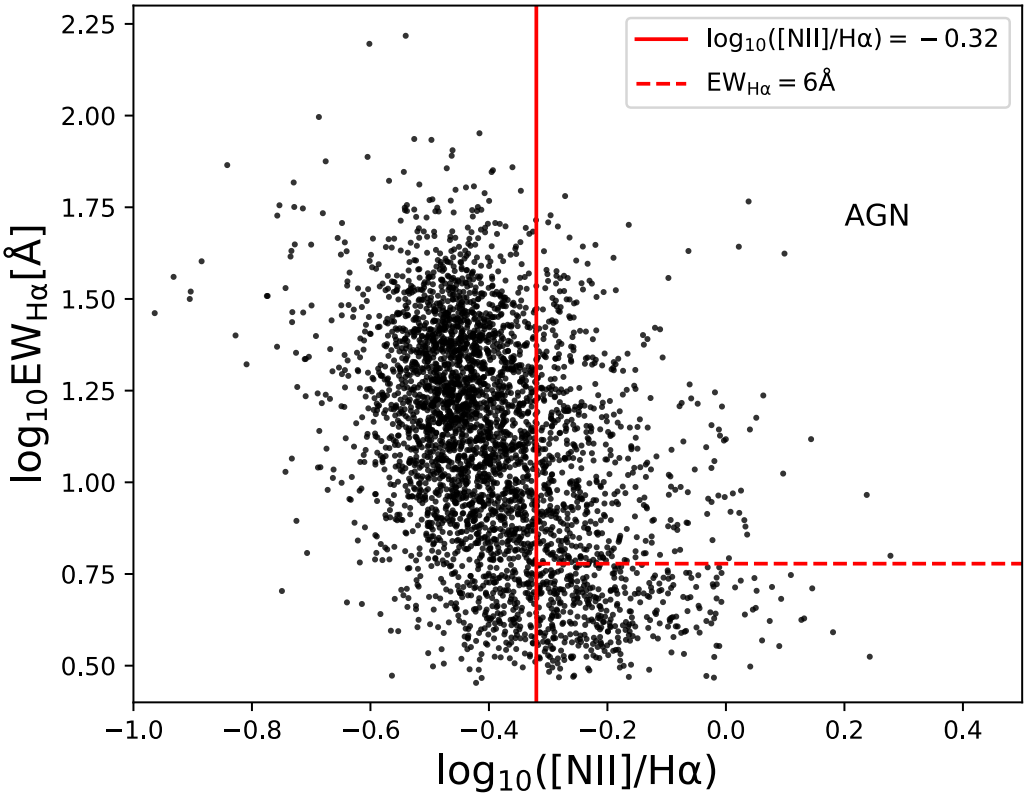

Figure 3.2: A WHAN diagram of the emission line galaxies selected in our group sample. The horizontal red dashed line is used to segregate AGN from weak AGN composites, and LIERs. The vertical red line is $\log_{10}([\mathrm{N\,II}]\ \lambda6583/\mathrm{H}\alpha) = -0.32$ which defines the boundary between the star-forming and AGN regions of the plot. To be classified as an AGN a galaxy must be located above the red dashed line and to the right of the red solid line. Note the absence of galaxies with $\log_{10}(\mathrm{EW}_{\mathrm{H}\alpha}/\text{Å}) < 0.5$, a consequence of the stringent selection criteria applied.

The WHAN diagram of the emission line galaxies is shown in Figure 3.2. Note, that because of the strict criteria imposed to ensure the reliability of the detected emission lines, the passive galaxy section of this diagram is barren.

Sample contamination

Although such an AGN selection will be more complete than more conservative methods, the level of contamination from galaxies ionised by a non-AGN source will naturally be higher. Given that the WHAN and BPT diagrams share an axis, this contamination can be visualised

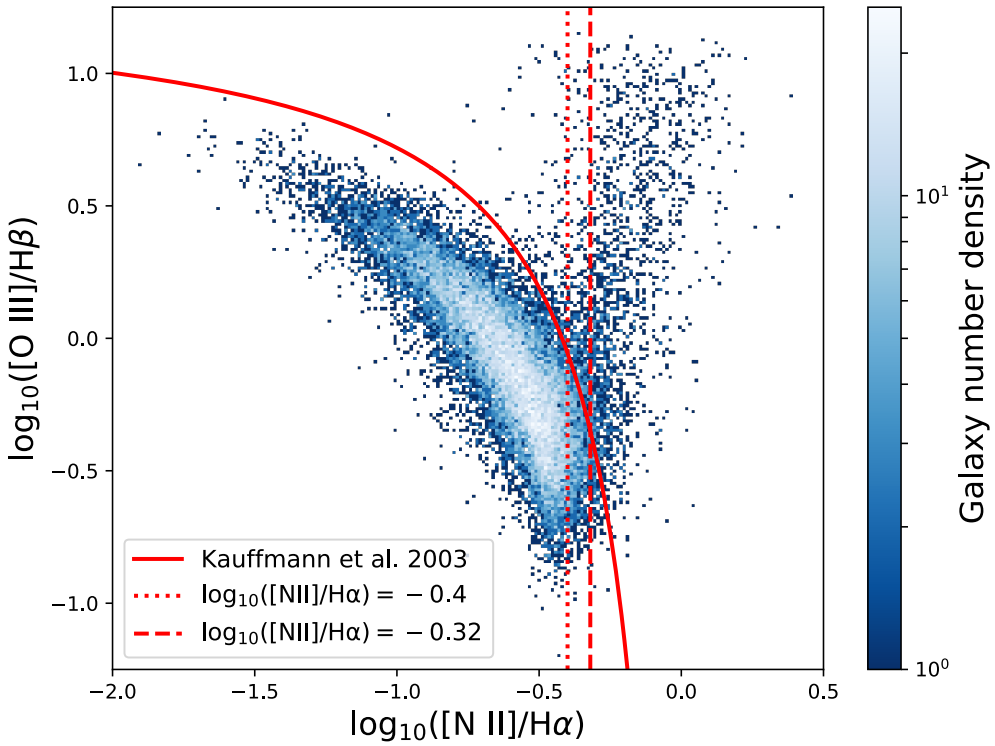

Figure 3.3: A BPT diagram of the emission line galaxies in GAMA. The Kauffmann et al. (2003) line is plotted as the solid red curve. The red dotted line shows $\log_{10}([\mathrm{N\,II}]\ \lambda6583/\mathrm{H}\alpha) = -0.4$, often used to select AGN in WHAN diagnostic criteria. The red dashed line shows $\log_{10}([\mathrm{N\,II}]\ \lambda6583/\mathrm{H}\alpha) = -0.32$ used to select AGN in this work. The large fraction of star forming galaxies located between the two vertical lines is readily apparent.

by over-plotting the Cid Fernandes et al. (2010) AGN/SF segregation on to the BPT (See Figure 3.3). To quantify, and minimise this, one can compare the classifications on both the WHAN and BPT of galaxies where all four BPT lines are detected with S/N > 3. For this, we classify those galaxies satisfying the Kewley et al. (2001) criteria (equation 3.7) as AGN, those satisfying the Kauffmann et al. (2003) criteria,

$$\log_{10}\left(\frac{[\mathrm{O\,III}]\ \lambda5007}{\mathrm{H}\beta}\right) < \frac{0.61}{\log_{10}\left(\frac{[\mathrm{N\,II}]\ 6583}{\mathrm{H}\alpha}\right) - 0.05} + 1.3 \tag{3.9}$$

as star-forming galaxies, and those galaxies not satisfying either criteria as composite sources.

Applying these criteria to WHAN selected AGN, shows that contamination of the AGN population by star-formers is limited to those AGN with the lowest [N II] λ6583:Hα ratios. The [N II] λ6583:Hα used in the WHAN diagram is derived from the Stasińska et al.

(2006) AGN/star-forming segregation. Transposing the more conservative Kauffmann et al. (2003) AGN/star-forming segregation on to the WHAN diagram would result in galaxies with $\log_{10}([\mathrm{N\,II}]\ \lambda6583/\mathrm{H}\alpha) < -0.32$ being classified as star-forming. Indeed, when only galaxies with $-0.4 < \log_{10}([\mathrm{N\,II}]\ \lambda6583/\mathrm{H}\alpha) < -0.32$ are considered, star-formers make up $75.88^{+1.06}_{-1.13}$ per cent of the population with all four BPT lines at S/N > 3. When only galaxies with $\log_{10}([\mathrm{N\,II}]\ \lambda6583/\mathrm{H}\alpha) > -0.32$ are considered, the contamination of the sample by star forming galaxies is reduced to $11.07^{+0.99}_{-0.85}$ per cent. Given the decreasing detections of all four BPT lines with increasing [N II] λ6583:Hα ratio shown in Cid Fernandes et al. (2010), we take this as an upper limit on the star-forming contamination of the ELG sample.

While altering the minimum [N II] λ6583:Hα ratio of our sample will reduce the contamination from pure star-forming sources, the contribution from the composite population is substantial. There are various arguments as to the nature of this population with a variety of sources thought to contribute. Kewley et al. (2001) argue that galaxies can be classified as a composite solely as the result of ionisation from an extreme starburst phase. However, the sample contamination from such sources will be minimal. Taking the Poggianti & Wu (2000) e(b) classification as a proxy for the starburst population, we find these galaxies constitute < 1 per cent of the ELG population in GAMA. Ionisation from post-AGB stars is likely to be a considerable source of contamination for the composite population. Furthermore, the Kewley et al. (2001) AGN population will be contaminated by low-ionisation emission regions (LIERs). Both of these contaminants present with weak hydrogen lines (Fig. 2 of Marshall et al., 2018; Sanchez et al., 2017), and thus their contribution to an AGN selection can be minimised by only selecting AGN with strong Hα, i.e., EW > 6 Å, emission.

To achieve a balance between high sample completeness and fidelity, we select our AGN using a conservative variant of the WHAN diagnostic criteria. Specifically we classify as AGN galaxies with $\log_{10}([\mathrm{N\,II}]\ \lambda6583/\mathrm{H}\alpha) > -0.32$ and $\mathrm{EW}_{\mathrm{H}\alpha} > 6$ Å. This produces a sample of 451 AGN in our selected groups.

3.4 Observations and Analysis

3.4.1 The group AGN fraction

Taking the group population as a whole, we find that AGN constitute $6.01^{+0.29}_{-0.26}$ per cent of the galaxies more massive than $10^{9.9}$ $M_\odot$ in our sample. Given that the masses of our groups span three orders of magnitude (See Table 3.1) we wish to determine whether this AGN fraction is dependent on the mass of the group. In Figure 3.4 we split our group sample in to four bins of M_{200}. We show that the AGN fraction is approximately flat at halo mass of $\log_{10}(M_{200}/M_\odot) > 13$. Lower mass groups have a higher, if not significantly so, AGN fraction than higher mass groups. For all fractional calculations, both here and throughout this paper, the errors are binomial as per Cameron (2011).

3.4.2 AGN in group projected phase-space

It has been shown that for massive clusters AGN, are preferentially found in the infall regions of those clusters, and are less likely to be found in the cluster centre (Haines et al., 2012; Pimbblet et al., 2013). To test if this is the case in lower mass groups, we stack our selected groups into one large 'super-group' of 7498 galaxies. We then analyse the positions of those galaxies in the projected radius versus velocity difference phase-space plane. In order for this projected phase-space to be useable for our stacked group we must normalise the dimensions. For the projected separation, we use the projected separation of a galaxy from the iterative centre of the group, and normalise by R_{200}. To calculate the velocity difference, we use the difference between the redshift of the galaxy and the median redshift of the group, i.e., $\Delta v = c(z_{\rm gal} - z_{\rm group})/(1 + z_{\rm group})$. This is normalised by the group velocity dispersion.

Ehlert et al. (2013) and Pimbblet et al. (2013) showed that AGN fraction increases with projected radius from the cluster centre. Given this established result for clusters, we test whether the same result holds for galaxy groups. In Figure 3.5 we show the same trend for our group sample. In order to test whether this effect is biased by the large mass range of groups in our sample, we repeat this test for the upper and lower quartiles of the mass distribution of our group sample. This shows that the low AGN fraction inside R_{200} is driven by high-mass groups, where the AGN fraction is lower at $R < R_{200}$ at 2.9σ confidence.

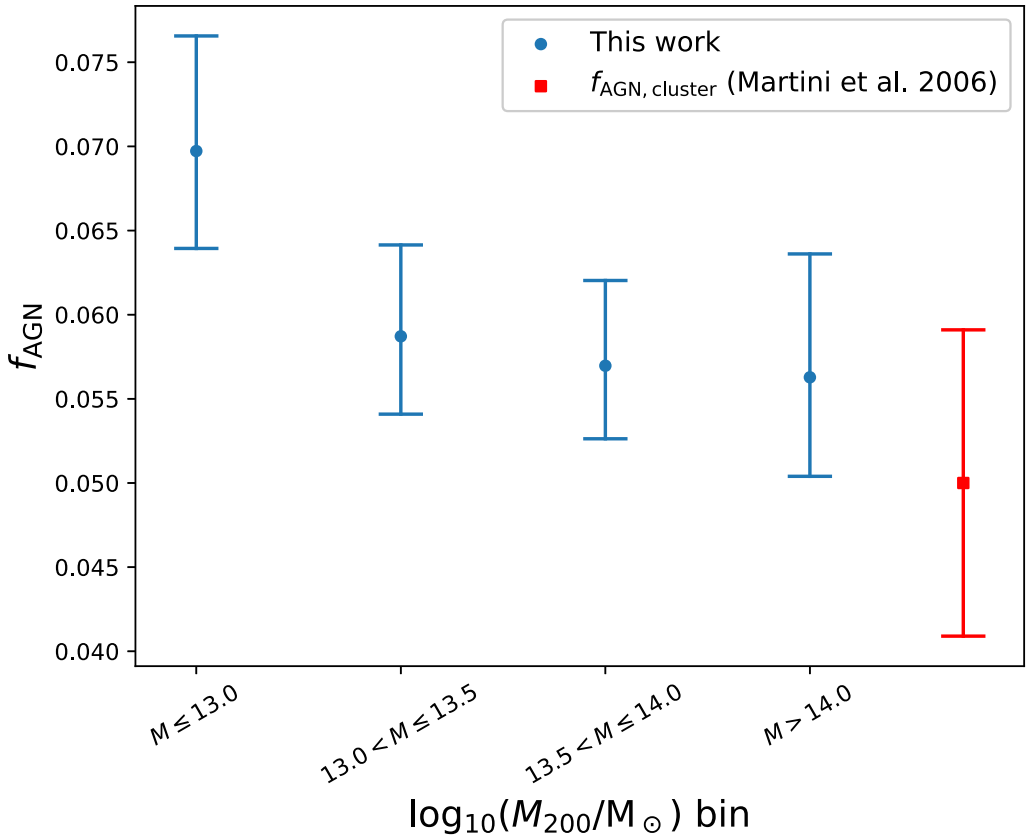

Figure 3.4: The fraction of the galaxy population hosting an AGN in bins of group mass, M_{200}. The AGN fraction is flat for $M_{200} > 10^{13.0}\,\mathrm{M}_\odot$, and marginally elevated at lower halo masses. The red square shows the AGN fraction in clusters, and 1σ errors, obtained from Martini et al. (2006) for comparison.

In Figure 3.6 we show the relative number densities of galaxies and AGN in projected phase-space and the expected infall curve from the work of Oman et al. (2013). This curve is defined as

$$\frac{|v|}{\sigma_{\mathrm{group,\,3D}}} = -\frac{4}{3}\frac{R}{R_{\mathrm{virial}}} + 2 \tag{3.10}$$

where $R_{\mathrm{viral}} = \frac{2.5}{2.2} R_{200}$ (Oman et al., 2013), and $\sigma_{\mathrm{group,\,3D}}$ is the three-dimensional equivalent of σ_{group}, i.e., $\sqrt{3}\sigma_{\mathrm{group}}$ (Barsanti et al., 2018). By comparing with this expected infall curve, Figure 3.6 shows qualitatively that, as one might expect for virialised structures, the number density of galaxies is higher below this curve. The number density of AGN, however, is seen to be more widely distributed, and the AGN fraction is highest in the infall regions, i.e. above

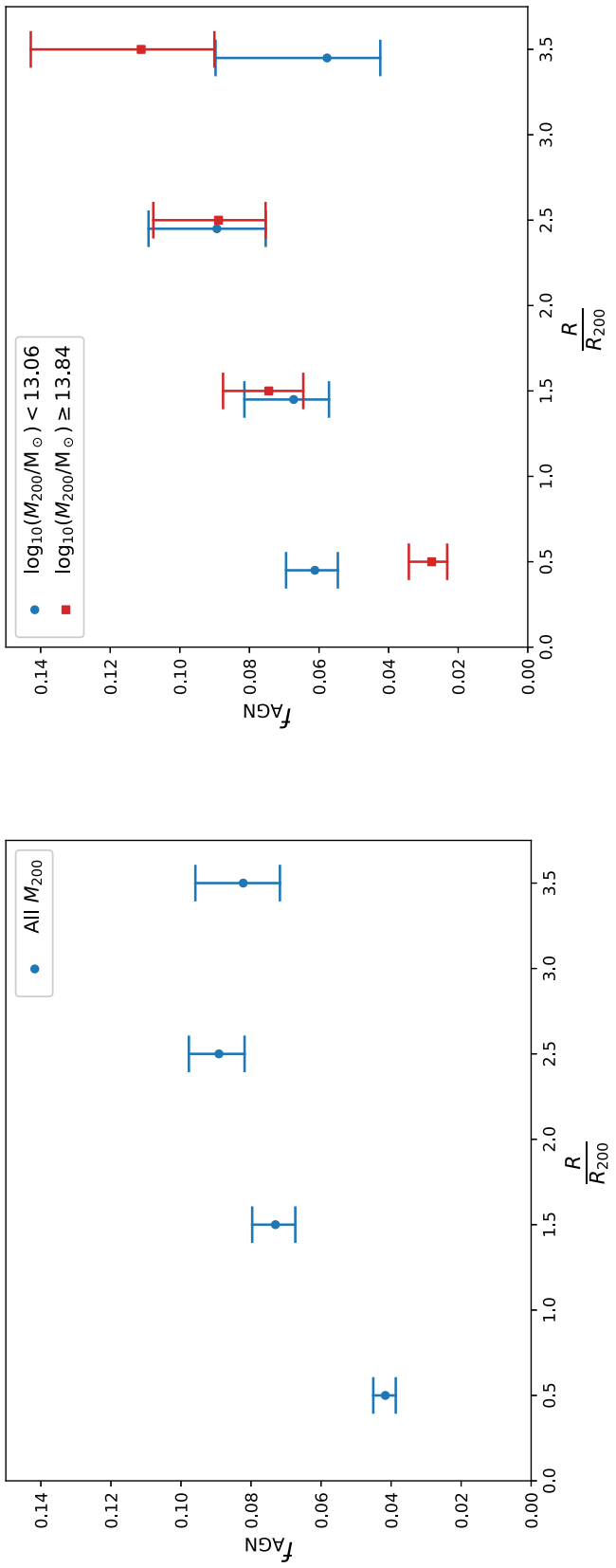

Figure 3.5: The effect of projected separation from group centre on AGN fraction. In panel (a) the entire group sample is considered. Panel (b) splits the sample into the upper and lower quartiles of the group mass distribution, showing that low mass groups don't have the deficit of centrally located AGN seen in high-mass groups and clusters (Ehlert et al., 2013; Pimbblet et al., 2013). For panel (b) blue circles represent groups with $\log_{10}(M_{200}/\mathrm{M}_\odot) < 13.06$, while groups with $\log_{10}(M_{200}/\mathrm{M}_\odot) > 13.84$ are shown by red squares, these are marginally offset along the x-axis for clarity. For both panels the bin width is R_{200} for all bins.

the Oman et al. (2013) curve.

The AGN fractions calculated for the bins in Figure 3.6 have a median absolute error of 0.02. To reduce this error and better quantify the difference in AGN triggering likelihood with environment, we calculate the AGN fractions for the virialised and infalling galaxy populations as defined by equation 3.10. For our stacked group, the AGN fraction in the virialised region is $4.50^{+0.36}_{-0.32}$ per cent compared to $7.56^{+0.46}_{-0.41}$ per cent in the infall regions. Across our sample, AGN are morel likely to be found in infalling galaxies with 3.9σ confidence.

As with the overall group AGN fraction, and the effect of projected separation from the group centre, we wish to test whether this preference for AGN to be found in the infalling population is driven by groups in a particular mass regime. In Figure 3.7, we show the galaxies and AGN in projected phase-space for the lower and upper quartiles, in terms of halo mass, of our sample. We also show the histograms for active and inactive galaxies in each of the projected phase-space dimensions, which clearly show a difference in the distribution of AGN at these halo mass regimes. To quantify this, we attempt to constrain at what group mass the environmental transition occurs. In Figure 3.8, we bin the mass range of our sample and compare the likelihood of virialised and infalling galaxies hosting an AGN. This shows a decreasing AGN fraction amongst virialised galaxies with increasing group mass. At $\log_{10}(M_{200}/\mathrm{M}_\odot) > 13.50$ the observed AGN deficit in the group centre becomes significant at the 3.6σ level. For group halo masses greater than $10^{13.5}\,\mathrm{M}_\odot$, $3.70^{+0.50}_{-0.40}$ per cent of the virialised galaxy population host an AGN, in contrast to $7.55^{+0.66}_{-0.57}$ per cent of the infalling population.

3.5 Discussion

3.5.1 AGN in large-scale structure

The dynamics of large-scale structure (LSS) change with structure size. For instance, one would not expect that a galaxy pair would have a similar kinematic environment to a larger group of many tens of members, the latter of which may well be virialised. Galaxy pairs, especially a close pair, and small groups of only a few members are likely to be directly interacting (Hickson, 1997; Robotham et al., 2014), a widely considered trigger for nuclear

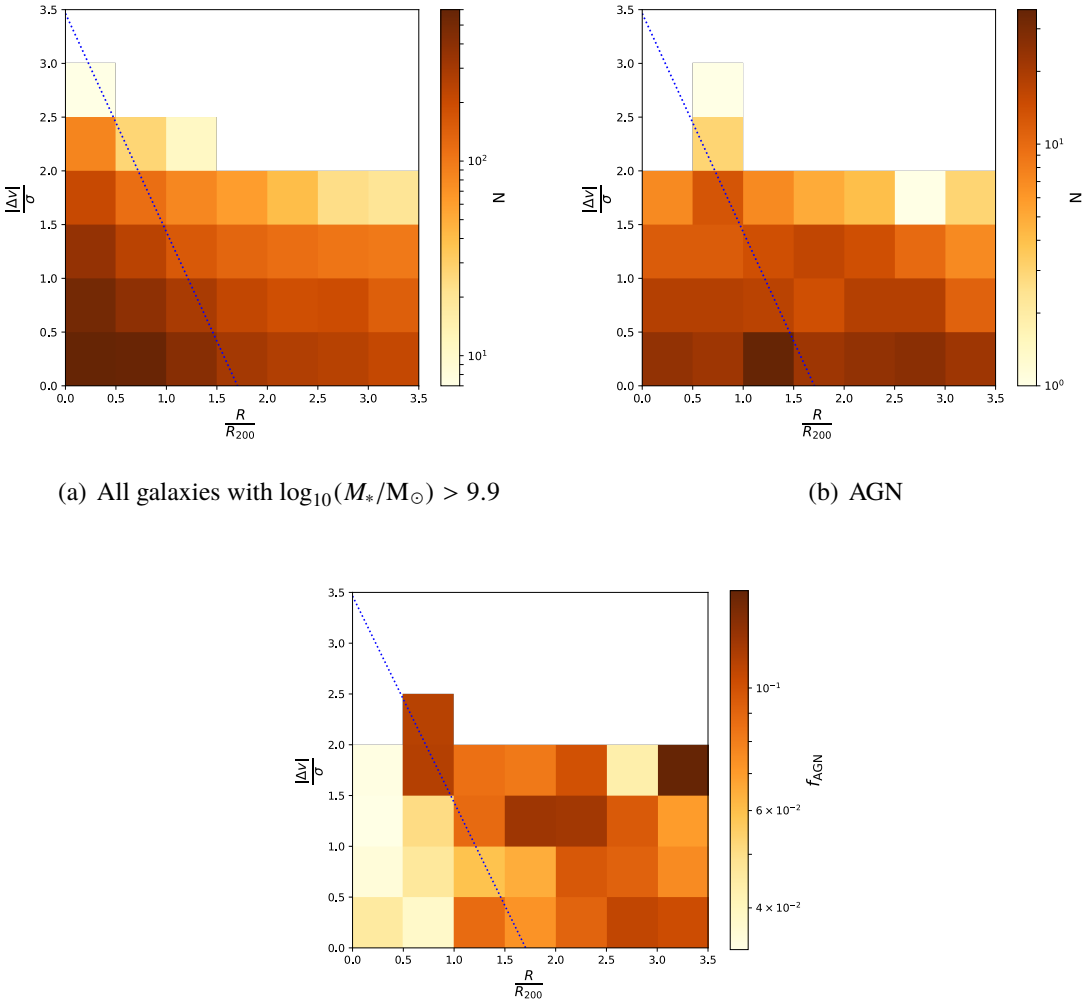

(a) All galaxies with $\log_{10}(M_*/\mathrm{M}_\odot) > 9.9$

(b) AGN

(c) AGN fraction

Figure 3.6: Two dimensional histograms showing the projected phase-space distributions of our stacked group of 7498 galaxies. Panel (a) shows the number density of all galaxies, panel (b) shows the number density of AGN, and panel (c) shows the AGN fraction. The blue dotted line shows the modelled infall curve of Oman et al. (2013). The median absolute error for the AGN fractions in panel (c) is 0.02.

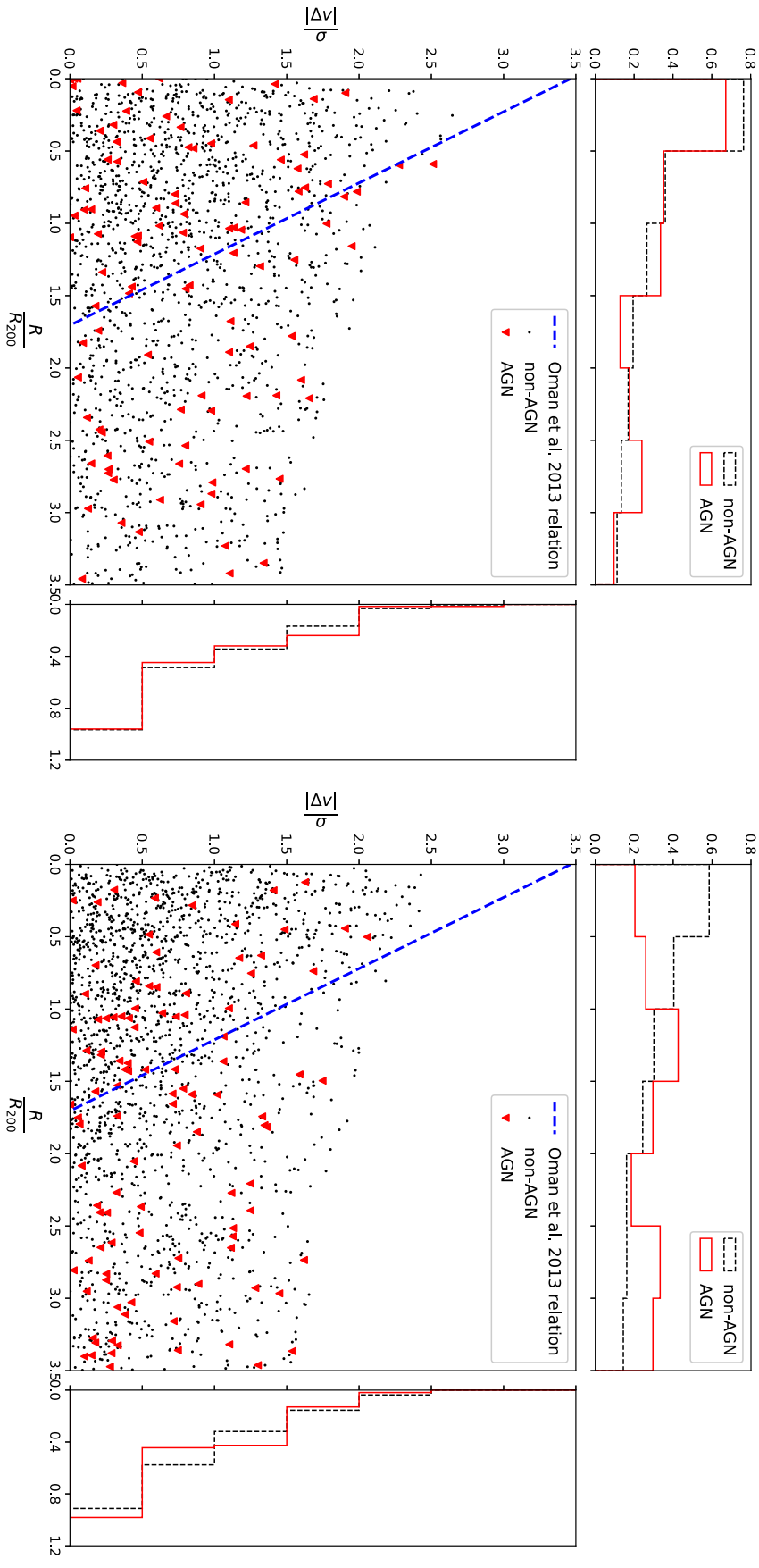

(a) $\log_{10}(M_{200}/M_\odot) < 13.06$

(b) $\log_{10}(M_{200}/M_\odot) > 13.84$

Figure 3.7: The projected phase-space diagrams and histograms for groups in the lower (panel a) and upper (panel b) quartiles of the group halo mass distribution. Inactive galaxies are represented by black dots in the phase-space diagram and black dashed line in the histograms, and AGN are represented by red triangles and red solid lines in these plots respectively. The blue dashed line marks the Oman et al. (2013) infall curve. Panel b clearly shows a low number of AGN at low projected radii relative to the inactive population.

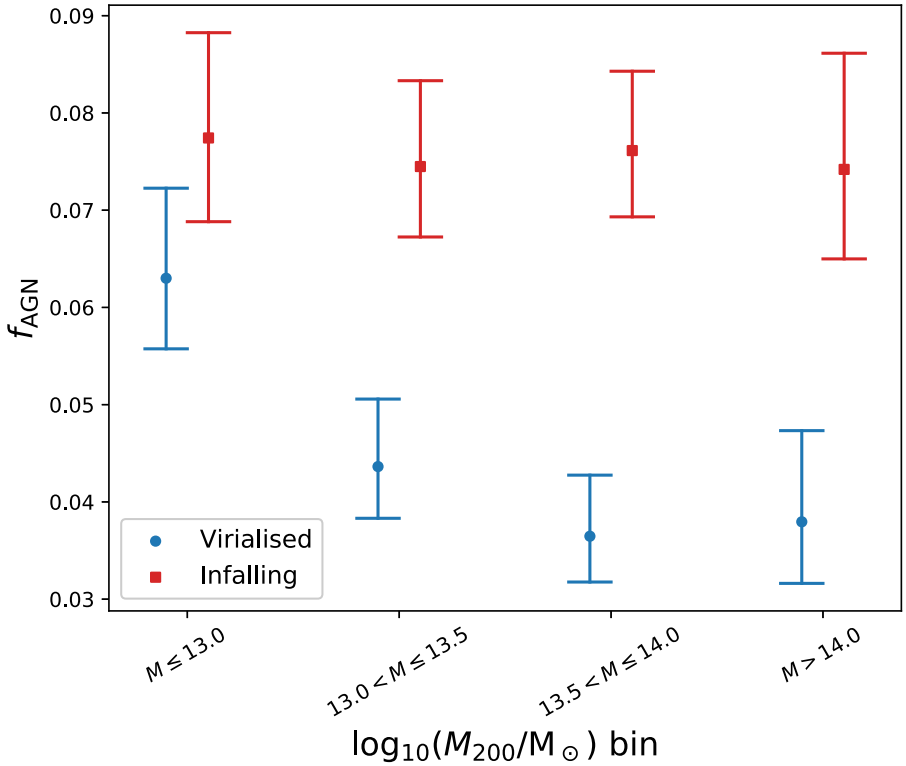

Figure 3.8: A comparison of the AGN fractions of the virialised and infalling galaxy populations defined by equation 3.10 (Oman et al., 2013). Blue circles show the virialised AGN fraction, which decreases with halo mass for $\log_{10}(M_{200}/\mathrm{M}_{\odot}) < 13.5$. The infalling AGN fraction is represented by red squares and is flat across all halo masses in our sample. As with Figure 3.5 a marginal x-axis offset is used for the two populations to improve clarity.

activity within galaxies (e.g., Sanders et al., 1988; Krongold et al., 2002; Ellison et al., 2011). This is supported by observations that both pairs and compact groups exhibit higher nuclear activity compared to field environments, with AGN fractions approaching $\sim$ 20 per cent in the closest pairs (Rubin et al., 1991; Menon, 1995; Ellison et al., 2011).

Pairs and compact groups represent the smallest super-galactic structures in the Universe. At the other end of the scale are massive clusters. In contrast to to smaller structures, clusters have AGN fractions of just $\sim$ 5 per cent (Martini et al., 2006; Arnold et al., 2009). This is lower than the field AGN fraction of 8 ± 0.13 per cent[2] (Woods & Geller, 2007). This could

[2]I have extrapolated the uncertainty on this value from Table 1 of Woods & Geller (2007).

suggest that the environmental changes associated with moving up the LSS mass function first act to increase AGN triggering opportunities through direct interaction, before inhibiting AGN triggering in high mass structures.

As a mid-point in the LSS mass function, galaxy groups should therefore sit between small structures such as pairs and compact groups, and clusters in terms of AGN fraction. Indeed prior observations have shown galaxy groups to have AGN fractions in the range $\sim 7-9$ per cent (Shen et al., 2007; Arnold et al., 2009; Oh et al., 2014; Tzanavaris et al., 2014). Our own observations are broadly consistent with this picture. We observe an AGN fraction of $6.01^{+0.29}_{-0.26}$ per cent, although we note that this covers the mass range of our group sample, i.e., $11.53 \leq \log_{10}(M_{200}/\mathrm{M}_{\odot}) \leq 14.56$. Consequently this may be driven by the high mass end of our group sample. Taking only the lowest quartile of the group mass range, the AGN fraction is $6.68^{+0.62}_{-0.53}$ per cent. This is perfectly consistent with the overall value observed in our sample, but is closer to the expected value from previous studies.

3.5.2 Galaxy location within group structure

As well as the galactic environment changing with group mass, the environmental conditions are a function of location within the group. Extending on the work of Haines et al. (2012) and Pimbblet et al. (2013), we have shown in Figure 3.5 that, although the radial AGN fraction of our groups decreases inside R_{200}, this effect is driven by high-mass groups. For low-mass groups, we show the AGN fraction out to $3.5R_{200}$ to be approximately flat. This suggests that the central regions of low-mass groups are similar to the more extended regions of those groups in terms of their ability to host AGN.

To conduct a more physically motivated analysis, we use the criteria of Oman et al. (2013) to split the groups into infalling and virialised populations. This shows that AGN are significantly ($\sim 3.9\sigma$) more likely to be found in infalling galaxies than virialised galaxies. As with the radial AGN fraction, this is primarily driven by the high mass groups in our sample. Figure 3.8 shows the infall AGN fraction remains flat at ~ 7.5 per cent across the mass range of our group sample, comparable to the field AGN fraction (Woods & Geller, 2007). This is suggestive that the act of falling into a group does not increase the likelihood of a galaxy hosting an AGN. The AGN fraction in the virialised region of the groups however,

is shown to decrease with increasing halo mass. This effect becomes significant at the 3.6σ level for groups with $M_{200} > 10^{13.5}\,M_{\odot}$, where only ~ 3.5 per cent of virialised galaxies host an AGN. That is to say, as one might expect, our high mass groups start to show the same observational properties with regard to AGN fostering that has been previously observed in clusters (Gilmour et al., 2007; Gavazzi et al., 2011; Haines et al., 2012; Pimbblet & Jensen, 2012; Pimbblet et al., 2013).

The decreasing AGN fraction in virialised galaxies with increasing group mass leads to the inference that the physics of the group core evolves with group mass. Indeed this should be expected if groups are simply low-mass and less evolved analogues of clusters. In relaxed clusters, the cores are virialised and consequently the frequency of low-speed interactions that may act as a trigger for AGN is reduced. As a group evolves into a cluster one would expect the dominance of this effect to increase, and consequently this mechanism may well play a role in the low virialised AGN fraction we see in our high-mass groups.

The inhibition of nuclear activity in the virialised region of phase-space of large groups may also be caused by RPS. The infall regions of clusters have been shown (Marshall et al., 2018) to provide the appropriate gas pressures to compress and destabilise intra-galactic gas (Schulz & Struck, 2001; Tonnesen & Bryan, 2009), potentially fuelling nuclear activity (Marshall et al., 2018). In the cores of clusters however, galaxies are subject to higher ram pressures that not only disrupt the internal galactic gas, but strip it from the galaxy (e.g., Kenney et al., 2004). Given that one would not expect the intense ram pressures required to strip a galaxy of gas in small groups, our observation of no AGN deficit in the central region of projected phase-space for low-mass groups is consistent with extreme RPS being a plausible mechanism for preventing nuclear activity in cluster cores.

The phase-space projections of galaxies within groups and clusters explain why the AGN fraction of the structure as a whole is lower than the AGN fraction in the field. If one considers only the infall region of the structure, the AGN fraction is shown to be a flat function of group halo mass (see red squares in Figure 3.8). Combining the AGN fraction in the infall region for all our groups to reduce the uncertainty gives an AGN fraction of ~ 7.5 per cent, and is consistent with the AGN fraction in the field (Woods & Geller, 2007). However, if one then

takes into account the core region of the cluster with its AGN deficit, this will act to reduce the overall AGN fraction. In low-mass groups where this effect is not observed, the infall AGN fraction is similar to the core AGN fraction, and thus similar to the field value.

3.5.3 A comparison to radio AGN, star-forming galaxies, and the passive population

The AGN used in this analysis have been selected optically, and hence their SMBH is accreting matter in a radiatively efficient manner. Such an accretion mode requires a cold gas fuel reservoir. In contrast, the SMBHs of radio selected AGN may inefficiently accrete matter whilst still powering the AGN. This inefficient accretion does not require a supply of cold gas, and the black hole may be 'drip-fed' by either internal or external mechanisms (Hardcastle et al., 2007; Best & Heckman, 2012; Ellison et al., 2015). Consequently the environmental effects inhibiting optical AGN in the cores of massive structures may not inhibit radio AGN. Indeed, the majority of low-powered radio AGN are found in the central galaxies in groups and clusters (Best et al., 2007; Ching et al., 2017). Therefore, these observations can only be used draw conclusions about the efficiently accreting AGN population.

Star forming galaxies, like optically selected AGN, require a fuel supply of cold gas. At the centres of massive groups, should that gas have been stripped on infall, and the IGM be too hot to accrete cold gas, then this will lead to the strangulation of star formation as well as reducing the AGN fraction in the group centre. Indeed, this effect is seen in massive clusters (Lopes et al., 2017). Additionally, Barsanti et al. (2018) observe this effect with the fraction of star forming galaxies increasing in groups with R/R_{200}. Although their halo mass bins are larger than ours, their group sample shows a higher fraction of star forming galaxies at small projected radii than their cluster sample (see Fig. 5 of Barsanti et al., 2018).This is consistent with what might be expected based on our demonstration of the importance of halo mass for galaxy nuclear activity. Furthermore, both Lopes et al. (2017) and Barsanti et al. (2018) observe the opposite effect for passive galaxies, with the passive population being more centrally located. As would be expected based on our observations, this effect is stronger in clusters than groups.

3.5.4 Accounting for potential sources of bias

Stellar mass

The likelihood of a galaxy hosting an AGN increases with stellar mass (Pimbblet & Jensen, 2012; Pimbblet et al., 2013; Wang et al., 2017; Lopes et al., 2017). Given that the central galaxies in groups are the most massive, the deficit of AGN in the cores of massive groups and clusters is unlikely to be a stellar mass bias. Moreover, if a dominant stellar mass bias were at play, one would expect to see the opposite observation. However, in low mass groups AGN are observed in the virialised region as frequently as in the infalling population. It is therefore necessary to confirm that the stellar mass distribution of galaxies within our group sample is not dependent in halo mass. In Figure 3.9 we show the median stellar mass of galaxies within the same halo mass bins used in Figure 3.8, demonstrating there is no difference in the stellar mass distributions of our high and low mass groups.

Group selection

We have taken care throughout this work to ensure that bias from group selection effects is minimal in our results. Nonetheless, as with any observational work, one must consider whether such effects may drive a result. FoF algorithms are reliable but may under select from the extended group structure (Barsanti et al., 2018), whereas methods such as ours that select based on a radius and velocity are prone to contamination from field galaxies. That is to say, such methods prioritise completeness over fidelity (Rines et al., 2005; Oman & Hudson, 2016).

In this work, to reduce the contamination of the group sample by interloping field galaxies, we exclude from selection galaxies that fall outside the NFW infall radius predicted for a group (see Section 3.3.2). However, by taking this approach there is every chance of excluding high-velocity infalling galaxies that genuinely are part of the group. To test whether this affected our results we reran the analysis on a group selection that did not account for the NFW profile. That is to say group membership was simply defined as $R < 3.5R_{200}$; $|\Delta v| < 3.5\sigma_{\rm group}$. This had no significant effect on our results with high mass groups having a central AGN deficit at $\sim 4\sigma$ confidence.

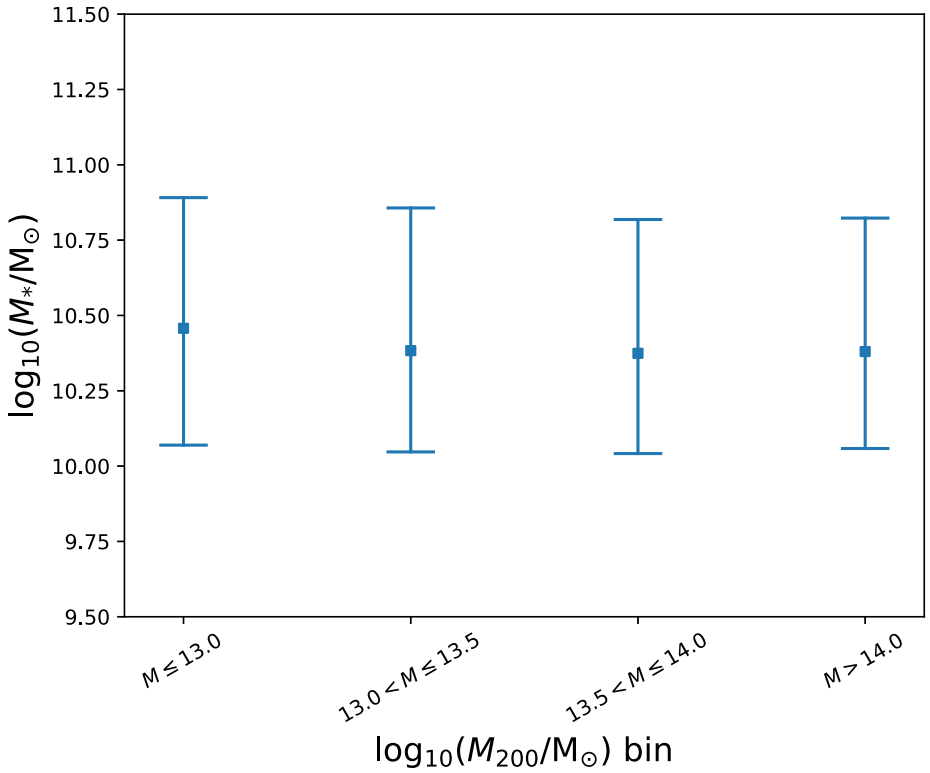

Figure 3.9: The median stellar mass of galaxies with $\log_{10}(M_*/\mathrm{M}_\odot) > 9.9$ with group halo mass. Across the halo mass range of our sample there is no variation in the median galactic stellar mass, eliminating this as a potential source of bias for our observations. The error bars represent the 16th and 84th percentiles of the stellar mass distribution in each halo mass bin, and thus represent 68 per cent of the population.

To select our group members using the method described Chapter 3.3.2, the centre of the group was chosen to be the galaxy that was central galaxy in corresponding FoF group (see Section 4.2 of Robotham et al., 2011). The logical alternative to this would be to centre the group selection on the brightest group galaxy (BGG). In 95 per cent of cases for groups with $N_{\mathrm{FoF}} \geq 5$, as we require for our group selection, the BGG was also the central galaxy in the group. Given this substantial overlap, we would expect altering the group selection in this way to have little effect on our results. To be certain of this, we reselected our groups using the BGG as the group centre. This resulted in a sample of 7482 galaxies with $\log_{10}(M_*/\mathrm{M}_\odot) > 9.9$, of which 452 host an AGN. Redoing our analysis on this sample produced the same results as for the group selection centred on the central galaxy of the corresponding FoF group.

Of final note on the group selection, is the calculation of the halo masses, M_{200}. As described in Section 3.3.2, we calculate our halo masses using the scaling relation of Munari et al. (2013, see equation 3.2), and thus $M_{200} \propto \sigma^3$ as would be expected from the virial theorem. Observations using weak gravitational lensing support a scaling relation with a shallower slope, $M_{200} \propto \sigma^{\sim 2}$ (Han et al., 2015; Viola et al., 2015). This weaker dependency however may not be accurate at the lower halo masses explored in this work. Viola et al. (2015) note that their selection criteria may result in an overestimate of the halo mass for groups with low-velocity, and thus reduce the exponent of the relation. Given this potential bias in the low-mass regime from weak-lensing derived observations, it is prudent for us to use a scaling relation consistent with the virial theorem.

The infalling population

Additionally, one must question whether our definition of the infalling and virialised populations may bias our results. We chose to use a physically motivated definition based on the work of Oman et al. (2013). This was based on N-body simulations and the result extrapolated into the projected phase-space plane. An independent test would be to compare our results directly with prior observations, and indeed our radial AGN fractions binned by group halo mass (see Figure 3.5) support our conclusions in this regard.

Further support of our results is obtained when we compare directly to Haines et al. (2012) who found no AGN within $0.4R/R_{500}$, and $0.8|\Delta v|/\sigma$ of the cluster centre. Transposing these criteria onto our projected phase-space plane defines a region $R < 0.26R_{200}$; $|\Delta v| < 0.8\sigma_{\rm group}$. When comparing the fraction of AGN inside this region to that outside we find that at $M_{200} > 10^{13.5}\,{\rm M}_{\odot}$ there is a deficit of AGN in this central region at the 2.5σ level. As with our other results, lower group masses do not show this effect.

3.6 Conclusions

We have exploited the depth and spectroscopic completeness, 98 per cent at $r < 19.8$ mag, of the GAMA survey (Driver et al., 2011; Liske et al., 2015) to probe the halo mass function in order to test the affect of group environment on AGN. We investigated the effect of galaxy

position, both radially and within projected phase-space on AGN prevalence. Further to this, by binning our group sample by halo mass, we demonstrate the evolution of a preferential region for AGN fostering within the group projected phase-space. Our main findings are as follows.

i The AGN fraction within our group sample is $6.01^{+0.29}_{-0.26}$ per cent, marginally lower than previous studies have found in groups. We attribute this to the large mass range covered by our sample. Although when split by halo mass the group AGN fraction is approximately flat, for the 25 percent of our galaxies in the lowest mass groups, $M_{200} < 10^{13.06}\,\mathrm{M}_{\odot}$, the AGN fraction is $6.68^{+0.62}_{-0.53}$ per cent. This is consistent with prior observations of the group AGN fraction (Shen et al., 2007; Arnold et al., 2009; Oh et al., 2014; Tzanavaris et al., 2014).

ii We find the AGN fraction as a function of projected separation is flat for low-mass groups. For high mass groups however, the AGN fraction is noticeably reduced at $R < R_{200}$, consistent with the findings of Ehlert et al. (2013); Pimbblet et al. (2013) for clusters.

iii Using the projected phase-space to split the galaxies into virialised and infalling populations as per Oman et al. (2013, see equation 3.10), we show that low mass groups do not experience the same deficit of AGN in their cores as do high mass groups and clusters (Gilmour et al., 2007; Gavazzi et al., 2011; Haines et al., 2012).

iv Across the halo mass range of our group sample, the infalling AGN fraction is comparable to the field AGN fraction, indicating that there is no excess of AGN triggering on infall in to groups.

v We demonstrate the evolution of group cores from an environment that supports AGN at low halo masses, to one which inhibits nuclear activity at halo masses greater than $10^{13.5}\,\mathrm{M}_{\odot}$ (see Figure 3.8).

3.7 Acknowledgements

The authors take this opportunity to thank the anonymous referee for their constructive comments. YAG acknowledges the financial support of the University of Hull through an internally funded PhD studentship that has enabled this research to be undertaken. KAP acknowledge the support of STFC, through the University of Hull?s Consolidated Grant ST/R000840/1. MSO acknowledges the funding support from the Australian Research Council through a Future Fellowship (FT140100255).

GAMA is a joint European-Australasian project based around a spectroscopic campaign using the Anglo-Australian Telescope. The GAMA input catalogue is based on data taken from the Sloan Digital Sky Survey and the UKIRT Infrared Deep Sky Survey. Complementary imaging of the GAMA regions is being obtained by a number of independent survey programmes including GALEX MIS, VST KiDS, VISTA VIKING, WISE, Herschel-ATLAS, GMRT and ASKAP providing UV to radio coverage. GAMA is funded by the STFC (UK), the ARC (Australia), the AAO, and the participating institutions. The GAMA website is http://www.gama-survey.org/.

Funding for SDSS-III has been provided by the Alfred P. Sloan Foundation, the Participating Institutions, the National Science Foundation, and the U.S. Department of Energy Office of Science. The SDSS-III web site is http://www.sdss3.org/.

SDSS-III is managed by the Astrophysical Research Consortium for the Participating Institutions of the SDSS-III Collaboration including the University of Arizona, the Brazilian Participation Group, Brookhaven National Laboratory, Carnegie Mellon University, University of Florida, the French Participation Group, the German Participation Group, Harvard University, the Instituto de Astrofisica de Canarias, the Michigan State/Notre Dame/JINA Participation Group, Johns Hopkins University, Lawrence Berkeley National Laboratory, Max Planck Institute for Astrophysics, Max Planck Institute for Extraterrestrial Physics, New Mexico State University, New York University, Ohio State University, Pennsylvania State University, University of Portsmouth, Princeton University, the Spanish Participation Group, University of Tokyo, University of Utah, Vanderbilt University, University of Virginia, University of Washington, and Yale University.

This research made use of Astropy, a community-developed core Python package for Astronomy (Astropy Collaboration, 2013).

4. The Fuelling of Low-Excitation Radio Galaxies

"There is nothing like looking, if you want to find something"

– J.R.R. Tolkein, *The Hobbit (1937)*

4.1 Prologue

One of the key open questions in extragalactic astronomy is that of the triggering mechanisms of AGN. For efficiently accreting AGN, high-impact external triggers such as major-mergers, harassment, and RPS are often invoked (e.g., Moore et al., 1996; Ellison et al., 2011; Marshall et al., 2018). Conversely, the inefficiently accreting population of LERGs (low-excitation radio galaxies) are thought to be drip fed from a poor supply of cold gas (Hardcastle et al., 2007), and observations have shown major-mergers to be an unlikely cause of the LERG phenomenon (Ellison et al., 2015). Thus, if LERGs are triggered by mergers, then it is minor mergers, i.e., mergers between galaxies with a mass ratio $\gtrsim 4:1$ (Lotz et al., 2010), that provide the fuel supply. The following chapter presents a test of the hypothesis that minor-mergers trigger LERGs. This is achieved by an analysis of the frequency of low surface brightness tidal features (e.g. as per Kaviraj, 2014a) in LERGs relative to a control sample.

This work forms the basis of a paper I am leading that is in preparation. I am responsible for > 95 per cent of the workload, with my collaborators, Kevin Pimbblet, Matt Owers, and Sugata Kaviraj, providing scientific feedback on my analysis and writing.

4.2 Introduction

The accretion of matter onto the central supermassive black hole in galaxies powers active galactic nuclei (AGN). Should the rate of accretion, $\dot{M}$, be of the order 1 per cent of the Eddington accretion rate, $\dot{M}_{\rm Edd}$, or greater, then the accretion mode can be described as efficient (Hardcastle et al., 2007; Maraschi et al., 2012). In such radiatively efficient accretion, the accretion flow is optically thick and produces high energy photons which act to ionise the

surrounding interstellar medium (Urry & Padovani, 1995). This leads to the narrow emission lines, e.g., [O III] λ5007, seen in Seyfert galaxies.

The dominant population of radio loud AGN (RLAGN) in the local Universe do not show such evidence of ionisation (Best & Heckman, 2012), and are known as LERGs. This is suggestive of a very low accretion rate, i.e., $\dot{M} \ll 0.01\dot{M}_{\rm Edd}$ (Baum et al., 1995; Tadhunter et al., 1998; Mingo et al., 2014). In such radiatively inefficient accretion models the bulk of the energy accreted powers the radio jet, thus providing evidence of an AGN in the absence of ionisation lines or X-rays (Allen et al., 2006; Hardcastle et al., 2007).

The weakly accreting nature of LERGs is indicative of poorer fuel supply than is available in more efficiently accreting AGN (Best & Heckman, 2012). LERGs are generally passive in terms of star-formation, and are associated with red, massive, early type galaxies (Best et al., 2005b; Kauffmann et al., 2008). This lack of star-formation adds weight to the argument that a ready supply of cold gas is not necessary to fuel LERGs. Furthermore, LERGs are frequently found in over-dense environments, and often in brightest cluster galaxies, where the hot intra-cluster medium inhibits cold-mode accretion (Hill & Lilly, 1991; Best et al., 2007; Davies et al., 2017). Consequently, mechanisms such as minor-mergers and hot-mode accretion are invoked as potential triggers for LERGs (Hardcastle et al., 2007; Ellison et al., 2015; Pracy et al., 2016).

Testing whether or not minor-mergers are the dominant trigger mechanism for LERGs can be problematic. The high mass ratio between the two merging galaxies mean that the structure of the smaller galaxy is completely disrupted and absorbed by the more massive galaxy. The effect on the morphology of the major galaxy in a minor-merger can, however, be negligible. Consequently, the only direct evidence of a recent minor-merger history for a massive galaxy will present as low surface brightness (LSB) tidal remnants of the smaller galaxy (Kaviraj, 2014a,b). Moreover, in order for the minor merger to be detected, the tidal remnant must remain visible during the time required for the accreted gas to fall to nucleus of the primary galaxy, a process expected to take $\sim$ 400 Myr (Shabala et al., 2017).

Detecting LSB tidal features requires deeper imaging than is necessary for normal morphological studies of massive galaxies. A new range of wide-deep imaging surveys, such as

stripe 82 of the Sloan Digital Sky Survey (SDSS, York et al., 2000; Abazajian et al., 2009), the Dark Energy Camera Legacy Survey (DECaLS)[1], and the Kilo Degree Survey (KiDS, de Jong et al., 2013) are opening up a pathway to large studies of LSB morphologies. Should minor-mergers be the dominant trigger mechanism for LERGs, then one would expect an excess of LSB tidal features in this population relative to otherwise similar galaxies (Kaviraj, 2014a,b), a hypothesis that is the foundation of this letter.

The layout of this letter is as follows. In Chapter 4.3, we detail the data used in this paper from SDSS and DECaLS. We state and discuss our observations in Chapter 4.4. Chapter 4.5 is a summary of this work. Throughout this letter we assume a standard flat ΛCDM cosmology with $h = 0.7$, $H_0 = 100h\,\mathrm{km\,s^{-1}\,Mpc^{-1}}$, $\Omega_\mathrm{M} = 0.3$, $\Omega_\Lambda = 0.7$.

4.3 Data

The spectroscopic data used in this work is obtained from data release 7 (DR7, Abazajian et al., 2009) of SDSS, which contains spectra for $\sim 10^6$ galaxies and quasars across $\sim 8\,000\,\mathrm{deg^2}$ of the sky. Specifically, we make use of the stellar mass estimates from MPA/JHU value added catalogue[2], and morphological classifications from the Galaxy Zoo database (Lintott et al., 2011). In order to obtain a sample with reliable morphological classification and imaging deep enough to detect the LSB tidal remnants of minor mergers, we limit this study to $z < 0.07$.

4.3.1 DECaLS imaging

Previous analyses of LSB tidal features similar to that presented in this Chapter have made use of Stripe 82 of SDSS. This is due to it's deeper imaging ($r \lesssim 25\,\mathrm{mag}$) relative to what is available from the SDSS main imaging catalogue ($r < 22.2\,\mathrm{mag}$, Kaviraj, 2014a,b). The added depth of Stripe 82 results in images that can detect surface brightness down to $\mu_r < 28.5\,\mathrm{mag\,arcsec^{-2}}$ (Fliri & Trujillo, 2016). Stripe 82 is, however, limited in its footprint, covering $300\,\mathrm{deg^2}$. Whilst only having a point source depth of $r < 23.9\,\mathrm{mag}$[3] (~ 1 mag lower

[1] http://legacysurvey.org/decamls/

[2] https://wwwmpa.mpa-garching.mpg.de/SDSS/DR7/

[3] Although not stated in the literature, the flux values of the tidal features seen in Figure 4.9 suggest that DECaLS can observe surface brightnesses of $\mu_r > 27\,\mathrm{mag\,arcsec^{-2}}$.

than stripe 82 but 1.7 mag higher than the main SDSS imaging survey), data release 5 (DR5) of DECaLS covers $\sim 8\,000\,\mathrm{deg}^2$ in the range $-20° < \delta < +30°$. This > 25 fold increase in available footprint motivates DECaLS as the choice of imaging survey for this work.

One issue that is present in the DECaLS DR5 data is that of missing fields. This is the result of using GAIA data release 1 stars being used as zeropoints. Gaia has missing areas in its coverage and the result is that some DECaLS observed bricks are uncalibrated and hence not included in the data release. Consequently galaxies in these regions are not used in this work.

4.3.2 LERG selection

We select our LERGs from the Best & Heckman (2012) catalogue of 18286 radio galaxies in SDSS. This catalogue was the result of cross matching observations from SDSS, the National Radio Astronomy Observatory (NRAO) Very Large Array (VLA) Sky Survey (NVSS, Condon et al., 1998), and the VLA Faint Images of the Radio Sky at Twenty cm survey (FIRST, Becker et al., 1995; Best et al., 2005a; Best & Heckman, 2012). The method used to classify LERGs is detailed in full in (Best & Heckman, 2012), but a brief overview is presented here.

The difficulty in segregating star-formation or nuclear activity as the source of radio emission is dealt with by a multi-fold approach. Best & Heckman (2012, see especially their Appendix 1) classify the radio galaxies as AGN or star-forming based on three criteria (where possible) before combining these into a single classification. Explicitly, the three parameters used are: the position of the galaxy on the D_{4000} versus $L_{1.4\,\mathrm{GHz}}/M_*$ plane (Best et al., 2005a; Best & Heckman, 2012, Figure 4.1); the Kauffmann et al. (2003) criteria on a Baldwin-Philips-Terlavich diagram (Baldwin et al., 1981, Figure 4.2), and Hα to radio luminosity of the galaxy (Kauffmann et al., 2008, Figure 4.3).

For the RLAGN sample, (Best & Heckman, 2012) classify galaxies as high- or low-excitation based on emission line diagnostics of decreasing complexity, depending on the number lines observed and spectral quality. For the highest quality spectra, and where Hβ, [O III] $\lambda\lambda$4959, 5007, [O I] $\lambda\lambda$6300, 6364, Hα, [N II] $\lambda\lambda$6548, 6584, and [S II] $\lambda\lambda$6716, 6731 are all observed, the excitation index of Buttiglione et al. (2010) is used. At the the other extreme, for spectra where multiple lines are not observed, a more simple detection threshold

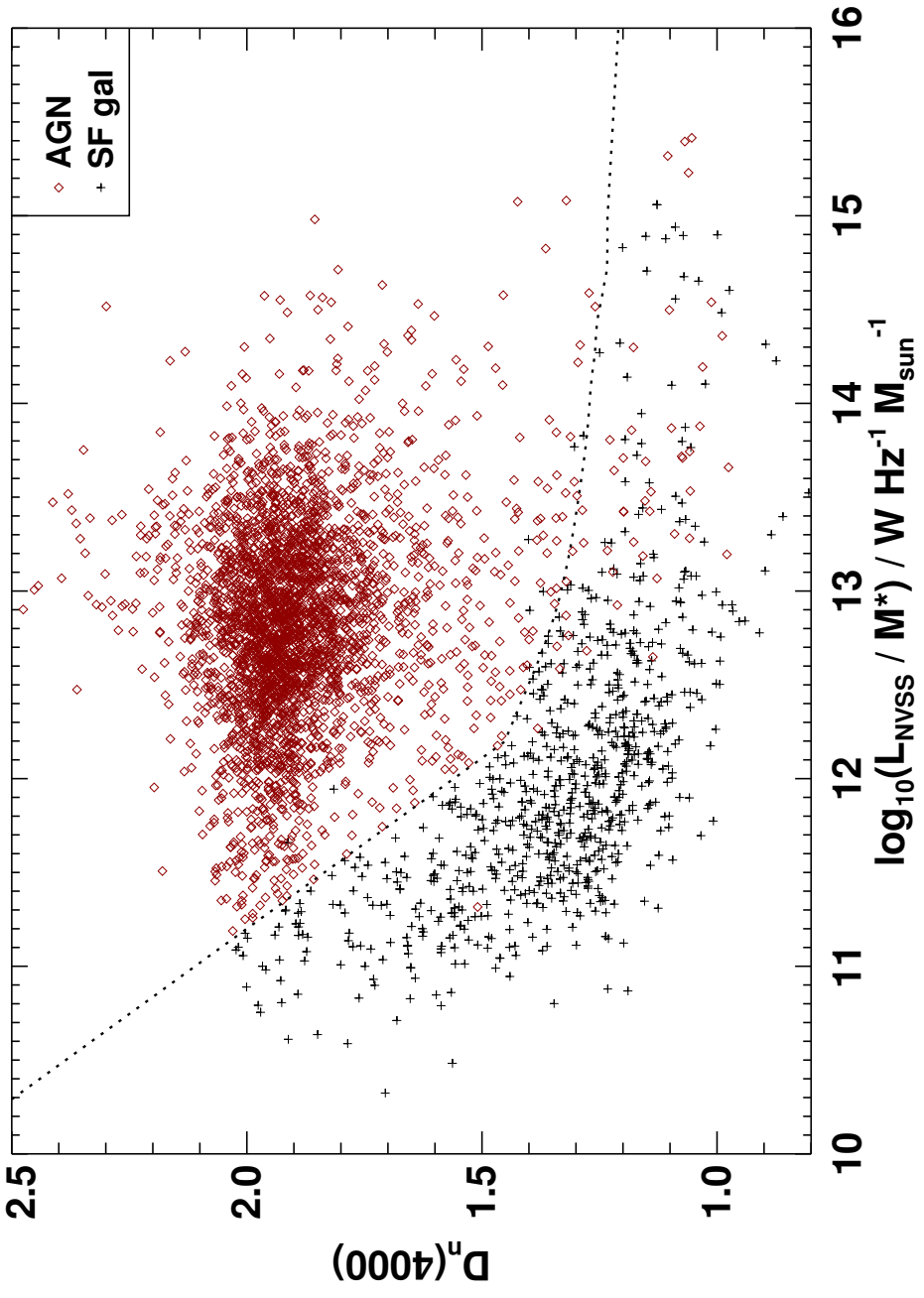

Figure 4.1: The Best & Heckman (2012) segregation of radio galaxies into star-forming galaxies and AGN using the $L_{1.4\,\mathrm{GHz}}/M_*$ versus D4000 plane. The red diamonds represent Best & Heckman (2012) RLAGN, whilst the black crosses represent star-forming galaxies. Originally a panel in Fig. A1 of Best & Heckman (2012).

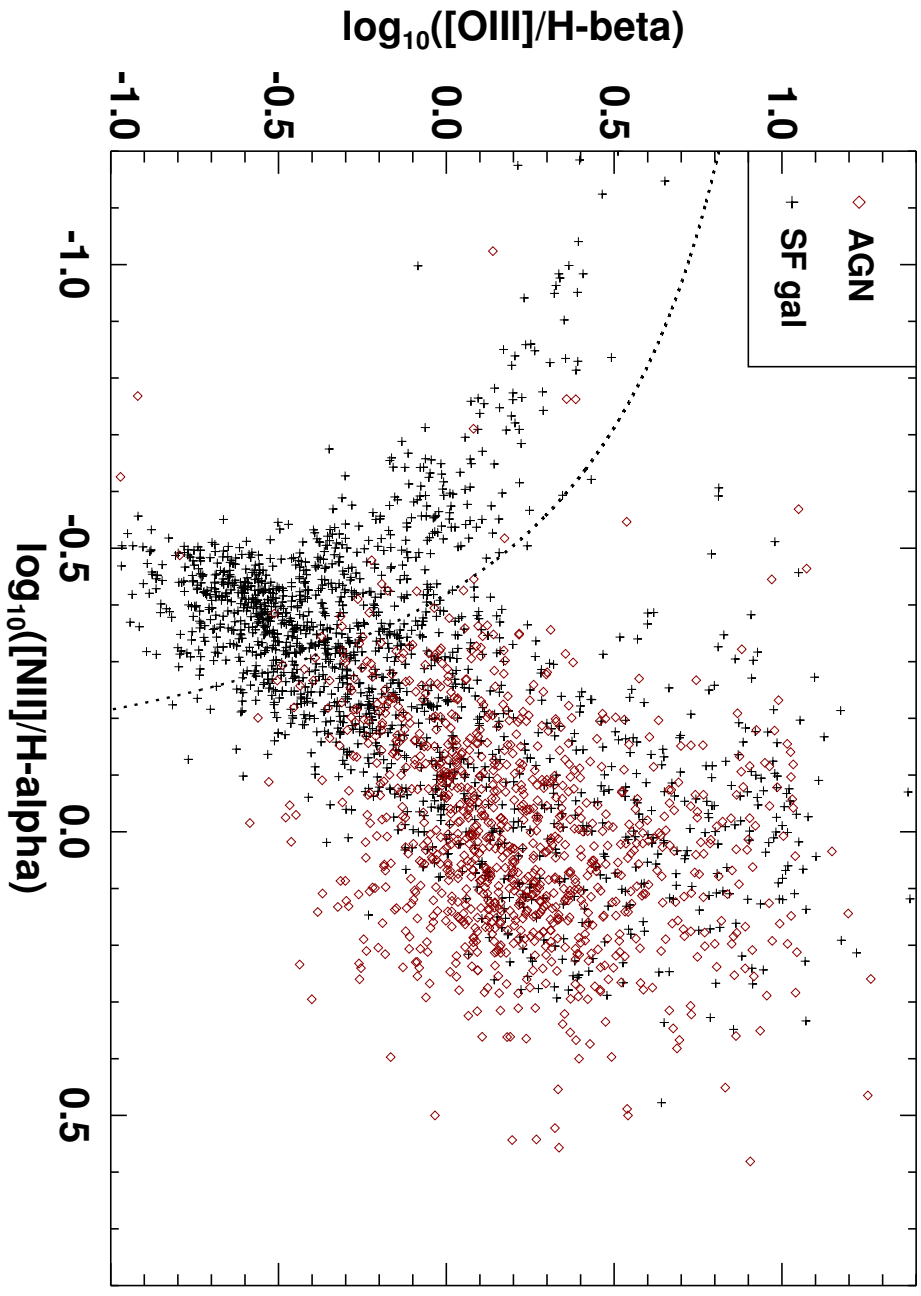

Figure 4.2: The Best & Heckman (2012) segregation of radio galaxies into star-forming galaxies and AGN using a BPT diagram. The red diamonds represent Best & Heckman (2012) RLAGN, whilst the black crosses represent star-forming galaxies. Originally a panel in Fig. A1 of Best & Heckman (2012).

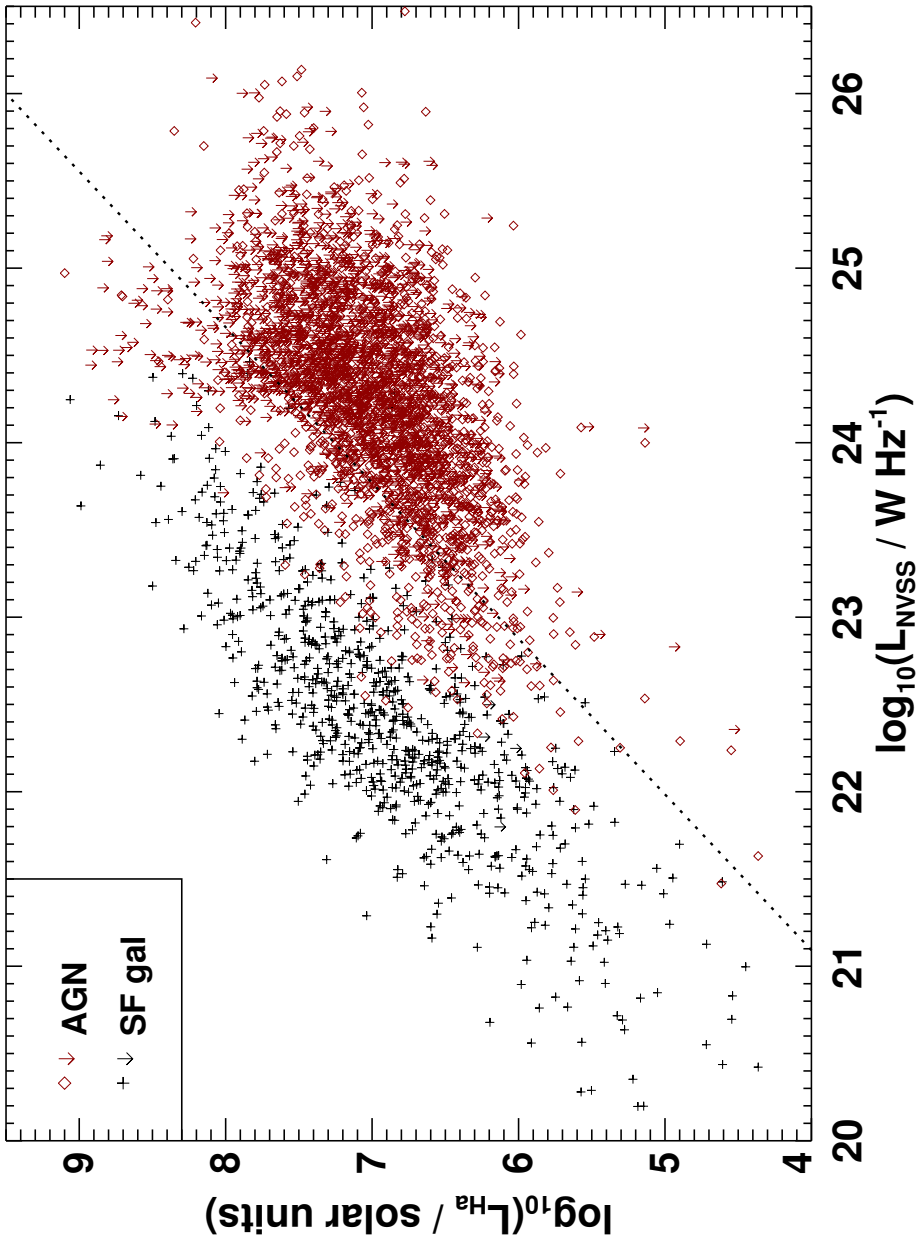

Figure 4.3: The Best & Heckman (2012) segregation of radio galaxies into star-forming galaxies and AGN using the $L_{1.4\,\mathrm{GHz}}$ versus $L_{\mathrm{H}\alpha}$ plane. as with Figures 4.1 and 4.2, the red diamonds represent Best & Heckman (2012) RLAGN, whilst the black crosses represent star-forming galaxies. Arrows are used when only an upper limit on on$L_{\mathrm{H}\alpha}$ could be obtained. Originally a panel in Fig. A1 of Best & Heckman (2012).

of $EW_{[O\,III]\ \lambda5007} = 5$ Å is used to segregate high- and low-excitation radio galaxies.

Stellar masses for our LERGs are taken as the mean values from the MPA/JHU value added catalogue. Morphology is taken from GalaxyZoo (Lintott et al., 2011), and require that at least 80 per cent of the debiased voting is supportive of the morphological classification. Galaxies with an uncertain debiased morphology are removed from our sample. Environment is defined as being field, group, or cluster based on the halo mass from the the Yang et al. (2007) SDSS group catalogue for DR7. Explicitly,

- $\log_{10}(M_{180}/\mathrm{M}_\odot) < 12.5$ is defined as the field
- $12.5 \leq \log_{10}(M_{180}/\mathrm{M}_\odot) < 14.0$ is defined as group
- $\log_{10}(M_{180}/\mathrm{M}_\odot) \geq 14.0$ is a cluster environment (e.g., Gordon et al., 2018; Barsanti et al., 2018).

4.3.3 Control sample

To select a control sample, for each LERG we select a population of radio-quiet galaxies that are otherwise similar to the LERG in terms of redshift, stellar mass, morphology, and environment. To match on redshift we require that $z_{\mathrm{control}} = z_{\mathrm{LERG}} \pm < 0.01$. For our stellar mass matching, we require that the stellar mass of the control is within the 1σ error of the stellar mass estimate of the LERG. Should a LERG be located in the field, then we require that the control galaxies for that LERG also be located in the field. However, should the LERG be located within a group or cluster, then the control galaxies are required to be located in a similar mass structure. Specifically, the difference in halo masses of the structures containing the LERG and its control galaxies is less than 0.25 dex. Finally, we require that the debiased GalaxyZoo morphological classification of the control galaxies match that of the LERG.

Applying these parameters for each LERG, the two closest control galaxies to the LERG in stellar mass are added to the control sample. In order to prevent duplicate galaxies appearing in the control sample, should a galaxy already have been picked as a control galaxy for a LERG then it is removed from consideration when selecting the control galaxies for further LERGs. For six LERGs, only one control galaxy could be found with reliable image data rather than

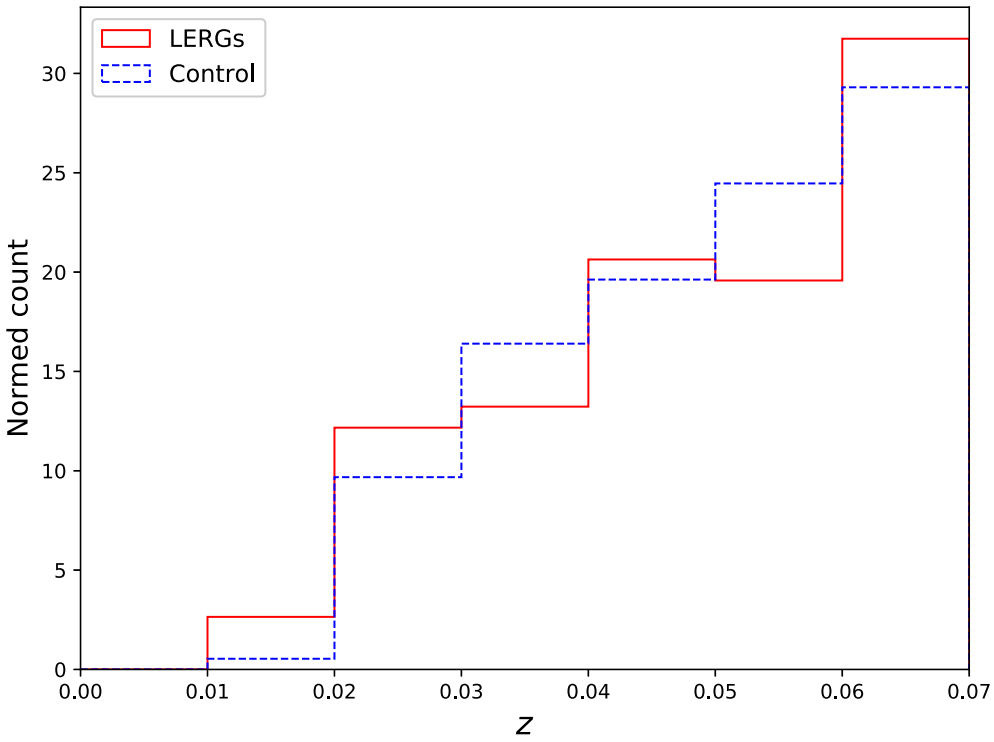

Figure 4.4: The distributions of the redshift of the LERG (red solid line) and control (blue dashed line) samples. A two sample KS test performed on these distributions returns a p-value of 0.75.

two. This selection leaves us with a sample of 189 LERGs and 372 control galaxies. To test the validity of our control population we compare the control and LERG distributions for redshift (Figure 4.4), stellar mass (Figure 4.5) and, for non-field galaxies, the group or cluster halo mass (Figure 4.6). For each of these distributions two-sample Kolmogorov-Smirnov (KS) tests are performed and returned p-values of 0.75, 0.99, and 0.96 for z, M_* and M_{180} respectively. This is strongly suggestive that the control population is representative of the LERG population.

4.4 Observations and Discussion

4.4.1 Fraction of LERGs and controls with tidal features

For each of the LERGs and control galaxies, an r-band FITS cutout measuring 200×200 kpc at the redshift of the target galaxy was used. These were visually inspected and scored based

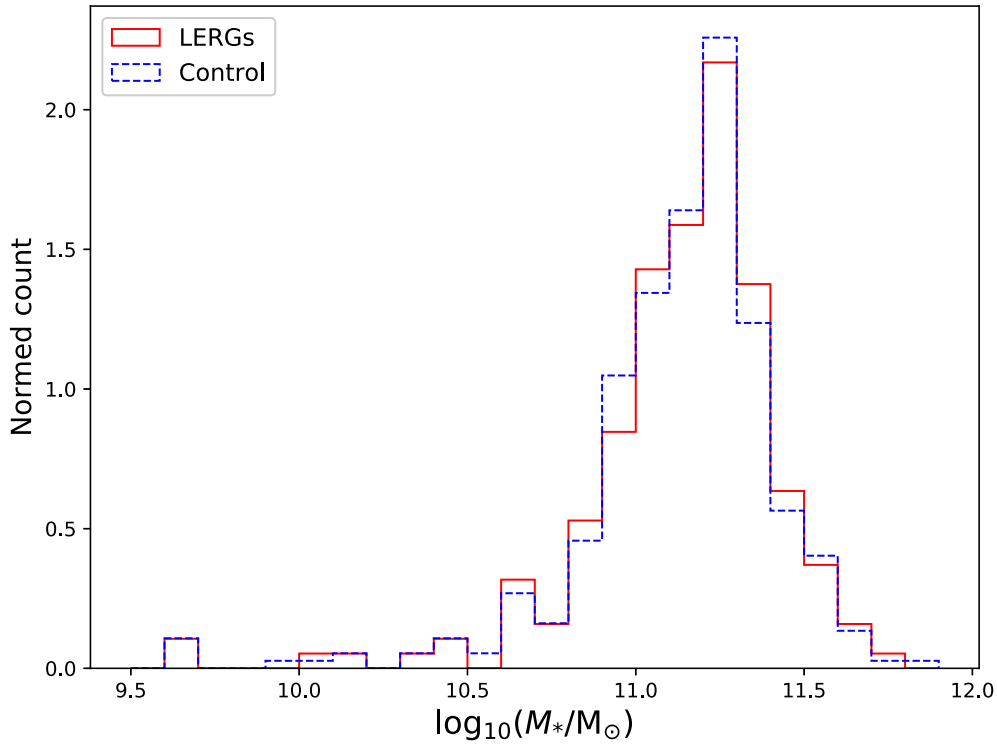

Figure 4.5: The distributions of the stellar masses of the LERG (red solid line) and control (blue dashed line) samples. A two sample KS test performed on these distributions returns a p-value of 0.99.

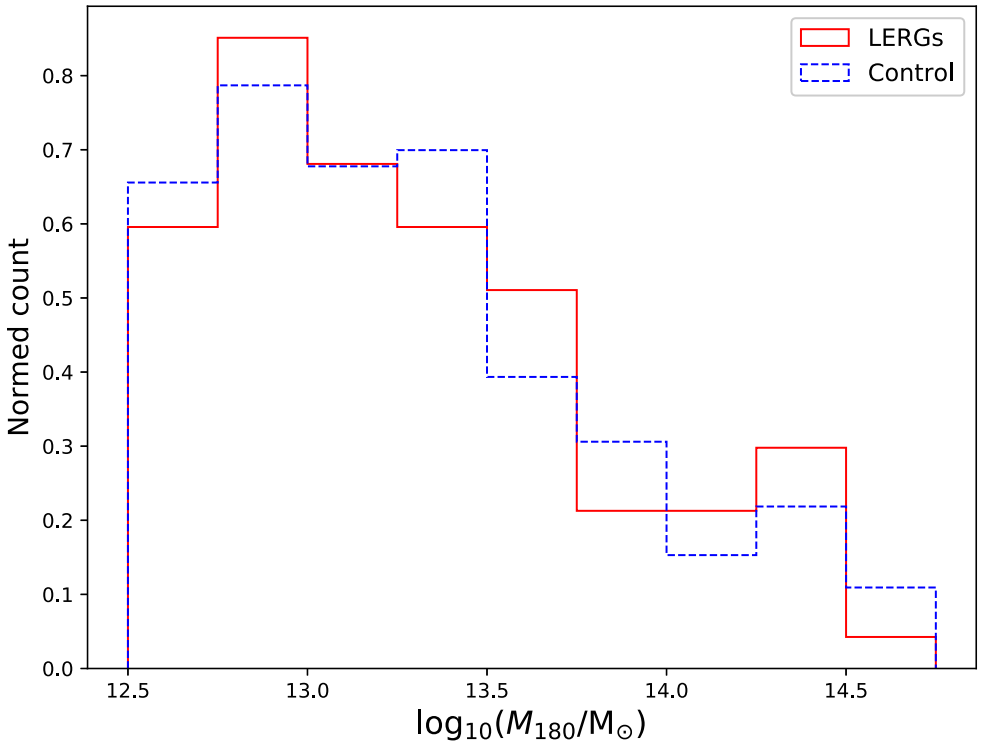

Figure 4.6: The distributions of the group halo masses of the LERG and control samples. As in Figures 4.4 and 4.5 the red solid line represents LERGs and the blue dashed line represents the control population. A two sample KS test performed on these distributions returns a p-value of 0.96.

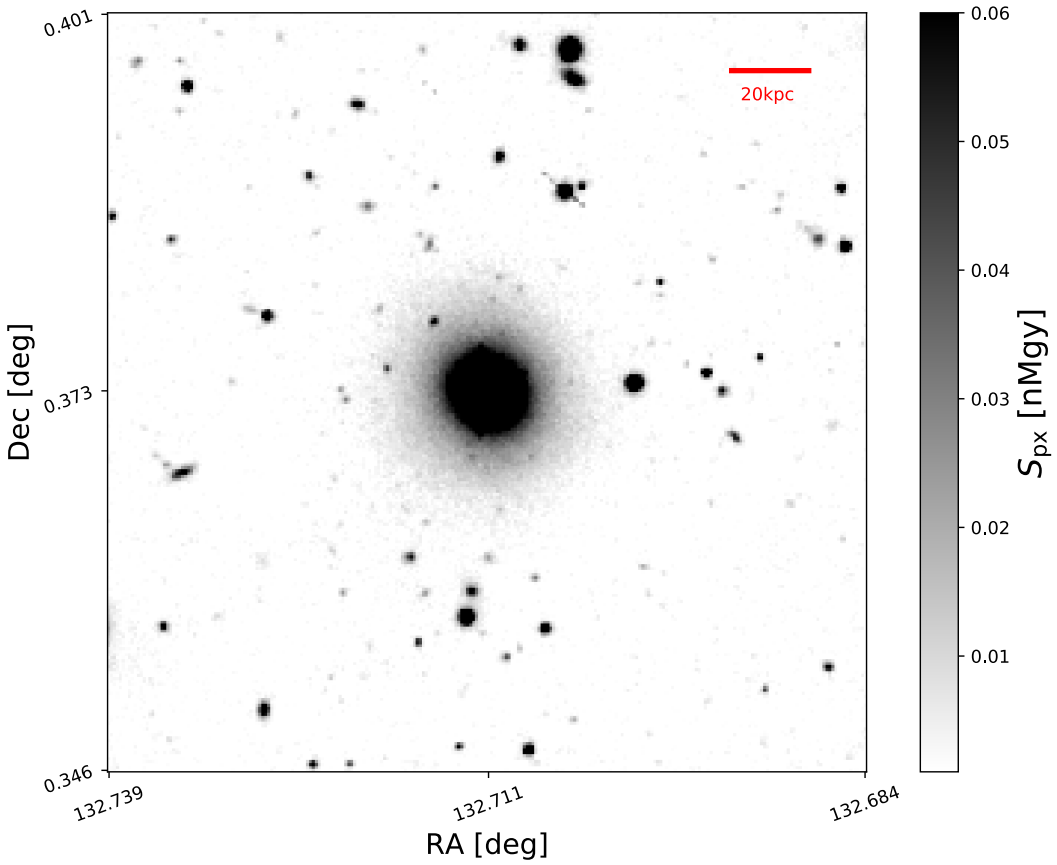

Figure 4.7: Example DECaLS image showing a galaxy without evidence of recent minor-mergers, i.e., was given a score of 0 in our analysis. For reference the colour bar shows the pixel flux value in nanomaggies.

on their appearance. A score of 1 was allocated should LSB tidal features be present, if the galaxy had a relaxed morphology, then a score of 0 was allocated. Clear examples of major interactions were not counted. Example images with scores of 0 and 1 are shown in Figures 4.7 - 4.8. The minor-merger fraction was then calculated as $N_{\text{score}==1}/N$. For perspective, Figures 4.9 and 4.10 demonstrate the improvement of DECaLS over SDSS r-band images.

For the complete sample of LERGs, the minor merger fraction was found to be $27.0^{+3.5}_{-3.0}$ per cent, compared to $31.5^{+2.5}_{-2.3}$ per cent for the control sample. These errors are binomial, and assume a beta distribution (Cameron, 2011). We further test whether the minor-merger history of a galaxy influences the radio-luminosity of the AGN. This is achieved by looking at the fractions of LERGs in different regions of their radio-luminosity distribution with LSB tidal features. Specifically we look at the lower and upper quartiles, and the inter quartile range of the radio luminosity distribution, which spans the range $21.73 < \log_{10}\left(\frac{L_{1.4\,\text{GHz}}}{\text{W Hz}^{-1}}\right) < 25.21$ (see

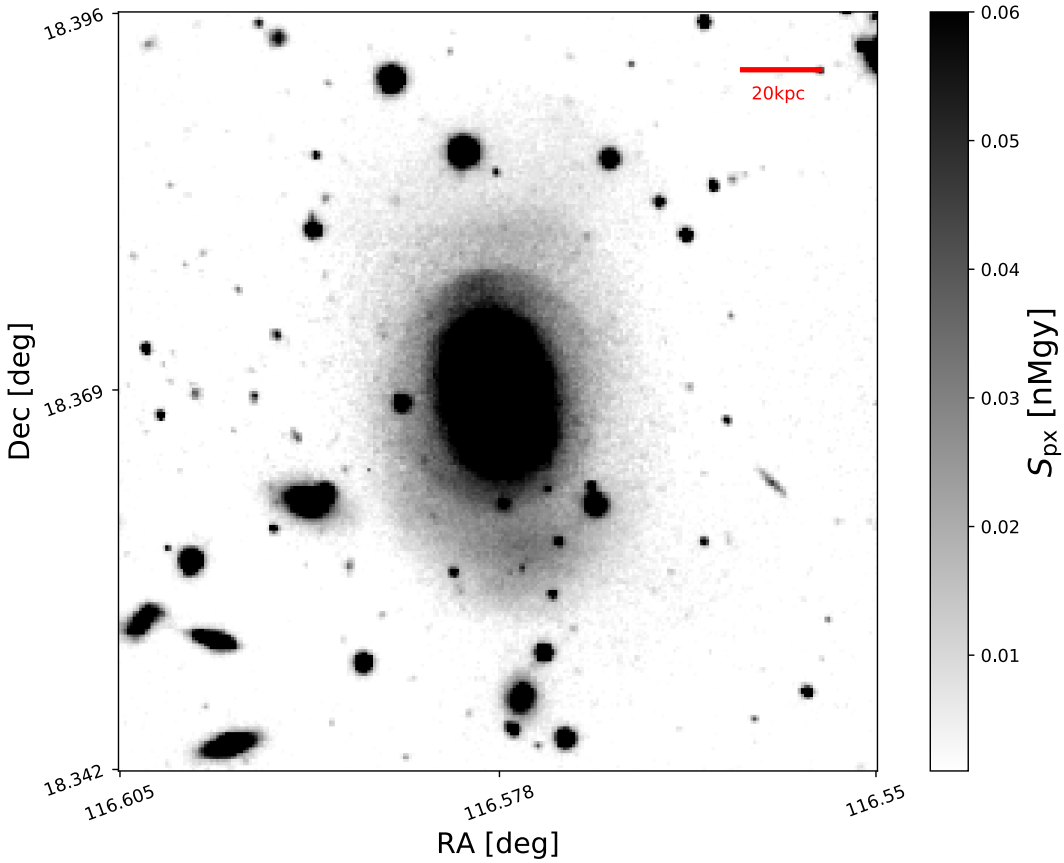

Figure 4.8: Example DECaLS image showing a galaxy with obvious and multiple LSB shell structures in the galactic halo and hence given a score of 1 in our analysis. This shows clearly that this galaxy has undergone recent minor-mergers.

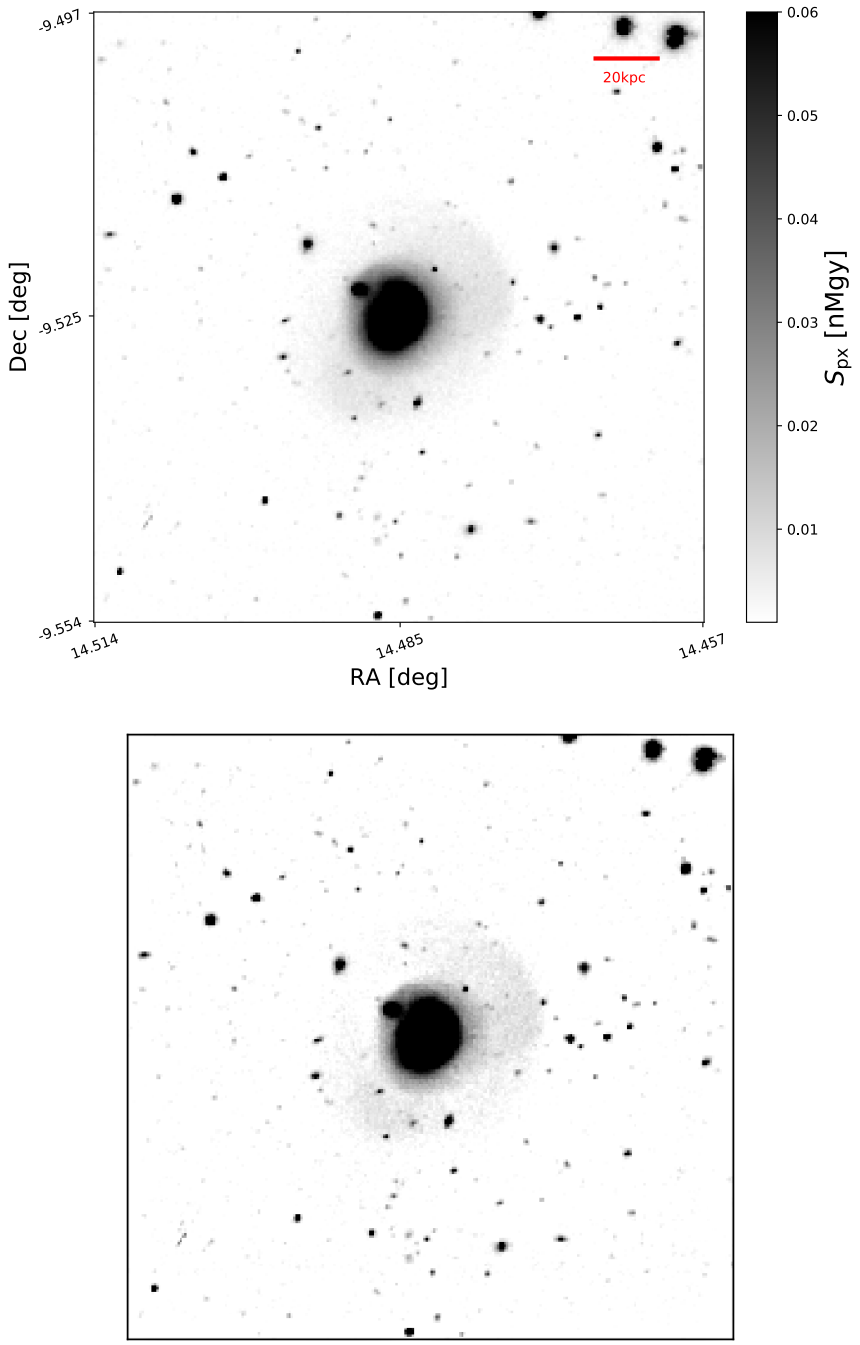

Figure 4.9: The top panel shows the standard DECaLS image of a galaxy with LSB features to the upper-left and lower right. These are more subtle than the LSB that are readily apparent around the galaxy in Figure 4.8, and can be highlighted by applying an unsharp mask, a process involving the subtraction of a Gaussian blur from the original image, to the image as shown in the bottom panel.

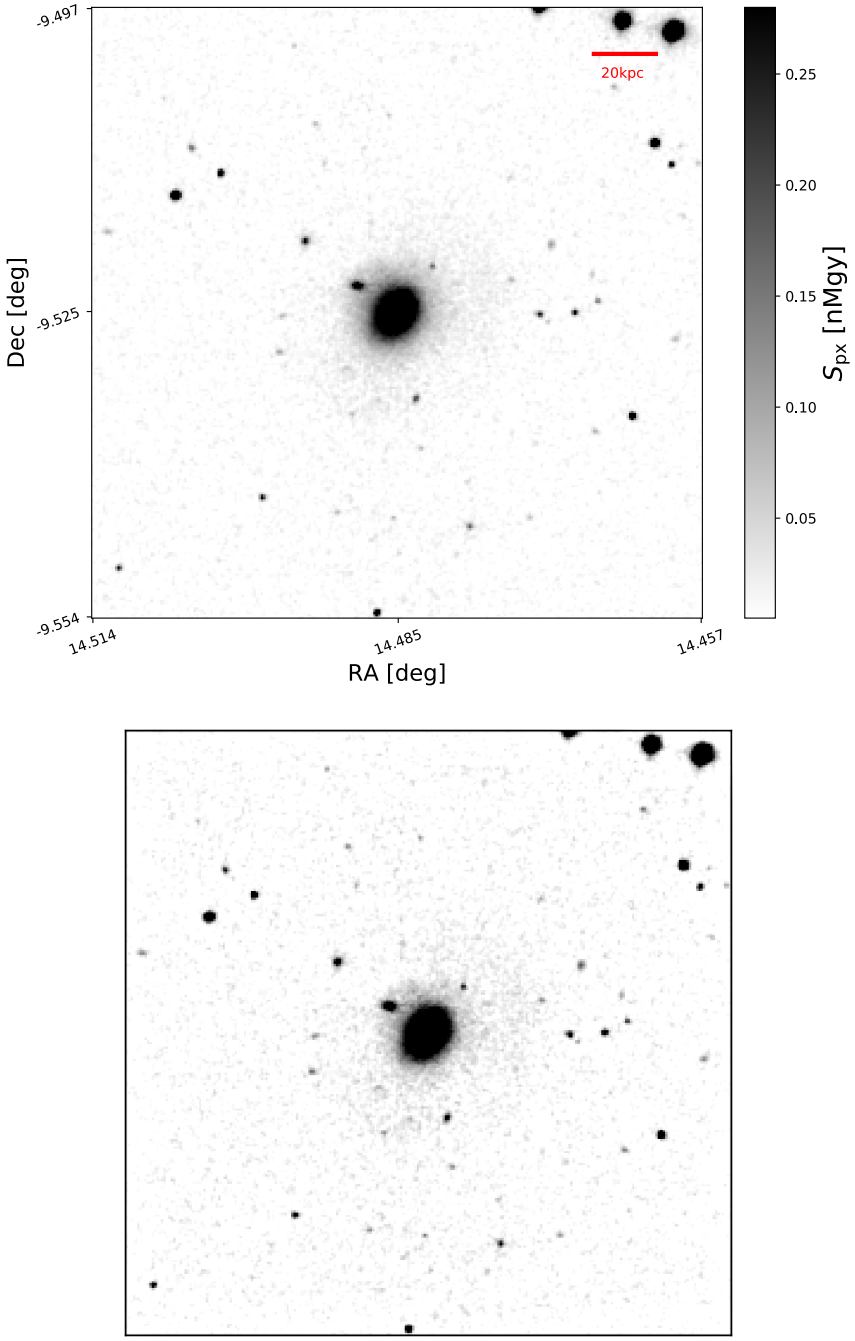

Figure 4.10: The top panel shows the standard SDSS *r*-band image of the same galaxy shown in Figure 4.9. The LSB features visible in the DECaLS image are no longer apparent. Applying an unsharp mask to the image (bottom panel) also fails to show any of the subtle, extended features observed by DECaLS.

Table 4.1: The frequency of low-surface brightness tidal features with LERG radio luminosity. The radio luminosity distribution is split into the lower and upper quartiles and the interquartile range. The upper quartile shows a potential, though insignificant, deficit of LSB tidal feature relative to the control sample.

$L_{1.4\,\mathrm{GHz}}$ range	LERG LSB percentage	Control LSB percentage
(All) $21.73 < \log_{10}\left(\frac{L_{1.4\,\mathrm{GHz}}}{\mathrm{W\,Hz^{-1}}}\right) < 25.21$	$27.0^{+3.5}_{-3.0}$	$31.5^{+2.5}_{-2.3}$
(Q_1) $\log_{10}\left(\frac{L_{1.4\,\mathrm{GHz}}}{\mathrm{W\,Hz^{-1}}}\right) < 22.73$	$28.6^{+7.2}_{-5.5}$	$29.9^{+5.0}_{-4.2}$
(IQR) $22.73 \leq \log_{10}\left(\frac{L_{1.4\,\mathrm{GHz}}}{\mathrm{W\,Hz^{-1}}}\right) \leq 23.39$	$28.3^{+5.1}_{-4.2}$	$29.1^{+3.6}_{-3.1}$
(Q_3) $\log_{10}\left(\frac{L_{1.4\,\mathrm{GHz}}}{\mathrm{W\,Hz^{-1}}}\right) > 23.39$	$22.9^{+7.1}_{-4.9}$	$37.6^{+5.2}_{-4.7}$

Figure 4.11). Our observations here show that the fraction of LERGs with LSB tidal features is again consistent with the control sample. One potential point of interest here is a possible deficit of LERGs with LSB tidal feature at high radio powers, that is $\log_{10}\left(\frac{L_{1.4\,\mathrm{GHz}}}{\mathrm{W\,Hz^{-1}}}\right) > 23.39$. However this observation is only present with $\sim 1.7\sigma$ confidence, and thus lacks significance. The percentages of LERGs and control sample with LSB tidal features for both the whole population and split by radio luminosity are shown in Table 4.1.

4.4.2 The trigger mechanism for LERGs

Our observations have shown that, for the majority of the population, LERGs are no more likely to exhibit LSB tidal features than otherwise similar, radio-quiet galaxies. This is suggestive that minor-mergers are not necessary to trigger LERGs, or at least are not the dominant fuelling mechanism, leaving LERG fuelling as an open problem. It has been observed that LERGS are frequently found in relatively dense environments (e.g., groups and clusters Hardcastle, 2004; Ineson et al., 2015), and that the radio-power of a LERG is positively correlated with both environmental density and ICM temperature (Ineson et al., 2013, 2015). This is consistent with the idea that cooling flows from the ICM may fuel LERGs.

The dense environment in which LERGs are often found is conducive to high-speed galaxy interactions short of mergers, i.e., fly-by events (Sinha & Holley-Bockelmann, 2012; Bialas et al., 2015). This raises the possibility of tidal interactions that would be fainter than those from a minor-merger, and thus may not be visible with current imaging. Additionally, Pace & Salim (2014) showed that even when controlled for large-scale environment, RLAGN have

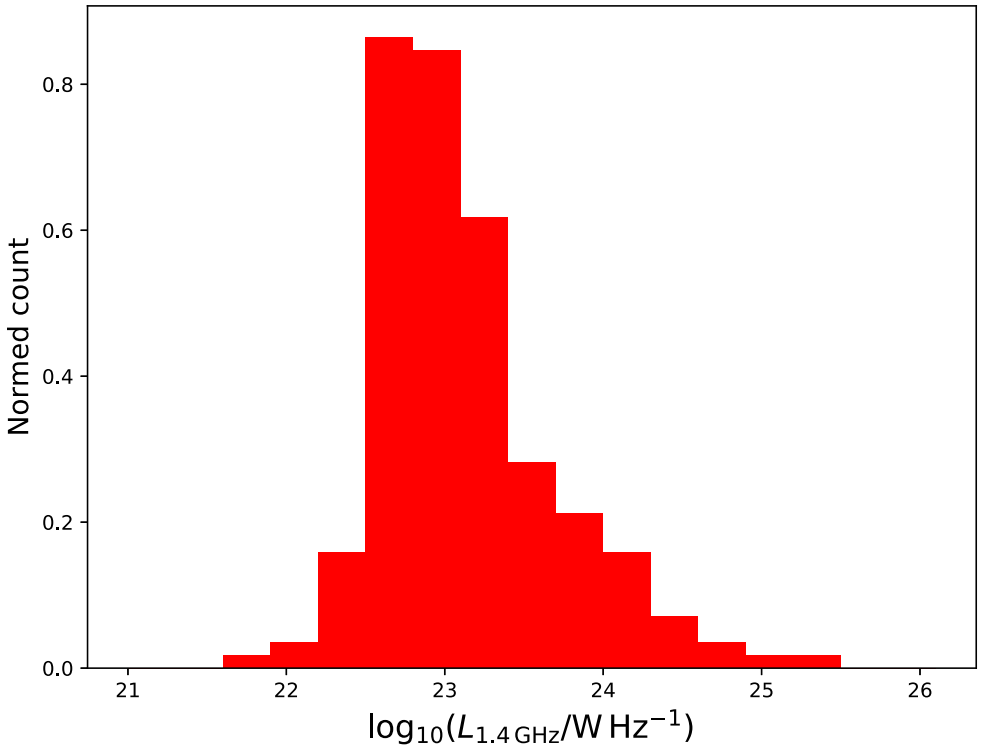

Figure 4.11: The 1.4 GHz luminosity distribution of the LERGs used in this analysis.

significantly more neighbours within 100 kpc than radio-quiet galaxies, further supporting the hypothesis that high speed interactions may be involved in LERG triggering. Our observations do not preclude this possibility should the resultant tidal features be sufficiently faint. Future very deep imaging surveys, e.g., by the Large Synoptic Survey Telescope (LSST, LSST Science Collaboration et al., 2009) may help confirm or further constrain this option.

Our results are consistent with a scenario where minor-mergers are not a significant contributor to LERG activity. However, the potential observation of a deficit of the LERG may suggest some role for minor mergers in the evolution of LERGs with high radio power. This potential deficit is more unexpected when one considers that radio power is correlated with stellar mass (see Figure 4.12). It should also be expected that, given the increased potential well from a more massive galaxy, it should be more likely to have undergone recent minor-mergers, and indeed this is the case for the control population (see the controls of high radio luminosity LERGs in Table 4.1.

The integrated radio luminosity includes contributions from both the jet, and the lobes. These extended structures require time to evolve following triggering, and a higher luminosity is consistent with a more evolved source. Given the potential deficit of LSB tidal features in high radio-luminosity LERGs, it may be possible that minor mergers do trigger LERGs but that the timescale between accretion of the satellite and peak radio luminosity is such that the tidal remnant has dissipated enough to prevent detection. Testing this will require a large sample of LERGs with deeper imaging than used in this work across a range of radio luminosities. Future facilities such as LSST and Taipan in the optical (for deep imaging and spectra respectively, LSST Science Collaboration et al., 2009; da Cunha et al., 2017), and the Australian Square Kilometre Array Pathfinder project in the radio (ASKAP, Johnston et al., 2008) may be able to test this hypothesis.

4.5 Conclusions

This work has tested the hypothesis that weakly accreting RLAGN are triggered and fuelled by minor-mergers (Ellison et al., 2015). This was achieved by comparing the fraction of LERGs and control galaxies with LSB tidal features, attributed to recent minor mergers, in

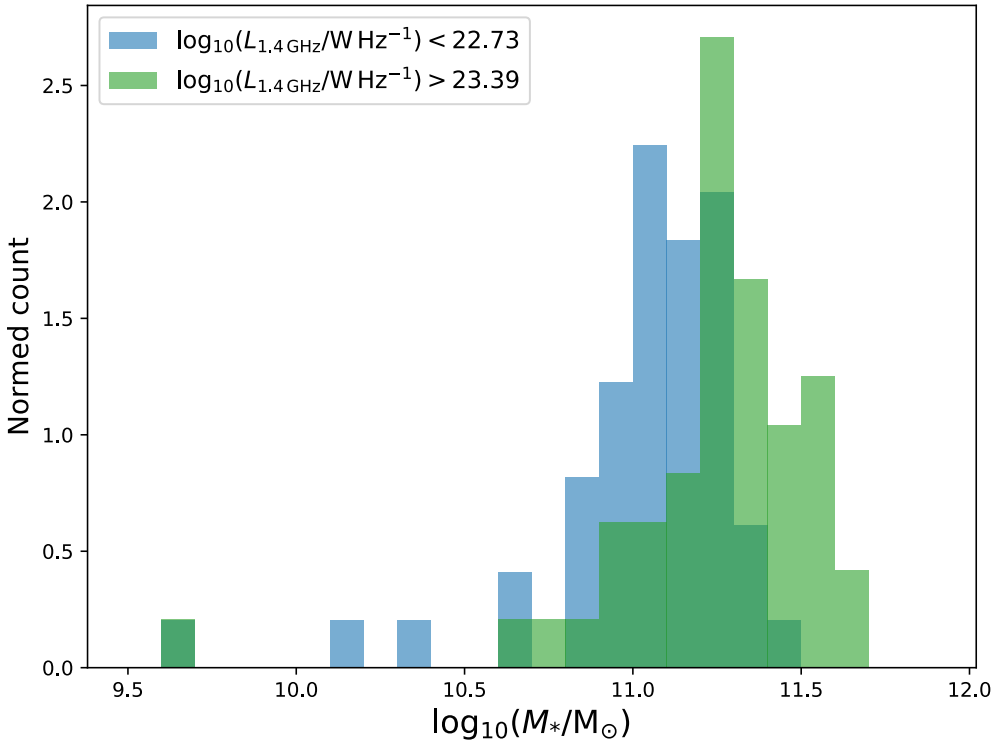

Figure 4.12: The stellar mass distributions of LERGs with $\log_{10}(L_{1.4\,\mathrm{GHz}}/\mathrm{W\,Hz^{-1}}) > 23.39$ (green), and $\log_{10}(L_{1.4\,\mathrm{GHz}}/\mathrm{W\,Hz^{-1}}) < 22.73$ (blue). There is a clear offset in the distributions with a difference in median values of 0.17 dex. That is to say that high power LERGs are $\sim$ 50 per cent more massive than low power LERGs.

deep optical images. Our results are:

i Approximately 30 per cent of both LERGs and control galaxies at $z < 0.07$ have LSB tidal features indicating a recent minor-merger history.

ii Control galaxies are matched to LERGs on stellar mass, morphology, redshift and environment to eliminate these potential sources of bias.

iii When split by radio-luminosity, a similar fraction of low and moderate radio-luminosity LERGs and their control sample have LSB tidal features.

iv We observe a potential, though insignificant at the 1.7σ confidence level, deficit of LSB tidal features in high radio luminosity ($\log_{10}(L_{1.4\,\mathrm{GHz}}/\mathrm{W\,Hz^{-1}}) > 23.39$) LERGs. Further observations of large numbers of high-power LERGs are required to ascertain if this effect is real or not.

These observations are inconsistent with the hypothesis that minor-mergers play a significant role in LERG triggering and fuelling. Consequently these observations may lend support to alternative models of LERG triggering, e.g., weak tidal interactions during high-speed satellite galaxy fly-bys or cooling flows from the ICM.

4.6 Acknowledgements

YAG acknowledges the financial support of the University of Hull through an internally funded PhD studentship that has enabled this research to be undertaken. MSO acknowledges the funding support from the Australian Research Council through a Future Fellowship (FT140100255).

Funding for the SDSS and SDSS-II has been provided by the Alfred P. Sloan Foundation, the Participating Institutions, the National Science Foundation, the U.S. Department of Energy, the National Aeronautics and Space Administration, the Japanese Monbukagakusho, the Max Planck Society, and the Higher Education Funding Council for England. The SDSS Web Site is http://www.sdss.org/.

The SDSS is managed by the Astrophysical Research Consortium for the Participating Institutions. The Participating Institutions are the American Museum of Natural History,

Astrophysical Institute Potsdam, University of Basel, University of Cambridge, Case Western Reserve University, University of Chicago, Drexel University, Fermilab, the Institute for Advanced Study, the Japan Participation Group, Johns Hopkins University, the Joint Institute for Nuclear Astrophysics, the Kavli Institute for Particle Astrophysics and Cosmology, the Korean Scientist Group, the Chinese Academy of Sciences (LAMOST), Los Alamos National Laboratory, the Max-Planck-Institute for Astronomy (MPIA), the Max-Planck-Institute for Astrophysics (MPA), New Mexico State University, Ohio State University, University of Pittsburgh, University of Portsmouth, Princeton University, the United States Naval Observatory, and the University of Washington.

This project used data obtained with the Dark Energy Camera (DECam), which was constructed by the Dark Energy Survey (DES) collaboration. Funding for the DES Projects has been provided by the U.S. Department of Energy, the U.S. National Science Foundation, the Ministry of Science and Education of Spain, the Science and Technology Facilities Council of the United Kingdom, the Higher Education Funding Council for England, the National Center for Supercomputing Applications at the University of Illinois at Urbana-Champaign, the Kavli Institute of Cosmological Physics at the University of Chicago, Center for Cosmology and Astro-Particle Physics at the Ohio State University, the Mitchell Institute for Fundamental Physics and Astronomy at Texas A&M University, Financiadora de Estudos e Projetos, Fundacao Carlos Chagas Filho de Amparo, Financiadora de Estudos e Projetos, Fundacao Carlos Chagas Filho de Amparo a Pesquisa do Estado do Rio de Janeiro, Conselho Nacional de Desenvolvimento Cientifico e Tecnologico and the Ministerio da Ciencia, Tecnologia e Inovacao, the Deutsche Forschungsgemeinschaft and the Collaborating Institutions in the Dark Energy Survey. The Collaborating Institutions are Argonne National Laboratory, the University of California at Santa Cruz, the University of Cambridge, Centro de Investigaciones Energeticas, Medioambientales y Tecnologicas-Madrid, the University of Chicago, University College London, the DES-Brazil Consortium, the University of Edinburgh, the Eidgenossische Technische Hochschule (ETH) Zurich, Fermi National Accelerator Laboratory, the University of Illinois at Urbana-Champaign, the Institut de Ciencies de l'Espai (IEEC/CSIC), the Institut de Fisica d'Altes Energies, Lawrence Berkeley National Labor-

atory, the Ludwig-Maximilians Universitat Munchen and the associated Excellence Cluster Universe, the University of Michigan, the National Optical Astronomy Observatory, the University of Nottingham, the Ohio State University, the University of Pennsylvania, the University of Portsmouth, SLAC National Accelerator Laboratory, Stanford University, the University of Sussex, and Texas A&M University.

This research made use of Astropy, a community-developed core Python package for Astronomy (Astropy Collaboration, 2013).

5. Conclusions and Future Work

"To strive, to seek, to find, and not to yield."

– Alfred Tennyson, *Ulysses (1842)*

5.1 Prologue

This Chapter summarises the research conducted for this thesis. Furthermore, potential directions for future research are discussed. Many of these future research opportunities exploit the potential of the Taipan galaxy survey in terms of it's completeness and footprint. Chapter 5.3 contains some analysis of the two surveys used in this thesis (GAMA and SDSS) in order to make predictions for Taipan. The results of the analysis in this Chapter were used as part of my contribution to the Taipan galaxy survey white paper (da Cunha et al., 2017) published in the Publications of the Astronomical Society of Australia and authored by Elisabete da Cunha, Andrew Hopkins, Matthew Colless, Edward Taylor, Chris Blake, Cullan Howlett, Christina Magoulas, John Lucey, Claudia Lagos, Kyler Kuehn, Yjan Gordon, Dilyar Barat, Fuyan Bian, Christian Wolf, Michael Cowley, Marc White, Ixandra Achitouv, Maciej Bilicki, Joss Bland-Hawthorn, Krzysztof Bolejko, Michael Brown, Rebecca Brown, Julia Bryant, Scott Croom, Tamara Davies, Simon Driver, Miroslav Filipovic, Samuel Hinton, Melanie Johnston-Hollitt, Heath Jones, Bärbel Koribalski, Dane Kleiner, Jon Lawrence, Nuria Lorente, Jeremy Mould, Matt Owers, Kevin Pimbblet, C.G. Tinney, Nicholas Tothill and Fred Watson. Although the predicted number of observed pairs calculated here are used in da Cunha et al. (2017), the full analysis is only presented in original form in this Chapter.

5.2 Summary

The ambition of this thesis has been to demonstrate, using observations from multi-object spectroscopic surveys, the extent to which the host galaxy environment can influence AGN. Moreover, by using those observations attempts are made to understand the underlying physical

processes that may both trigger and inhibit nuclear activity. Specifically, this thesis has addressed the questions:

- Is AGN unification consistent with observations of the small scale environments of type 1 and 2 AGN?
- Are the mechanisms that trigger AGN in cluster infall regions, and suppress AGN in cluster cores at work in galaxy groups?
- Do weakly accreting RLAGN require fuelling by minor-mergers?

Previous observations had ostensibly been at odds with AGN unification by demonstrating that broad- and narrow-line AGN inhabit different small-scale environments (e.g., Jiang et al., 2016; Villarroel & Korn, 2014). In Chapter 2 the high spectroscopic completeness of GAMA was exploited in order to provide a high-quality sample of close galaxy pairs with which to test AGN unification. The close environment of 209 unobscured, 464 partially obscured and 281 obscured optical AGN were analysed comparatively. No significant differences were observed in fraction of AGN with neighbours, or the colours or star-forming behaviours of the neighbouring galaxies. At the smallest scales, that is pairs separated by less than 20 kpc, our observations suggest an excess of type 2 AGN. Taken in conjunction with prior results, this indicates that close interactions may perturb the dusty torus, increasing the likelihood of nuclear obscuration.

In Chapter 3, we expand on previous work on AGN environment in clusters, by testing how group environment influences AGN evolution. In clusters multiple observations have shown that optically selected AGN are preferentially found in the infall regions of massive clusters (Haines et al., 2012; Pimbblet et al., 2013). This has been attributed to increased triggering opportunities such as low-speed galaxy-galaxy interactions, and moderate levels of ram-pressure stripping (Sanders et al., 1988; Moore et al., 1996; Marshall et al., 2018). Additionally observations have shown a deficit of optically selected AGN in cluster cores (Gavazzi et al., 2011; Pimbblet & Jensen, 2012), attributed to a lack of low-speed galaxy-galaxy interactions and difficulty in accreting gas from the hot ICM (Ostriker, 1980; Davies et al., 2017). Again exploiting the high completeness of GAMA, we optically select 451 AGN from 7 498 galaxies

with a stellar mass greater than $10^{9.9}\,M_\odot$ in groups with $11.5 \lesssim \log_{10}(M_{200}/M_\odot) \lesssim 14.5$. We then perform a projected phase space analysis and show two new results. First, that in groups there is no excess of AGN in the infall regions that is seen in massive clusters. Second, the inhibition of AGN in the core of large scale structure evolves with halo mass. Groups with $\log_{10}(M_{200}/M_\odot) < 13.5$ show no AGN deficit in their cores, whereas more massive groups and low-mass clusters show such a deficit at $> 3.5\sigma$ confidence. This demonstrates convincingly that large-scale environment can influence the evolution of AGN.

The lack of evidence for major-mergers being the dominant trigger mechanism for LERGs, and their weakly accreting nature, has led to the hypothesis that minor-mergers provide the fuel supply for these AGN (Hardcastle et al., 2007; Best & Heckman, 2012; Ellison et al., 2015). This supposition is tested in Chapter 4 by using a population of 189 LERGs selected from SDSS and FIRST/NVSS by Best & Heckman (2012), and deep imaging from DECaLS. Imaging of the LERGs is used to search for low-surface brightness tidal features that are the remnants of recent minor-mergers (Kaviraj, 2014a,b). Such features are found in $27^{+3.5}_{-3.0}$ per cent of our LERG sample. In comparison this same evidence for recent minor-merger activity is found in $31.5^{+2.5}_{-2.3}$ per cent of a control population of 372 galaxies matched on redshift, stellar mass, morphology, and large scale environment. Therefore, these observations are inconsistent with the theory that minor-mergers trigger LERGs, suggesting that mechanisms such as the stripping of satellite galaxies during high speed fly-bys, or hot mode accretion from the ICM, may instead provide a fuelling pathway for these AGN.

Chapters 2, 3 and 4 therefore demonstrate that environment plays a significant role in the evolution of AGN and have provided three original contributions to the study of these phenomena. The work in those Chapters was done using legacy data from surveys. In Chapter 5.3 we test how such surveys can be improved upon and make predictions for the Taipan galaxy survey, which addresses the weaker areas of survey design that we highlight. This opens up avenues of investigation into constraining the effect of environment on AGN at the smallest scales, and thus expanding on the research presented in this thesis.

5.3 The Taipan Galaxy Survey

Planning multi-object spectroscopic surveys often require trade-offs to be made between sky-coverage, depth, and spectroscopic completeness. That is, given an allocated amount of observing time, that time must be allocated to some combination of large on-sky area, and re-observing the same field multiple times to circumvent fibre collisions (Strauss et al., 2002). The effect of this is that surveys with high levels of completeness in the densest regions of sky tend to have a small footprint, whilst those with a high footprint lack the observing time to effectively complete the highest density regions of sky.

5.3.1 The importance of completeness

In Chapter 2 it was stated that GAMA was a more complete spectroscopic survey than SDSS. This is a consequence of GAMA repeatedly observing each field of view multiple times, moving spectroscopic fibres between observations, in order to circumvent the fibre-collisions that hamper SDSS (Strauss et al., 2002; Patton & Atfield, 2008; Liske et al., 2015). One way to quantify a difference in completeness is to perform a two-point angular correlation function on both these surveys.

For the GAMA II[1] equatorial regions we select galaxies with spectra obtained by GAMA II and SDSS (up to the tenth data release Ahn et al., 2014). Furthermore, the G09 GAMA equatorial region is not completely covered by SDSS, therefore only GAMA equatorial fields G12 and G15 are used here. To ensure that differences in survey depth do not bias our observations, only galaxies within the magnitude limit of the SDSS spectroscopic survey ($r_{\rm petrosian} < 17.77$) are used. For each galaxy we pair it with all other galaxies (observed by the same survey) inside a 0.5^o radius, and find 10 096 SDSS, and 11 547 GAMA observed galaxies producing 726 162 and 929 904 pairs respectively. To determine the angular correlation function we produce galaxy populations equal in size to the GAMA and SDSS populations, and distribute the galaxies randomly along the same spatial coordinates occupied by the real

[1]As in Chapter 2 GAMA II refers to the second GAMA data release (Liske et al., 2015) that is > 98 per cent complete to $r < 19.8$ across the equatorial regions. The previous data release had only been > 98 per cent complete to $r < 19.4$ in two of three equatorial regions (Driver et al., 2011).

data. The Landy-Szalay estimator, $\omega(\theta)$, given by

$$\omega(\theta) = \frac{DD - 2DR + RR}{RR}, \tag{5.1}$$

where DD, DR, and RR, are the data-data, data-random, and random-random pairs respectively, is then used to calculate the angular correlation (Landy & Szalay, 1993).

In Figure 5.1, we show the two-point correlation functions for both GAMA and SDSS in pair separation bins of 20″ (∼ 40 kpc at the median SDSS redshift of $z = 0.1$, Abazajian et al., 2009) out to to 0.5^o, with the 55″ SDSS fibre collision limit included for reference. The angular correlation functions are shown to deviate at separations below the SDSS fibre collision limit, reaching a 5σ difference at pair separations of $< 20''$. This clearly shows that GAMA is a more effective spectroscopic survey than SDSS for detecting structure on the smallest angular scales, and highlights the impact of fibre collisions on a spectroscopic survey.

5.3.2 Predictions for Taipan

Having demonstrated the advantage in re-observing fields of view multiple times, this section focusses on predictions for a survey with the ambition of surveying with high completeness over a large fraction of the sky. In the northern hemisphere, SDSS provides spectroscopic coverage of ∼ 8 000 deg^2, out to a median redshift of 0.1 (Abazajian et al., 2009). In the southern sky 6dFGS covers 17 000 deg^2 (Jones et al., 2009), however the median redshift of 6dFGS is only ∼ 0.05. Consequently the sample size of 6dFGS is only ∼ 20 per cent that of SDSS (Abazajian et al., 2009; Jones et al., 2009). Given the large size of SDSS, any survey that was competitive in terms of survey footprint and sample size would be required to have some advantage over SDSS in order to justify the expense. In Figure 5.1 it was demonstrated that fibre collisions in SDSS curb its observational completeness on small angular scales, presenting an obvious area for improvement.

The next generation of robotic fibre-positioning technology will allow for fibres to be repositioned in minutes and thus speed up survey operations. In particular, ‘Starbugs’ are robotic fibre positioners that are being used in the TAIPAN instrument (Transforming Astronomical Imaging Through the Polychromatic Analysis of Nebulae, Kuehn et al., 2014;

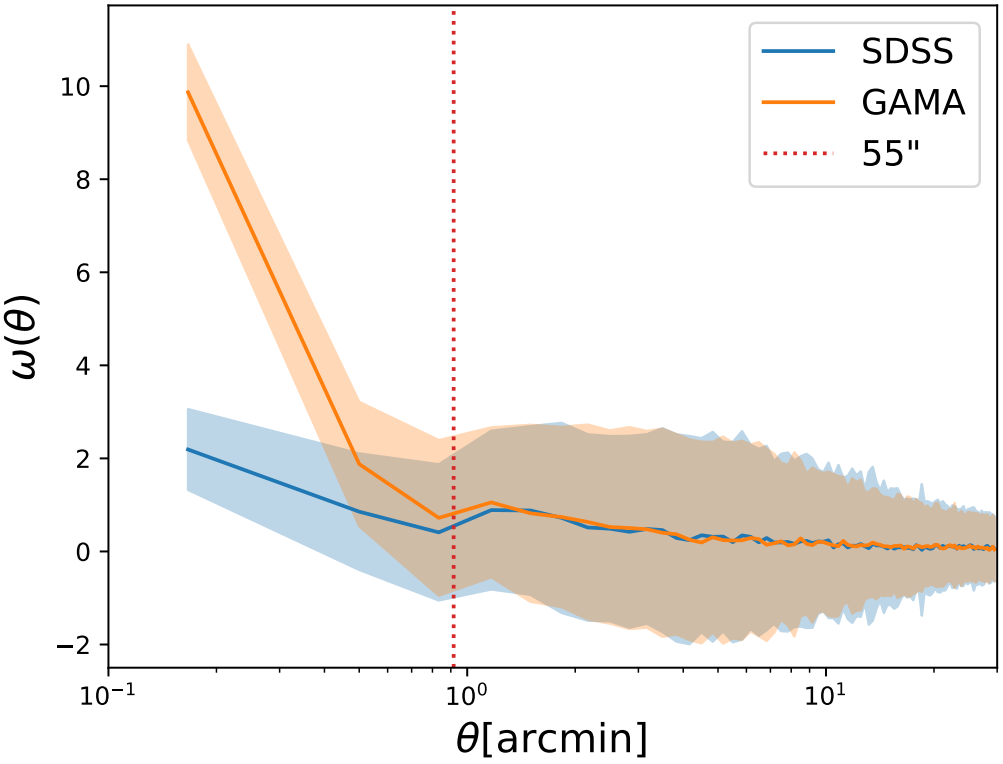

Figure 5.1: The 2-point angular correlation functions, $\omega(\theta)$, of GAMA (orange) and the SDSS spectroscopic survey over the GAMA equatorial regions. A Landy-Szalay estimator was used and the errors are estimated using the bootstrap method. The red dashed line shows the SDSS fibre collision limit of 55". There is a clear (5σ) increase in GAMA detections on the smallest angular scales.

Lorente et al., 2015). Allowing for parallel repositioning of fibres, rather than the serial repositioning of previous fibre positioning systems, Starbugs can reposition 150 fibres across a six degree field of view in under five minutes, a process that could take over an hour in prior surveys (da Cunha et al., 2017). This drastic reduction in 'wasted' observing time means that surveys using this technology can spend more time actually observing, resulting in higher completenesses being possible over larger footprints for a given amount of observing time.

The Taipan Galaxy survey (hereafter refereed to as Taipan, da Cunha et al., 2017) will use the TAIPAN[2] instrument fitted to the 1.2 m UK Schmidt Telescope at Siding Spring Observatory to undertake a spectroscopic survey of the southern sky. Taipan will survey 20 600 deg^2, observing 1.2×10^6 galaxies down to $i < 17$ over a five year period. Taipan is currently scheduled to begin science operations in mid 2018. Rapid redeployment of fibres using Starbug technology will enable Taipan to reobserve fields multiple times using different fibre configurations. Consequently, Taipan will achieve completeness levels comparable to that of GAMA (da Cunha et al., 2017), but over an area nearly twice that of SDSS. This combination of completeness and survey area will be one of the primary advantages of Taipan as a galaxy evolution survey.

If one were to assume that Taipan was to be as complete as GAMA (as is the design of the survey, da Cunha et al., 2017), then predictions for the number of galaxy pairs can be made based on extrapolating from the GAMA dataset. In Figure 5.2 we compare the cumulative number of galaxy pairs separated by less than the SDSS fibre collision limit of 55″ observed per square degree as a function of i-band magnitude (Taipan is i-band selected) of the faintest member of the pair. For this analysis only the GAMA II equatorial regions were considered for GAMA as the southern GAMA regions have not been observed to the same level of completeness. For SDSS, data release 8 was used (Aihara et al., 2011).

Figure 5.2 shows clearly that GAMA detects more of these pairs than SDSS, as would be expected from the angular correlation function shown in Figure 5.1. Integrating the number of pairs in GAMA at $i = 17$ over the Taipan footprint then gives an estimate for the number of such pairs expected to be observed by Taipan. Based on GAMA detecting 6.4 ± 0.2 sub 55″

[2]Taipan refers to the galaxy survey, while the acronym TAIPAN is used to refer to the instrument

Table 5.1: The number of $i < 17$ galaxy pairs at $< 25''$ and $< 55''$ separations as observed by SDSS, and the predictions for Taipan based on extrapolating the observations of GAMA.

Survey (area/deg^2)	$N_{<25''\text{pairs}}$/deg^2	$N_{<25''\text{pairs}}$	$N_{<55''\text{pairs}}$/deg^2	$N_{<55''\text{pairs}}$
SDSS (7 966)	0.38 ± 0.01	$3\,027 \pm 80$	1.29 ± 0.01	$10\,276 \pm 80$
Taipan (20 600)	3.32 ± 0.14	68392 ± 2884	6.38 ± 0.19	$131\,428 \pm 3914$

pairs per square degree at $i < 17$, and Taipan observing 20 600 deg^2, Taipan should expect to observe $132\,000 \pm 4\,000$ pairs satisfying these criteria, more than 10 times the amount observed in SDSS. When a similar comparison is made for sub $25''$ pairs, the difference is even more stark with Taipan expected to observe $\sim$ 20 times the number of galaxy pairs separated by this distance as SDSS. The results of this analysis and the subsequent predictions for Taipan are summarised in Table 5.1.

In Figure 5.3, these observational predictions for Taipan are compared the theoretical predictions of close pairs observable in Taipan using the Lagos et al. (2012) GALFORM model. The GALFORM model predicts a similar pair density to the GAMA observations, strengthening the argument that Taipan will improve on SDSS for spectroscopic observations of small scale environment. Figure 5.2 also shows the number counts for pairs that have a velocity difference of less than 1 000 km s^{-1}, and are thus likely to be gravitationally bound and not just a chance alignment (Robotham et al., 2014). As is the case with the potentially unbound pairs, Taipan is expected to observe more than an order of magnitude more of this type of pair than SDSS.

The increase in the observed numbers of pairs will allow for more reliable studies of galaxy interactions. To demonstrate this let us take the work presented in Chapter 2 as an example. In Chapter 2, 1 039 galaxy pairs were selected where one member contained an AGN. Of these, 456 were separated by $< 55''$. The pairs in Chapter 2 were selected based on $z < 0.3$, whilst Taipan will be selecting based on magnitude, $i < 17$. GAMA observed 145 879 galaxies at $z < 0.3$, of which 11 573 have $i < 17$. That is to say that 7.9 per cent of GAMA galaxies at $z < 0.3$ would be targeted by Taipan. Knowing this, the expected sample of pairs separated by $< 55''$ that would be used in a repeat of the work in Chapter 2 based on Taipan observations can be estimated. This is achieved by taking the product of the fraction

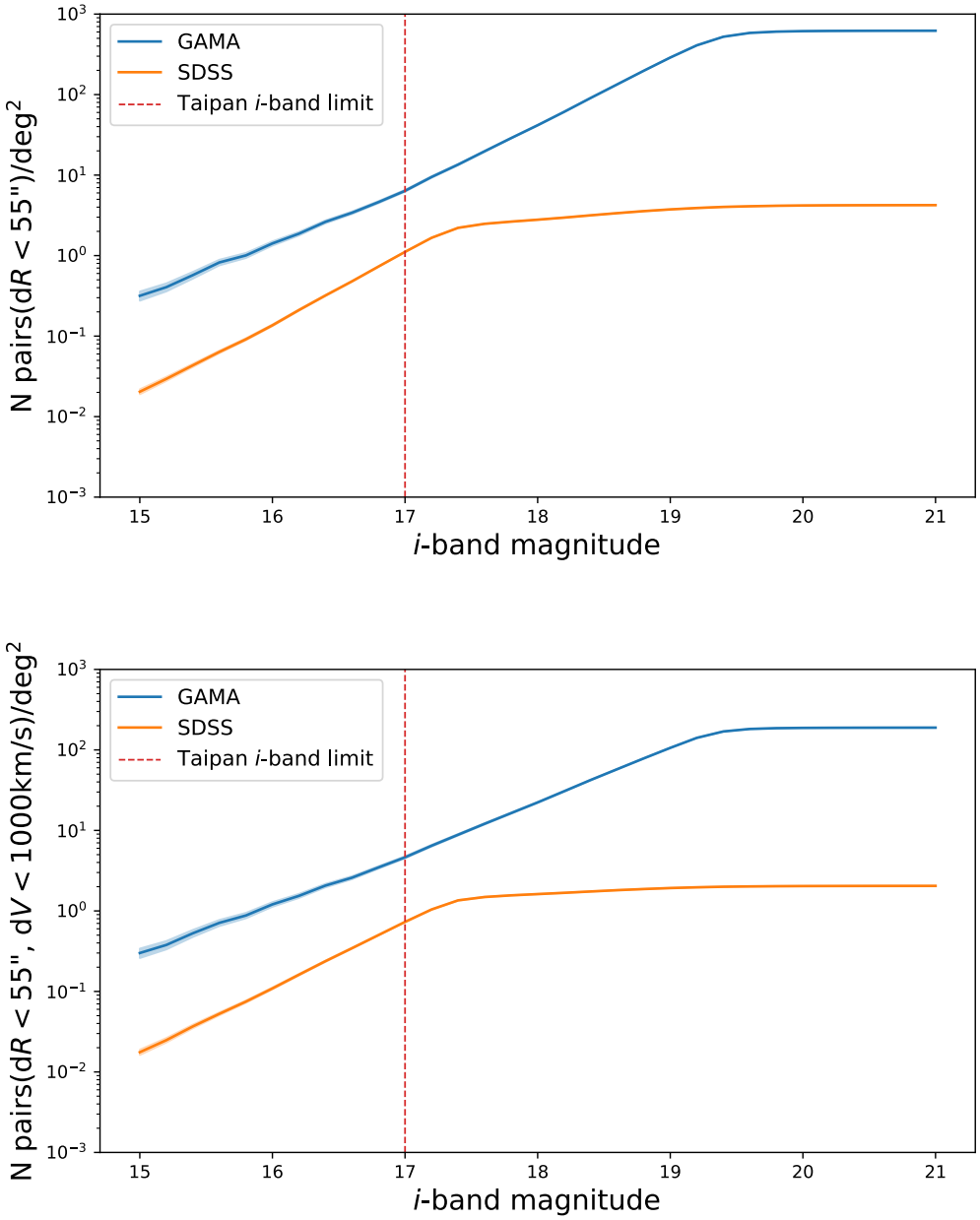

Figure 5.2: The cumulative number density of galaxy pairs separated by less than 55 arc seconds in SDSS and GAMA as a function of i-band magnitude. The bottom panel also requires a velocity separation of no more than 1 000 km s^{-1}, increasing the likelihood that they are indeed bound galaxy pairs and not a chance alignment (Robotham et al., 2014). The blue line represents GAMA, the orange line SDSS, and the red dashed line is the Taipan target selection criteria, $i = 17$. The errors shown are Poissonian and of the order of the line thickness at fainter magnitudes.

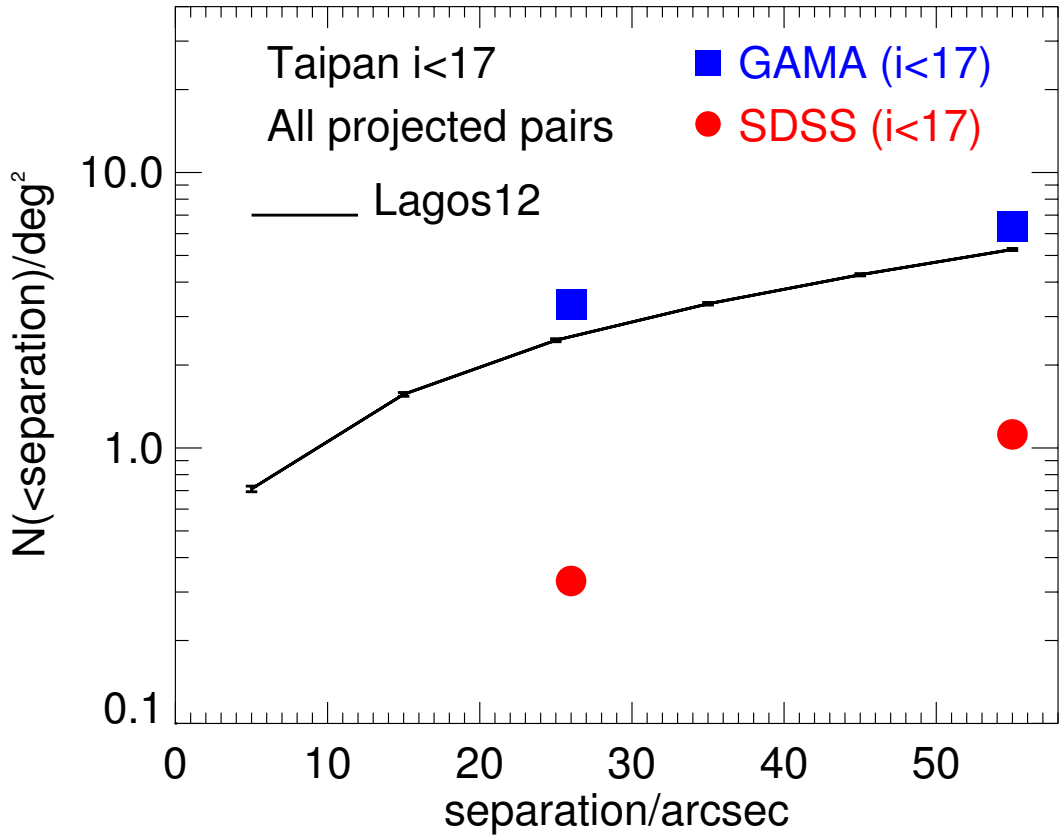

Figure 5.3: The cumulative number density of galaxy pairs as a function of pair separation assuming a limiting magnitude of $i < 17$ mag. The black line is based on the GALFORM model (Cole et al., 2000; Lagos et al., 2011, 2012) predictions for Taipan. The blue squares and red circles are the observed number of galaxy pairs in GAMA and SDSS respectively. Originally Fig. 10 in da Cunha et al. (2017).

of galaxies that would be targeted by Taipan, the ratio of the survey areas, and the observed GAMA sample size, i.e., $0.079 \times (20\,000/180) \times 456 = 4\,122$. Taipan would therefore likely increase the sub 55″ pair sample size in Chapter 2 by a factor of 9. Naturally, this would reduce the scatter on measured quantities by a factor of $\sqrt{9}$, i.e., 3, allowing for a more reliable quantification of the potential excess of type 2 AGN observed in very close pairs. Taipan will therefore be a useful tool in the study of the interacting and merging galaxies, that are separated on the smallest angular scales.

5.4 Future Work

Our results presented in Chapter 2 are suggestive that close galactic interactions, on the ~ 20 kpc scale, increase the likelihood of nuclear obscuration. This is consistent with the observations of Jiang et al. (2016), who observe an excess of satellite galaxies to type 2 AGN. Given the advantages that the Taipan survey will present for observing close galactic interactions, following up on the results of Chapter 2 will be possible in the next few years. In particular exploiting Taipan will allow for constraining the effect on interactions at the ~ 10 kpc scale with high statistical power, something that was not possible using the data available here.

The completeness of Taipan over such a large portion of the sky will allow for in-depth studies into the infall regions of large numbers of galaxy clusters. Given the observations of Haines et al. (2012) and Pimbblet et al. (2013) of an excess number of AGN in the infalling population, it stands to reason that, at least for some of these galaxies, the AGN was triggered prior to infall. It has already been observed that galaxies in the filaments that feed clusters can accrete gas directly from the intergalactic medium (Kleiner et al., 2017), thus providing a potential fuel supply for an AGN. Therefore it may well be the case that preprocessing within galaxy filaments (Balogh et al., 1997; Rines et al., 2005; Sato & Martin, 2006) triggers the AGN prior to its infall into the cluster. The survey design of Taipan will allow for a complete catalogue of the filaments around clusters and testing of this hypothesis.

The observations of LERGs presented in Chapter 4 are inconsistent with minor-mergers being the dominant fuelling mechanism for these AGN. However, the observations of Pace

& Salim (2014) show that LERGs have more satellites than non-LERGs and consequently a denser small scale environment. This could allow for stripping of gas from satellite galaxies to an extent that would not be detectable using DECaLS. In the next five years LSST should begin observations down to $\gtrsim 3$ mag fainter than DECaLS in the r band (LSST Science Collaboration et al., 2009). Consequently, it may be possible to test that hypothesis using imaging from LSST. As LSST will survey the Southern sky, new multi-band observations of the Southern sky will also be required given that FIRST/NVSS, and SDSS are predominantly Northern sky surveys. Such observations could be provided by the Square Kilometre Array, e.g. from WALLABY (the Widefield ASKAP L-band Legacy All-sky Blind surveY, Koribalski, 2012) in the radio, while optical spectra may be obtained from Taipan.

Bibliography

Abazajian K. N., et al., 2009, ApJS, 182, 543

Abbott B. P., et al., 2016, Phys. Rev. Lett., 116, 061102

Abell G. O., 1959, Astron. Soc. Pacific Leafl., 8, 121

Ahn C. P., et al., 2014, ApJS, 211, 17

Aihara H., et al., 2011, ApJS, 193, 29

Allen S. W., Dunn R. J. H., Fabian A. C., Taylor G. B., Reynolds C. S., 2006, MNRAS, 372, 21

Alonso M. S., Lambas D. G., Tissera P., Coldwell G., 2007, MNRAS, 375, 1017

Alpaslan M., et al., 2015, MNRAS, 451, 3249

Angel J. R. P., Stockman H. S., 1980, ARA&A, 18, 321

Antonucci R., 1993, ARA&A, 31, 473

Antonucci R. R. J., Miller J. S., 1985, ApJ, 297, 621

Aragón-Salamanca A., Alonso-Herrero A., Gallego J., Garcia-Dabo C. E., Perez-Gonzalez P. G., Zamorano J., de Paz A. G., 2003, Star Form. through Time, ASP Conf. Ser., 297, 191

Arnold T. J., Martini P., Mulchaey J. S., Berti A., Jeltema T. E., 2009, ApJ, 707, 1691

Arshakian T. G., 2005, A&A, 436, 817

Astropy Collaboration 2013, A&A, 558, A33

Atlee D. W., Mathur S., 2009, ApJ, 703, 1597

Bagchi J., et al., 2014, ApJ, 788, 174

Baldry I. K., 2008, Astron. Geophys., 49, 5.25

Baldwin J. A., Phillips M. M., Terlevich R., 1981, PASP, 93, 5

Balogh M. L., Morris S. L., Yee H. K. C., Carlberg R. G., Ellingson E., 1997, ApJ, 488, L75

Balogh M. L., Morris S. L., Yee H. K. C., Carlberg R. G., Ellingson E., 1999, ApJ, 527, 54

Balogh M. L., Pearce F. R., Bower R. G., Kay S. T., 2001, MNRAS, 326, 1228

Barnes J. E., Hernquist L. E., 1991, ApJ, 370, L65

Barnes J. E., Hernquist L., 1996, ApJ, 471, 115

Barsanti S., et al., 2018, ApJ, 857, 71

Baum S. A., Zirbel E. L., O'Dea C. P., 1995, ApJ, 451, 88

Beall J. H., 2015, in Proc. Sci.. p. 58, http://pos.sissa.it/

Becker R. H., White R. L., Helfand D. J., 1995, ApJ, 450, 559

Belfiore F., et al., 2016, MNRAS, 461, 3111

Bell E. F., McIntosh D. H., Katz N., Weinberg M. D., 2003, ApJS, 149, 289

Best P. N., Heckman T. M., 2012, MNRAS, 421, 1569

Best P. N., Kauffmann G., Heckman T. M., Ivezić Ž., 2005a, MNRAS, 362, 9

Best P. N., Kauffmann G., Heckman T. M., Brinchmann J., Charlot S., Ivezić Ž., White S. D. M., 2005b, MNRAS, 362, 25

Best P. N., Von Der Linden A., Kauffmann G., Heckman T. M., Kaiser C. R., 2007, MNRAS, 379, 894

Bialas D., Lisker T., Olczak C., Spurzem R., Kotulla R., 2015, A&A, 576, A103

Blandford R. D., Znajek R. L., 1977, MNRAS, 179, 433

Blanton M. R., Lin H., Lupton R. H., Maley F. M., Young N., Zehavi I., Loveday J., 2003, AJ, 125, 2276

Bond J. R., Kofman L., Pogosyan D., 1996, Nature, 380, 603

Bournaud F., Dekel A., Teyssier R., Cacciato M., Daddi E., Juneau S., Shankar F., 2011, ApJ, 741, L33

Brough S., et al., 2013, MNRAS, 435, 2903

Buttiglione S., Capetti A., Celotti A., Axon D. J., Chiaberge M., Macchetto F. D., Sparks W. B., 2010, A&A, 509, 6

Calzetti D., 2007, Astron. Soc. Pacific Conf. Ser., 390, 121

Cameron E., 2011, PASA, 28, 128

Cannon R., et al., 2006, MNRAS, 372, 425

Cardiel N., Gorgas J., Cenarro J., González J. J., 1998, Astron. Astrophys. Suppl. Ser., 127, 597

Carlberg R. G., Yee H. K. C., Ellingson E., 1997, ApJ, 478, 462

Carroll B. W., Ostlie D. A., 2006, An Introduction to Modern Astrophysics and Cosmology, 2nd edn. Pearson, San Fransico

Casteels K. R. V., et al., 2014, MNRAS, 445, 1157

Cattaneo A., Combes F., Colombi S., Bertin E., Melchior A.-L., 2005, MNRAS, 359, 1237

Chabrier G., 2003, PASP, 115, 763

Chandrasekhar S., 1931, ApJ, 74, 81

Ching J. H. Y., et al., 2017, MNRAS, 469, 4584

Cid Fernandes R., Stasińska G., Schlickmann M. S., Mateus A., Vale Asari N., Schoenell W., Sodré L., 2010, MNRAS, 403, 1036

Cid Fernandes R., Stasińska G., Mateus A., Vale Asari N., 2011, MNRAS, 413, 1687

Clarke A. O., et al., 2017, Astron. & Astrophys., 601, A25

Cluver M. E., et al., 2014, ApJ, 782, 90

Cole S., Lacey C. G., Baugh C. M., Frenk C. S., 2000, MNRAS, 319, 168

Cole S., et al., 2001, MNRAS, 326, 255

Coles P., Lucchin F., 2002, Cosmology: The Origin and Evolution of Cosmic Structure, 2nd edn. Wiley, Boston, MA

Colless M., 1999, Philos. Trans. R. Soc. A Math. Phys. Eng. Sci., 357, 105

Condon J. J., Cotton W. D., Greisen E. W., Yin Q. F., Perley R. A., Taylor G. B., Broderick J. J., 1998, AJ, 115, 1693

Constantin A., Hoyle F., Vogeley M. S., 2008, ApJ, 673, 715

Croom S. M., Smith R. J., Boyle B. J., Shanks T., Miller L., Outram P. J., Loaring N. S., 2004, MNRAS, 349, 1397

Croom S. M., et al., 2009, MNRAS, 392, 19

Crossett J. P., Pimbblet K. A., Jones D. H., Brown M. J. I., Stott J. P., 2017, MNRAS, 464, 480

Croton D. J., et al., 2006, MNRAS, 365, 11

Croton D. J., et al., 2016, ApJS, 222, 22

Curtis H. D., 1917, PASP, 29, 206

Curtis H. D., 1920, J. R. Astron. Soc. Canada, 14, 317

da Cunha E., et al., 2017, PASA, 34, 47

Davies L. J. M., et al., 2015, MNRAS, 452, 616

Davies L. J. M., et al., 2016, MNRAS, 455, 4013

Davies R. I., et al., 2017, MNRAS, 466, 4917

Davis M., et al., 2003, Proc. SPIE, 4838, 161

De Cia A., et al., 2017, ApJ, submitted

de Grijp M. H. K., Miley G. K., Lub J., de Jong T., 1985, Nature, 314, 240

de Grijp M. H. K., Miley G. K., Lub J., 1987, Astron. & Astrophys. Suppl. Ser., 70, 95

de Jong J. T. A., Verdoes Kleijn G. A., Kuijken K. H., Valentijn E. A., 2013, Exp. Astron., 35, 25

Di Matteo T., Springel V., Hernquist L., 2005, Nature, 433, 604

Dolag K., Bartelmann M., Perrotta F., Baccigalupi C., Moscardini L., Meneghetti M., Tormen G., 2004, A&A, 416, 853

Dressler A., 1980, ApJ, 236, 351

Dressler A., Shectman S. A., 1988, AJ, 95, 985

Drinkwater M. J., et al., 2010, MNRAS, 401, 1429

Driver S. P., et al., 2011, MNRAS, 413, 971

Dultzin-Hacyan D., Krongold Y., Fuentes-Guridi I., Marziani P., 1999, ApJ, 513, L111

Ebeling H., Stephenson L. N., Edge A. C., 2014, ApJ, 781, L40

Eddington A. S., 1924, MNRAS, 84, 308

Ehlert S., Allen S. W., Brandt W. N., Xue Y. Q., Luo B., von der Linden A., Mantz A., Morris R. G., 2013, MNRAS, 428, 3509

Einasto M., et al., 2012, A&A, 540, A123

Eisenstein D. J., et al., 2005, ApJ, 633, 560

Elitzur M., 2012, ApJ, 747, L33

Ellison S. L., Patton D. R., Simard L., McConnachie A. W., 2008, AJ, 135, 1877

Ellison S. L., Patton D. R., Simard L., McConnachie A. W., Baldry I. K., Mendel J. T., 2010, MNRAS, 407, 1514

Ellison S. L., Patton D. R., Mendel J. T., Scudder J. M., 2011, MNRAS, 418, 2043

Ellison S. L., Patton D. R., Hickox R. C., 2015, MNRAS, 451, 35

Faber S. M., Jackson R. E., 1976, ApJ, 204, 668

Fabian A. C., 1994, ARA&A, 32, 277

Fabian A., 2012, ARA&A, 50, 455

Fan L., et al., 2016, ApJ, 822, L32

Fanaroff B. L., Riley J. M., 1974, MNRAS, 167, 31P

Fath E. A., 1909a, Phd thesis, University of California, Berkeley

Fath E. A., 1909b, Pop. Astron., 17, 504

Fender R., 2016, Astron. Nachrichten, 337, 381

Fender R. P., Gallo E., Russell D., 2010, MNRAS, 406, 1425

Ferrarese L., Merritt D., 2000, ApJ, 539, 9

Ferreras I., Silk J., 2000, ApJ, 541, L37

Fliri J., Trujillo I., 2016, MNRAS, 456, 1359

Fraser-McKelvie A., Brown M. J. I., Pimbblet K. A., 2014, MNRAS, 444, L63

Fraser-McKelvie A., Pimbblet K. A., Penny S. J., Brown M. J. I., 2016, MNRAS, 459, 754

Fumagalli M., Fossati M., Hau G. K. T., Gavazzi G., Bower R., Sun M., Boselli A., 2014, MNRAS, 445, 4335

Gardner E., Done C., 2018, MNRAS, 473, 2639

Gatti M., Shankar F., Bouillot V., Menci N., Lamastra A., Hirschmann M., Fiore F., 2016, MNRAS, 456, 1073

Gavazzi G., Savorgnan G., Fumagalli M., 2011, A&A, 534, A31

Gebhardt K., et al., 2000, ApJ, 539, 13

Gill S. P. D., Knebe A., Gibson B. K., 2005, MNRAS, 356, 1327

Gilmour R., Gray M. E., Almaini O., Best P., Wolf C., Meisenheimer K., Papovich C., Bell E., 2007, MNRAS, 380, 1467

Giovanelli R., Haynes M. P., 1985, ApJ, 292, 404

González J., Krongold Y., Dultzin D., Hernández-Toledo H., Huerta E., Olguín L., Marziani P., Cruz-González I., 2008, Rev. Mex. Astron. y Astrofísica, 32, 170G

Goosmann R. W., Czerny B., Mouchet M., Karas V., Dovčiak M., Ponti G., Różańska A., Dumont A.-M., 2006, Astron. Nachrichten, 327, 977

Gopal-Krishna Wiita P. J., 2001, A&A, 373, 100

Gordon Y. A., et al., 2017, MNRAS, 465, 2671

Gordon Y. A., et al., 2018, MNRAS, 475, 4223

Green T. S., et al., 2016, MNRAS, 461, 560

Greenstein J. L., Matthews T. A., 1963, AJ, 68, 279

Grootes M. W., et al., 2017, AJ, 153, 111

Gunawardhana M. L. P., et al., 2011, MNRAS, 415, 1647

Gunawardhana M. L. P., et al., 2013, MNRAS, 433, 2764

Gunn J. E., Gott J. R. I., 1972, ApJ, 176, 1

Haines C. P., et al., 2012, ApJ, 754, 97

Han J., et al., 2015, MNRAS, 446, 1356

Hardcastle M. J., 2004, A&A, 414, 927

Hardcastle M. J., Evans D. A., Croston J. H., 2007, MNRAS, 376, 1849

Hayward C. C., Hopkins P. F., 2017, MNRAS, 465, 1682

Heckman T. M., 1980, Astron. Astrophys., 87, 152

Heckman T. M., Ptak A., Hornschemeier A., Kauffmann G., 2005, ApJ, 634, 161

Herschel W., 1802, Philos. Trans. R. Soc., 92, 477

Hickox R. C., et al., 2009, ApJ, 696, 891

Hickson P., 1997, ARA&A, 35, 357

Hill G. J., Lilly S. J., 1991, ApJ, 367, 1

Hine R. G., Longair M. S., 1979, MNRAS, 188, 111

Hogg D. W., 1999, arXiv.org, astro-ph, 5116

Hopkins A. M., et al., 2013, MNRAS, 430, 2047

Hopkins A. M., Colless M., Blake C., Mould J., Brown M. J. I., Croom S. M., Spitler L., Tinney C., 2014, AAO Obs., pp 8–10

Houghton R. C. W., 2015, MNRAS, 451, 3427

Huang J.-S., Glazebrook K., Cowie L., Tinney C., 2003, ApJ, 584, 203

Hubble E. P., 1926, ApJ, 64, 321

Hubble E. P., 1927a, Publ. Am. Astron. Soc., 5, 261

Hubble E., 1927b, Obs., 50, 276

Hubble E., 1929, Proc. Natl. Acad. Sci., 15, 168

Ineson J., Croston J. H., Hardcastle M. J., Kraft R. P., Evans D. A., Jarvis M., 2013, ApJ, 770, 136

Ineson J., Croston J. H., Hardcastle M. J., Kraft R. P., Evans D. A., Jarvis M., 2015, MNRAS, 453, 2682

Ishibashi W., Fabian A. C., 2012, MNRAS, 427, 2998

Ishibashi W., Auger M. W., Zhang D., Fabian A. C., 2014, MNRAS, 443, 1339

Jiang N., Wang H., Mo H., Dong X., Wang T., Zhou H., 2016, ApJ, 832, 111

Johnston S., et al., 2008, Exp. Astron., 22, 151

Jones D. H., et al., 2004, MNRAS, 355, 747

Jones D. H., et al., 2009, MNRAS, 399, 683

Kant I., 1755, Allgemeine Naturgeschichte und Theorie des Himmels. Zeitz, Bei W. Webel, 1798. Neue aufl., http://adsabs.harvard.edu/abs/1755anth.book.....K

Kass R. E., Raftery A. E., 1995, J. Am. Stat. Assoc., 90, 773

Kauffmann G., et al., 2003, MNRAS, 346, 1055

Kauffmann G., Heckman T. M., Best P. N., 2008, MNRAS, 384, 953

Kaviraj S., 2014a, MNRAS, 437, L41

Kaviraj S., 2014b, MNRAS, 440, 2944

Kawaguchi T., Mineshige S., Machida M., Matsumoto R., Shibata K., 2000, Publ. Astron. Soc. Japan, 52, L1

Kellermann K. I., Sramek R., Schmidt M., Shaffer D. B., Green R., 1989, AJ, 98, 1195

Kenney J. D. P., van Gorkom J. H., Vollmer B., 2004, AJ, 127, 3361

Kennicutt R. C. J., 1992, ApJ, 388, 310

Kennicutt R. C., 1998, ARA&A, 36, 189

Kennicutt R., Tamblyn P., Congdon C. E., 1994, ApJ, 435, 22

Kewley L. J., Dopita M. A., Sutherland R. S., Heisler C. A., Trevena J., 2001, ApJ, 556, 121

Khachakian E. E., Weedman D. W., 1971, Astrofizika, 7, 389

Klebesadel R. W., Strong I. B., Olson R. A., 1973, ApJ, 182, L85

Kleiner D., Pimbblet K. A., Heath Jones D., Koribalski B. S., Serra P., 2017, MNRAS, 466, 4692

Kocevski D. D., et al., 2015, ApJ, 814, 104

Kolehmainen M., Done C., 2010, MNRAS, 406, 2206

Koribalski B. S., 2012, PASA, 29, 359

Koulouridis E., Plionis M., Chavushyan V., Dultzin-Hacyan D., Krongold Y., Goudis C., 2006, ApJ, 639, 37

Krause M., Diehl R., Böhringer H., Freyberg M., Lubos D., 2014, A&A, 566, A94

Krongold Y., Dultzin-Hacyan D., Marziani P., 2002, ApJ, 572, 169

Krumpe M., Miyaji T., Coil A. L., Aceves H., 2018, MNRAS, 474, 1773

Kuehn K., et al., 2014, Proc. SPIE, 9147, 914710

LSST Science Collaboration et al., 2009, arXiv e-prints, 0912, 0201

Lagos C. d. P., Lacey C. G., Baugh C. M., Bower R. G., Benson A. J., 2011, MNRAS, 416, 1566

Lagos C. d. P., Bayet E., Baugh C. M., Lacey C. G., Bell T. A., Fanidakis N., Geach J. E., 2012, MNRAS, 426, 2142

Landy S. D., Szalay A. S., 1993, ApJ, 412, 64

Larson R. B., Tinsley B. M., Caldwell C. N., 1980, ApJ, 237, 692

Le Fèvre O., et al., 2005, Astron. Astrophys., 439, 845

Le Fèvre O., et al., 2013, A&A, 559, A14

Lee J. C., Iwasawa K., Houck J. C., Fabian A. C., Marshall H. L., Canizares C. R., 2002, ApJ, 570, L47

Lemaître G., 1927, Ann. la Sociètè Sci. Bruxelles, A47, 49

Lemaître G., 1931, MNRAS, 91, 483

Lintott C., et al., 2011, MNRAS, 410, 166

Liske J., Lemon D. J., Driver S. P., Cross N. J. G., Couch W. J., 2003, MNRAS, 344, 307

Liske J., et al., 2015, MNRAS, 452, 2087

Lopes P. A. A., Ribeiro A. L. B., Rembold S. B., 2017, MNRAS, 472, 409

Lorente N., Vuong M., Satorre C., Hong S. E., Shortridge K., Goodwin M., Kuehn K., 2015, Astron. Soc. Pacific Conf. Ser., 495, 265

Lotz J. M., Jonsson P., Cox T. J., Primack J. R., 2010, MNRAS, 404, 575

Loveday J., et al., 2015, MNRAS, 451, 1540

Madau P., Pozzetti L., Dickinson M., 1998, ApJ, 498, 106

Magorrian J., et al., 1998, AJ, 115, 2285

Mahajan S., Raychaudhury S., Pimbblet K. A., 2012, MNRAS, 427, 1252

Maraschi L., Colpi M., Ghisellini G., Perego A., Tavecchio F., 2012, J. Phys. Conf. Ser., 355, 012016

Markwardt C., 2009, in Bohlender D., Durand D., Dowler P., eds, Vol. 411, A.S.P. Conf. Ser.. San Fransico, p. 251

Markwardt C., 2010, Markwardt IDL Library, http://www.physics.wisc.edu/$\sim$craigm/idl/idl.html

Marshall M. A., Shabala S. S., Krause M. G. H., Pimbblet K. A., Croton D. J., Owers M. S., 2018, MNRAS, 474, 3615

Martini P., Kelson D. D., Kim E., Mulchaey J. S., Athey A. A., 2006, ApJ, 644, 116

Masters K. L., et al., 2010, MNRAS, 405, 783

Mathis J. S., 1990, ARA&A, 28, 37

Matthews T. A., Sandage A. R., 1963, ApJ, 138, 30

McKinney J. C., 2005, ApJ, 630, L5

McLean I. S., Aspin C., Heathcote S. R., McCaughrean M. J., 1983, Nature, 304, 609

McNamara B., Nulsen P., 2007, ARA&A, 45, 117

Menon T. K., 1995, MNRAS, 274, 845

Messier C., 1781, Connoissance des Temps ou des Mouvements Célestes, 1784, 227

Mickaelian A. M., Sanders D. B., 2014, Proc. Int. Astron. Union Symp. Colloq., 304

Mihos J. C., Hernquist L., 1996, ApJ, 464, 641

Miller J. S., Antonucci R. R. J., 1983, ApJ, 271, L7

Miller C. J., Nichol R. C., Gó Mez P. L., Hopkins A. M., Bernardi M., 2003, AJ, 597, 142

Mingo B., Hardcastle M. J., Croston J. H., Dicken D., Evans D. A., Morganti R., Tadhunter C., 2014, MNRAS, 440, 269

Moore B., Katz N., Lake G., Dressler A., Oemler A., 1996, Nature, 379, 613

Moore B., Lake G., Katz N., 1998, ApJ, 495, 139

Moster B. P., Somerville R. S., Maulbetsch C., van den Bosch F. C., Macciò A. V., Naab T., Oser L., 2010, ApJ, 710, 903

Munari E., Biviano A., Borgani S., Murante G., Fabjan D., 2013, MNRAS, 430, 2638

Mutch S. J., Croton D. J., Poole G. B., 2013, MNRAS, 435, 2445

Narayan R., McClintock J. E., 2012, MNRAS, 419, L69

Navarro J. F., Frenk C. S., White S. D. M., 1996, ApJ, 462, 563

Nazaryan T. A., Petrosian A. R., Hakobyan A. A., McLean B. J., Kunth D., 2013, Proc. Int. Astron. Union, 9, 327

Neugebauer G., Becklin E. E., Oke J. B., Searle L., 1976, ApJ, 205, 29

Newton I., 1687, Philosophiae Naturalis Principia Mathematica. Jussu Societatis Regiæ ac Typis Joseph Streater, London, doi:10.3931/e-rara-440

Newton R. D. A., Kay S. T., 2013, MNRAS, 434, 3606

Norberg P., et al., 2002, MNRAS, 336, 907

Oh S., et al., 2014, ApJ, 790, 43

Oman K. A., Hudson M. J., 2016, MNRAS, 463, 3083

Oman K. A., Hudson M. J., Behroozi P. S., 2013, MNRAS, 431, 2307

Osterbrock D. E., 1981, ApJ, 249, 462

Ostriker J. P., 1980, Comments Astrophys., 8, 177

Owen F. N., Ledlow M. J., 1994, in Bicknell G., Dopita M. A., Quinn P., eds, Vol. 54, A.S.P. Conf. Ser.. p. 319

Owers M. S., Blake C., Couch W. J., Pracy M. B., Bekki K., 2007, MNRAS, 381, 494

Owers M. S., Couch W. J., Nulsen P. E. J., Randall S. W., 2012, ApJ, 750, L23

Owers M. S., et al., 2013, ApJ, 772, 104

Owers M. S., et al., 2017, MNRAS, 468, 1824

Pace C., Salim S., 2014, ApJ, 785, 66

Palomar Observatory 1949, Nature, 164, 97

Pan D. C., Vogeley M. S., Hoyle F., Choi Y.-Y., Park C., 2012, MNRAS, 421, 926

Patton D. R., Atfield J. E., 2008, ApJ, 685, 235

Patton D. R., Torrey P., Ellison S. L., Mendel J. T., Scudder J. M., 2013, MNRAS, 433, L59

Pentericci L., et al., 2013, A&A, 552, A111

Percival W. J., et al., 2002, MNRAS, 337, 1068

Perlmutter S., et al., 1999, ApJ, 517, 565

Peterson J., Fabian A., 2006, Phys. Rep., 427, 1

Pimbblet K. A., 2011, MNRAS, 411, 2637

Pimbblet K. A., Jensen P. C., 2012, MNRAS, 426, 1632

Pimbblet K. A., Shabala S. S., Haines C. P., Fraser-McKelvie A., Floyd D. J. E., 2013, MNRAS, 429, 1827

Pinkney J., Roettiger K., Burns J. O., Bird C. M., 1996, ApJS, 104, 1

Poggianti B. M., Wu H., 2000, ApJ, 529, 157

Poggianti B. M., et al., 2017, Nature, 548, 304

Pracy M., et al., 2016, MNRAS, 17, 2

Quilis V., 2000, Science (80-.)., 288, 1617

Rieke G. H., 1978, ApJ, 226, 550

Rieke G. H., Lebofsky M. J., 1979, ARA&A, 17, 477

Rines K., Geller M. J., Kurtz M. J., Diaferio A., 2005, AJ, 130, 1482

Robotham A., et al., 2010, PASA, 27, 76

Robotham A. S. G., et al., 2011, MNRAS, 416, 2640

Robotham A. S. G., et al., 2014, MNRAS, 444, 3986

Roediger E., 2009, Astron. Nachrichten, 330, 888

Rubin V. C., Hunter D. A., Ford, W. Kent J., 1991, ApJS, 76, 153

Ruderman J. T., Ebeling H., 2005, ApJ, 623, L81

Russell H. N., 1914, Pop. Astron., 22, 275

Russell D. M., Gallo E., Fender R. P., 2013, MNRAS, 431, 405

Salpeter E. E., 1955, ApJ, 121, 161

Salpeter E. E., 1964, ApJ, 140, 796

Samui S., 2014, New Astron., 30, 89

Sanchez S. F., et al., 2017, Rev. Mex. Astron. y Astrofísica, In press, arXiv:1709.05438

Sanders D. B., Soifer B. T., Elias J. H., Madore B. F., Matthews K., Neugebauer G., Scoville N. Z., 1988, ApJ, 325, 74

Sanders D. B., Egami E., Lipari S., Mirabel I. F., Soifer B. T., 1995, AJ, 110, 1993

Saripalli L., 2012, AJ, 144, 85

Sarzi M., et al., 2006, MNRAS, 366, 1151

Sato T., Martin C. L., 2006, ApJ, 647, 946

Satyapal S., Ellison S. L., McAlpine W., Hickox R. C., Patton D. R., Trevor Mendel J., 2014, MNRAS, 441, 1297

Saunders W., et al., 2004, Proc. SPIE - Int. Soc. Opt. Eng., 5492, 389S

Sauty C., Tsinganos K., Trussoni E., 2002, Lect. Notes Phys., 589, 41

Scannapieco C., Tissera P. B., White S. D. M., Springel V., 2008, MNRAS, 389, 1137

Schawinski K., Thomas D., Sarzi M., Maraston C., Kaviraj S., Joo S.-J., Yi S. K., Silk J., 2007, MNRAS, 382, 1415

Schawinski K., et al., 2010, ApJ, 711, 284

Schawinski K., et al., 2014, MNRAS, 440, 889

Schechter P., 1976, ApJ, 203, 297

Schmidt M., 1963, Nature, 197, 1040

Schmidt B. P., et al., 1998, ApJ, 507, 46

Schulz S., Struck C., 2001, MNRAS, 328, 185

Scudder J. M., Ellison S. L., Mendel J. T., 2012a, MNRAS, 423, 2690

Scudder J. M., Ellison S. L., Torrey P., Patton D. R., Mendel J. T., 2012b, MNRAS, 426, 549

Serjeant S., 2010, Observational Cosmology. Cambridge University Press, Cambridge

Seyfert C. K., 1943, ApJ, 97, 28

Shabala S. S., et al., 2012, MNRAS, 423, 59

Shabala S. S., Deller A., Kaviraj S., Middelberg E., Turner R. J., Ting Y. S., Allison J. R., Davis T. A., 2017, MNRAS, 464, 4706

Shapley H., 1919, PASP, 31, 261

Shapley H., Curtis H. D., 1921, Bull. Natl. Res. Counc., 2, 171

Shen Y., Mulchaey J. S., Raychaudhury S., Rasmussen J., Ponman T. J., 2007, ApJ, 654, L115

Sikora M., Stawarz L., Lasota J.-P., 2007, ApJ, 658, 815

Silk J., Rees M. J., 1998, Astron. & Astrophys., 331, L1

Singh R., et al., 2013, A&A, 558, A43

Sinha M., Holley-Bockelmann K., 2012, ApJ, 751, 17

Slipher V., 1915, Pop. Astron., 23, 21

Smethurst R. J., et al., 2016, MNRAS, 463, 2986

Smith R. J., et al., 2004, AJ, 128, 1558

Soifer B. T., Boehmer L., Neugebauer G., Sanders D. B., 1989, AJ, 98, 766

Springel V., 2005, MNRAS, 364, 1105

Springel V., et al., 2005, Nature, 435, 629

Stasińska G., Cid Fernandes R., Mateus A., Sodré L., Asari N. V., 2006, MNRAS, 371, 972

Steele I. A., et al., 2004, Proc. SPIE, 5489, 679

Stein W. A., Weedman D. W., 1976, ApJ, 205, 44

Stoner E., 1930, Philos. Mag., 9, 944

Strauss M. a., Weinberg D. H., Lupton R. H., Narayanan V. K., 2002, AJ, 124, 1810

Tadhunter C. N., Morganti R., Robinson A., Dickson R., Villar-Martin M., Fosbury R. A. E., 1998, MNRAS, 298, 1035

Taylor E. N., et al., 2011, MNRAS, 418, 1587

Tchekhovskoy A., Narayan R., McKinney J. C., 2010, ApJ, 711, 50

Tegmark M., et al., 2004, ApJ, 606, 702

Thomas D., Maraston C., Bender R., de Oliveira C. M., 2005, ApJ, 621, 673

Tonnesen S., Bryan G. L., 2009, ApJ, 694, 789

Tonry J., Davis M., 1979, AJ, 84, 1511

Tran H. D., 2001, ApJ, 554, L19

Tremonti C. A., et al., 2004, ApJ, 613, 898

Tzanavaris P., et al., 2014, ApJS, 212, 9

Ueda Y., et al., 2015, ApJ, 815, 1

Urry C. M., Padovani P., 1995, PASP, 107, 803

van Maanen A., 1916, ApJ, 44, 210

Villarroel B., Korn A. J., 2014, Nat. Phys., 10, 417

Viola M., et al., 2015, MNRAS, 452, 3529

Walcher J., Groves B., Budavàri T., Dale D., 2011, Astrophys. Space Sci., 331, 1

Walter F., Weiss A., Scoville N., 2002, ApJ, 580, L21

Wang T., et al., 2017, A&A, 601, A63

Ward M., Penston M. V., Blades J. C., Turtle A. J., 1980, MNRAS, 193, 563

Wijesinghe D. B., et al., 2011, MNRAS, 410, 2291

Wilkes B. J., 2004, in Richards G., Hall P., eds, Vol. 311, ASP Conf. Ser.. San Fransico, p. 37

Wilson A. S., Colbert E. J. M., 1995, ApJ, 438, 62

Woltjer L., 1959, ApJ, 130, 38

Woods D. F., Geller M. J., 2007, AJ, 134, 527

Xu L., Rieke G. H., Egami E., Pereira M. J., Haines C. P., Smith G. P., 2015, ApJS, 219, 18

Yang X., Mo H. J., van den Bosch F. C., Pasquali A., Li C., Barden M., 2007, ApJ, 671, 153

Yi S. K., et al., 2005, ApJ, 619, L111

York D. G., et al., 2000, AJ, 120, 1579

Yun M. S., Reddy N. A., Condon J. J., 2001, ApJ, 554, 803

Zel'dovich Y. B., 1964, Sov. Phys. Dokl., 9, 195